INVESTIGATING THE ENIGMATIC ORBIT OF THE SUSPECTED 2.5 M_J PLANET IN THE NU OCTANTIS BINARY SYSTEM

A thesis submitted in partial fulfilment of the requirements for the

Degree of Master of Science in Astronomy

in the University of Canterbury

by A. T. Dallow

University of Canterbury

2012

Contents

Chapter 1 Introduction 1

1.1 A Brief History of Planet Hunting 1

1.2 The Doppler Method 3

1.3 Other Indirect Methods of Detection 13

1.3.1 The Transit Method 13

1.3.2 Gravitational Microlensing 16

1.3.3 The Pulsar Timing Method 18

1.4 Giant Planets 20

Chapter 2 ν Octantis 24

2.1 Properties of ν Octantis 24

2.2 Possible Planetary Perturbation in the RVs of ν Octantis 28

2.3 Retrograde Orbit of the Planetary Companion 33

2.4 Precession due to a Close Binary System 36

Chapter 3 Modelling the Orbit of the ν Octantis Planet 39

3.1 Modelling the Orbit 39

3.2 Simulation Results and Discussion 47

3.2.1 Confirmation of Retrograde Orbital Stability 47

3.2.2 100-Million year Retrograde Orbit Simulation 49

3.2.3 Stability of Other Orbits in the ν Octantis System 53

3.2.4 The Periodic Variation in the Eccentricity of ν Octantis 59

3.2.5 Stability of Non-Coplanar Retrograde Orbits 67

3.3 Conclusion 68

Chapter 4 ν Octantis Observations 70
4.1 Introduction 70
4.2 Acquisition of ν Octantis Spectra 72
4.2.1 The HERCULES Spectrograph, CCD and Telescope 72
4.2.2 The Iodine Absorption Cell 75
4.2.3 Mt John Observing Program 77
4.3 Reduction of Spectra 78
4.3.1 HERCULES Reduction Software Package (HRSP) 78
4.3.2 High Precision Radial Velocities 81
4.4 Results and Discussion 84
4.4.1 Raw Radial Velocities of ν Octantis 84
4.4.2 Analysis of the Suggested Planet's Radial Velocity Perturbation 91
4.4.3 Comparison to Simulations 98
4.5 Conclusion 101
Chapter 5 Conclusion 103
Appendix 110
References 116

Acknowledgments

It is with immense gratitude that I acknowledge my Professor, John Hearnshaw, Department of Physics and Astronomy, University of Canterbury, without whose kind help, guidance and support, this thesis would not have been completed.

I am very much grateful to Dr. Erik Brogt, Academic Development Group, University of Canterbury, for your valuable suggestions, moral support and helping me with clearly communicating my ideas.

I sincerely thank Dr. David Ramm, Department of Physics and Astronomy, University of Canterbury, for his generous assistance.

Abstract

ν Octantis is a spectroscopic binary with a semi-major axis and period of 2.55 AU and 2.9 years, respectively. Ramm et al. (2009) discovered a 52 ms^{-1} radial-velocity (RV) perturbation with a period of 417 days in this system. All evidence, both photometric and spectroscopic, suggests the perturbation is the result of a 2.5 M_J planet orbiting the primary star. However, when assuming a "normal" prograde coplanar orbit, celestial mechanics predicts this orbit is unstable, contradicting the observed stability.

Simulations by Eberle and Cuntz (2010) showed a retrograde orbit for the planet to be stable for at least 10^7 years. In this thesis, we performed a 10^8-yr simulation of the retrograde orbit, and found it remained stable. Simulations over a range of planetary semi-major axes, eccentricities, and primary/secondary masses showed that stable retrograde orbits are not possible past a semi-major axis of 1.315 ± 0.092 AU. Therefore, planetary retrograde orbits are most likely inherently more stable than prograde orbits owing to the absence of stability at known mean-motion resonances.

Eccentricity simulations showed that the period of the planet's dominant eccentricity variation is related to the planet's semi-major axis by a second order exponential. However, retrograde orbits tend to have longer eccentricity periods than prograde orbits at the same semi-major axis. There is also evidence that this eccentricity period is connected to the orbital stability.

By fitting a keplerian to both Ramm et al. (2009) and current radial velocities, the period of the ν Octantis binary was determined to be 1050.04 ± 0.02 days with an eccentricity of 0.2359 ± 0.001. The planetary orbital solution for just the data reduced in this thesis gave a period of 416.9 ± 2.1 days and an eccentricity of 0.099 ± 0.015, with an RMS scatter of 9.6 ms^{-1}. Therefore, the orbital elements are within 1σ of the Ramm et al. (2009) elements. Assuming a retrograde coplanar orbit about the primary star then the planet has a mass of $M_{pl} = 2.3\ M_J$ and a semi-major axis of $a_{pl} = 1.21 \pm 0.09$ AU.

Chapter 1
Introduction

1.1 A Brief History of Planet Hunting

In 1600 Giordano Bruno expanded on Copernican theory by suggesting that fixed stars in the sky were in fact similar to our Sun in that they may contain orbiting planets. Unfortunately, he was burnt at the stake by the Roman Inquisition for his views, but his ideas did not go to the grave; instead they sparked the interests of many future scientists (Rabin, 2010). In 1609 Johannes Kepler published the first two laws of planetary motion; The orbit of every planet is an ellipse with the Sun at the centre of one of the two foci, and the line joining a planet and the Sun sweeps out equal areas during equal intervals of time (Kepler, 1609). Kepler then published the third law in 1619 that the square of the orbital period of a planet is directly proportional to the cube of the semi-major axis of its orbit (Kepler, Ptolemaeus and Fludd, 1619). These laws enabled us to model the orbits of planets in our solar system like never before and can be adapted to extrasolar planets. The eighteenth

century saw Isaac Newton, known today as the father of classical mechanics, publish the laws of motion and universal gravitation (Newton, 1760). This allowed future astronomers to form theories of how one might observe an extrasolar planet.

Many attempts have been made since Newton's time to detect planets around other stars, such as: 70 Ophiuchi in 1855 by Capt. W. S. Jacob who reported 'orbital anomalies' in the star making it 'highly probably' of a planet in the system (Jacob, 1855). However, in the 1890's F. R. Moulton published a paper on a three-body simulation of the system and found it to be highly unstable (See, 1896). During 1950 - 1960 Peter van der Kamp made a prominent series of detection claims about a Jupiter mass planet orbiting Barnard's star. Because of the very limited precision of the data during this early period, astronomers now regard these as erroneous (Boss, 2009).

The first confirmed planets were detected orbiting PSR 1257+12 via the pulsar timing technique by A. Wolszczan and D. Frail (1992). As technology advanced rapidly in high resolution spectroscopy and CCD chips during the 1990's many more planets were detected, in particular the first planet detected by the Doppler technique was 51 Pegasi by M. Mayor and D. Queloz in 1995 (Mayor and Queloz, 1995). As of July 2012 777 planets (Schneider, 2012) have been discovered using the methods described in sections 1.2-1.3.

1.2 The Doppler Method

To understand the Doppler Method we must first understand how two bodies orbit about one another. By Newton's universal law of gravitation and the conservation of angular momentum, two stars with mass M_1 and M_2 must orbit their common centre of mass (COM). From the observers perspective one can measure the radial velocity component ($\dot{z}$) via the Doppler effect, which would appear to vary periodically with a period (P) depending on the eccentricity (e), semi-major axis (a), and semi-amplitude (K) of the system.

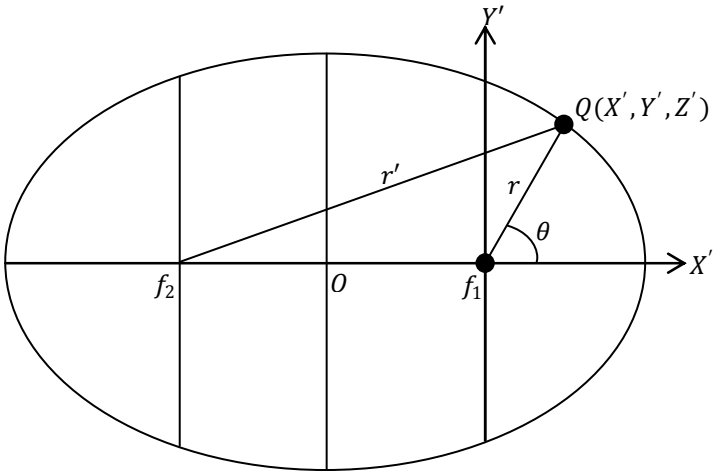

Figure 1.2.1 - *Diagram of an elliptical orbit in a two body system.*

[1]To model the variation in radial velocity seen by the observer suppose we have an elliptical orbit of the body **Q** with mass (M_2) about some central mass (M_1) positioned at focus f_1 as shown in Figure 1.2.1. The angular momentum ($\boldsymbol{J}$) of a body with linear momentum $\boldsymbol{p}$ relative to the origin is defined as (Hilditch, 2001):

$$\boldsymbol{J} = (\boldsymbol{r} \times \boldsymbol{p})$$

$$\boldsymbol{J} = \mu(\boldsymbol{r} \times \boldsymbol{v}) \tag{1.2.1}$$

where μ is the reduced mass $\frac{M_1 M_2}{M_1 + M_2}$, $\boldsymbol{v}$ is the tangential velocity, and $\boldsymbol{r}$ the radius vector from f_1. The time derivative of $\boldsymbol{J}$ is the torque:

[1] The following derivation of the radial velocity of a binary system is based on the ideas described in Ramm (2004).

$$T = \frac{dJ}{dt} = \mu \frac{d}{dt}(\boldsymbol{r} \times \boldsymbol{p}) = \boldsymbol{r} \times \boldsymbol{F}\,. \tag{1.2.2}$$

Now $\boldsymbol{F}$ is the gravitational force acting parallel to the vector $\boldsymbol{r}$ and so their cross-product is zero, therefore angular momentum is conserved, assuming there are no external forces acting on the system.

The position of the body Q can be defined by the equation:

$$\boldsymbol{r} = X'\widehat{\boldsymbol{X}}' + Y'\widehat{\boldsymbol{Y}}' \tag{1.2.3}$$

therefore the velocity of Q is:

$$\mathrm{v} = \dot{X}'\widehat{\boldsymbol{X}}' + \dot{Y}'\widehat{\boldsymbol{Y}}' \tag{1.2.4}$$

Converting to polar coordinates in terms of r and θ (the true anomaly) :

$$\boldsymbol{r} = r\hat{\boldsymbol{r}}, \quad \hat{\boldsymbol{r}} = \begin{bmatrix}\cos\theta \\ \sin\theta\end{bmatrix}, \quad \hat{\mathbf{v}} = \begin{bmatrix}-\sin\theta \\ \cos\theta\end{bmatrix} \tag{1.2.5}$$

allows us to find the velocity:

$$\mathbf{v} = \dot{r}\hat{\boldsymbol{r}} + r\dot{\theta}\hat{\mathbf{v}} \tag{1.2.6}$$

and therefore the magnitude of the angular momentum as:

$$\|\boldsymbol{J}\| = \mu r^2\dot{\theta}. \tag{1.2.7}$$

If we then differentiate equation 1.2.6 with respect to time we can obtain the acceleration:

$$\ddot{r} = \mu\left(\ddot{r} - r\dot{\theta}^2\right)\boldsymbol{r} + \frac{\mu}{r}\frac{d}{dt}(r^2\dot{\theta})\mathbf{v}.$$

Now by Newton's second law $\left(\ddot{r} = \frac{1}{2}\frac{d(\dot{r}^2)}{dr}\right)$ and the conservation of angular momentum $\left(\frac{\mu}{r}\frac{d}{dt}(r^2\dot{\theta})\boldsymbol{\nu} = 0\right)$:

$$\mu(\ddot{r} - r\dot{\theta}^2) + F_g = 0. \tag{1.2.8}$$

Integrating equation 1.2.8 with respect to *r* gives:

$$\frac{\mu}{2}(\dot{r}^2 + r^2\dot{\theta}^2) + \int F_g\, dr = constant, \tag{1.2.9}$$

which represents the conservation of energy. Thus it can be seen that both energy and angular momentum are conserved, assuming no external forces act on the system.

The next step is to define the shape of the orbit by first taking Newton's law of universal gravitation (Newton, 1760) :

$$F_g(r) = \frac{GM_1M_2}{r^2}, \qquad U(r) = -\frac{GM_1M_2}{r}, \tag{1.2.10}$$

which tells us that the gravitational force of a mass decreases with the inverse square of the radius, where *G* is the universal gravitational constant. We also know that energy is conserved therefore the total energy (*E*) is equal to the sum of the kinetic energy and potential energy (*U*), giving:

$$E(r) = \frac{1}{2}\mu(\dot{r}^2 + r^2\dot{v}^2) - \frac{k}{r} \tag{1.2.11}$$

where $k = GM_1M_2$. Now we can make a substitution for $\dot{\theta}$ from equation 1.2.7 and solve for $\dot{r}$ to give the rate of change of *r* as:

$$\dot{r} = \sqrt{\frac{2}{\mu}\left(E - \frac{J^2}{2\mu^2r^2} + \frac{k}{r}\right)} \tag{1.2.12}$$

To integrate this equation we must first make the substitution $r = \frac{1}{h}$, $dr = -\frac{dh}{h^2}$, and $h^2 dt = \frac{\mu dv}{J}$, giving the integral:

$$dv = \int \frac{J}{\mu} \frac{dh}{\sqrt{2\mu E + 2\mu k h - J^2 h^2}}. \tag{1.2.13}$$

Integrating using the general formula $\int \frac{1}{1-u^2} \frac{du}{dx} dx = \cos^{-1} u$, gives:

$$\theta - \theta_0 = \cos^{-1} \left(\frac{\frac{J^2 h}{\mu k} - 1}{\sqrt{1 + \frac{2EJ^2}{\mu k^2}}} \right).$$

Substituting *h* back in and solving for $\frac{1}{r}$ gives:

$$\frac{1}{r} = \frac{1}{s}(1 + e\cos(\theta - \theta_0)), \tag{1.2.14}$$

where $s = \frac{J^2}{\mu k}$ and $e = \sqrt{1 + \frac{2EJ^2}{\mu k^2}}$. Equation 1.2.14 is the general form of a conic section where *e*, the eccentricity, measures the shape of an orbit. For an orbit to be real and bound then $-\frac{\mu k^2}{2J^2} \leq E < 0$, therefore $0 \leq e < 1$.

From this information we can say that all bound orbits have the shape of an ellipse which agrees with Kepler's first law and that the position of Q varies periodically as a function of v with a period (*P*) of 2π. There is also a special case of $e = 0$ which produces a circular orbit.

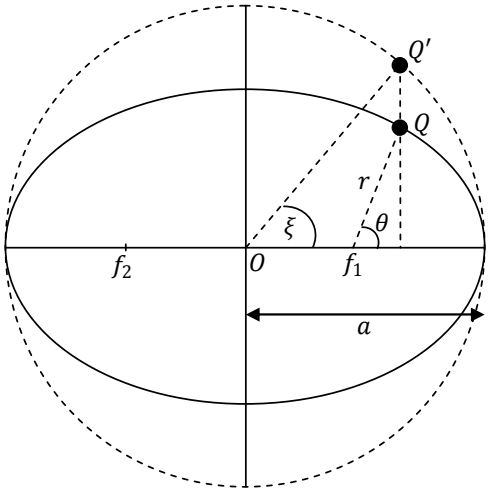

Figure 1.2.2 - *Diagram of an elliptical orbit projected onto a secondary circle for a two body system.*

Assuming an elliptical orbit we can determine the radial velocity of a body at any point in its orbit, but first the true anomaly (θ) needs to be found in terms of time. This is done by first projecting the elliptical orbit onto a circular orbit centred on **O** (shown in Figure 1.2.2) and then we define a new parameter called the mean anomaly (Φ) which is the angular fraction of a complete orbit if it were circular, defined as:

$$\Phi = \frac{2\pi}{P}(t - T), \tag{1.2.15}$$

where T is the time of periastron passage. We then introduce the eccentric anomaly (ξ) which has the same angular range and zero points as v but is centred at O and represents the position of Q on the auxiliary circle. ξ is related to v by the equation (Hilditch, 2001):

$$\tan\frac{\xi}{2} = \sqrt{\frac{1-e}{1+e}}\tan\frac{\theta}{2}. \tag{1.2.16}$$

Then we take Kepler's equation (Hilditch, 2001):

$$\xi_m = \Phi + e\sin\xi_{m-1}, \tag{1.2.17}$$

and by an iterative process ξ_m is calculated, where the first approximation is $\xi_1 = \Phi$.

Finally to find the radial velocity $\dot{z}$ we must project the orbital plane onto the sky plane which is done by a rotation matrix with rotation angle ψ:

$$R_x(\psi) = \begin{bmatrix} 1 & 0 & 0 \\ 0 & \cos\psi & -\sin\psi \\ 0 & \sin\psi & \cos\psi \end{bmatrix}. \tag{1.2.18}$$

To rotate the orbital plane (X', Y', Z') onto the sky plane (x, y, z) one rotation R_T is performed:

$$R_T = R_{Z'}(-\Omega) R_{X'}(-i) R_{Y'}(-\omega),$$

where Ω is the longitude of the ascending node, i the inclination, and ω the position angle of periastron passage. Therefore the rotated matrix is:

$$R_T = \begin{bmatrix} \cos\Omega & -\sin\Omega & 0 \\ \sin\Omega & \cos\Omega & 0 \\ 0 & 0 & 1 \end{bmatrix} \begin{bmatrix} 1 & 0 & 0 \\ 0 & \cos i & -\sin i \\ 0 & \sin i & \cos i \end{bmatrix} \begin{bmatrix} \cos\omega & -\sin\omega & 0 \\ \sin\omega & \cos\omega & 0 \\ 0 & 0 & 1 \end{bmatrix}$$

$$= \begin{bmatrix} \cos\Omega\cos\omega - \sin\Omega\sin\omega\cos i & -\cos\Omega\sin\omega - \sin\Omega\cos\omega\cos i & \sin\Omega\sin i \\ \sin\Omega\cos\omega + \cos\Omega\sin\omega\cos i & -\sin\Omega\sin\omega + \cos\Omega\cos\omega\cos i & -\cos\Omega\sin i \\ \sin i\sin\omega & \sin i\cos\omega & \cos i \end{bmatrix}.$$

Now we only need the $\dot{z}$ component ($Z' = 0$) represented by the third row of the matrix, giving:

$$\dot{z} = \dot{X}' \sin i \sin\omega + \dot{Y}' \sin i \cos\omega\,. \tag{1.2.19}$$

Then by the equations of an ellipse (Hilditch, 2001):

$$\dot{X}' = -a\,\dot{\xi}\sin\xi\,, \qquad \dot{Y}' = a\sqrt{1-e}\,\dot{\xi}\cos\xi, \tag{1.2.20}$$

where a is the sum of the semi-major axes ($a = a_1 + a_2$) and $\dot{\xi}$ is given by:

$$\dot{\xi} = \frac{2\pi}{P}\frac{1}{1 - e\cos\xi}, \tag{1.2.21}$$

equation 1.2.19 becomes:

$$\dot{z} = V_{\text{rel}} = \frac{2\pi a \sin i}{P(1 - e\cos\xi)}\left(\sqrt{1 - e^2}\cos\omega\cos\xi - \sin\omega\sin\xi\right).$$

Then substituting ξ from equation 1.2.16 allows us to obtain the relative radial velocity:

$$V_{\text{rel}} = \frac{2\pi\, a \sin i}{P\sqrt{1 - e^2}}(e\cos\omega + \cos(\theta + \omega))\,. \tag{1.2.22}$$

The semi-amplitude (K) can be seen to be:

$$K = \frac{2\pi\, a \sin i}{P\sqrt{1 - e^2}}. \tag{1.2.23}$$

Now to obtain the radial velocity observed in either star equation 1.2.22 can be separated into the two equations:

$$V_{\text{rel},1} = -\frac{2\pi\, a_1 \sin i}{P\sqrt{1 - e^2}}(e\cos\omega + \cos(\theta + \omega)),$$

$$V_{\text{rel},2} = \frac{2\pi\, a_2 \sin i}{P\sqrt{1 - e^2}}(e\cos\omega + \cos(\theta + \omega)),$$

where $V_{\text{rel},1}$ has a phase difference of π compared to $V_{\text{rel},2}$. One more factor that needs to be considered is that when a star is observed from the Earth the radial velocity will vary depending on where the Earth is in its orbit about the Sun relative to the star, the rotational rate of the earth, and the velocity of the Sun relative to its barycentre (Hilditch, 2001). This is called the Barycentric correction (BC). In addition, the velocity of the observed star system's barycentre through the Galaxy produces a Systemic radial velocity (γ), thus the radial velocity that we observe from the Earth can be represented by the equations:

$$V_1 = BC + \gamma - \frac{2\pi\, a_1 \sin i}{P\sqrt{1-e^2}}(e\cos\omega + \cos(\theta+\omega)), \tag{1.2.24}$$

$$V_2 = BC + \gamma + \frac{2\pi\, a_2 \sin i}{P\sqrt{1-e^2}}(e\cos\omega + \cos(\theta+\omega)). \tag{1.2.25}$$

To measure the radial velocity given by the above two equations, the Doppler effect is taken advantage of, whereby the wavelength of light (λ_0) emitted by a star is shifted to $\lambda_0 + \delta\lambda$ depending on the magnitude and direction of the radial velocity of the target star, defined by the equation (Doppler, 1846):

$$\frac{V_R}{c} = \frac{\lambda_{obs} - \lambda_0}{\lambda_0}. \tag{1.2.26}$$

The wavelengths of light are measured using a spectrograph and then compared to some reference spectrum to determine the wavelength change, and thus the radial velocity is obtained.

From equation 1.2.23 one can estimate the radial velocity semi-amplitude that would be seen for different semi-major axes and masses of the secondary body, which is shown in Table 1.1 below for a circular orbit about a solar mass primary star with orbital inclination $i = 90^\circ$.

		$\mathbf{1}\, M_{Sun}$	$\mathbf{0.5}\, M_{Sun}$	$\mathbf{3}\, M_{Jupiter}$	$\mathbf{1}\, M_{Jupiter}$	$\mathbf{1}\, M_{Earth}$
***a* (AU)**	***P* (d)**	km/s	km/s	m/s	m/s	m/s
0.5	129.14	62.561	31.280	179.35	59.78	0.19
1.0	365.25	31.280	15.640	89.67	29.89	0.09
1.5	671.01	20.853	10.426	59.78	19.94	0.06
2.0	1033.08	15.640	7.820	44.83	14.95	0.05
2.5	1443.78	12.512	6.256	35.87	11.96	0.04

Table 1.1 - *Table of estimated semi-amplitudes for different masses at different semi-major axes from the primary star.*

Table 1.1 tells us that the Doppler method can easily detect very massive bodies such as other stars orbiting the target star, since most high resolution spectrometers have a preci-

sion of at least 20 m/s. Jupiter-mass giant planets are also reasonably easy to detect depending on their mass and distance from the host star, but some spectrographs may struggle to detect them past 2.5 AU, owing to the perturbations being on a similar scale to the uncertainty in the observations.

β Gem is an example of a K giant star which has been observed to host a 2.3 M_{Jupiter} planet detected by the Doppler method. The 41 ms^{-1} RV perturbation with a period of 558 days was first discovered by Hatzes and Cochran (1993), where they observed a consistent sinusoidal pattern from 1980 - 1993, and is shown in the top plot of Figure 1.2.3. However, three other similar K giant stars observed in the same study exhibited similar behaviour, leaving the possibility that the perturbation was intrinsic to the star (e.g. rotational modulation or pulsation). The presence of a consistent planetary RV perturbation was later confirmed by Hatzes, Cochran et al. (2006) to have a period of 589.64 ± 0.81 days, an eccentricity of 0.02 ± 0.03, and a semi-major axis of 1.64 ± 0.27 AU, resulting in the lower RV curve of Figure 1.2.3.

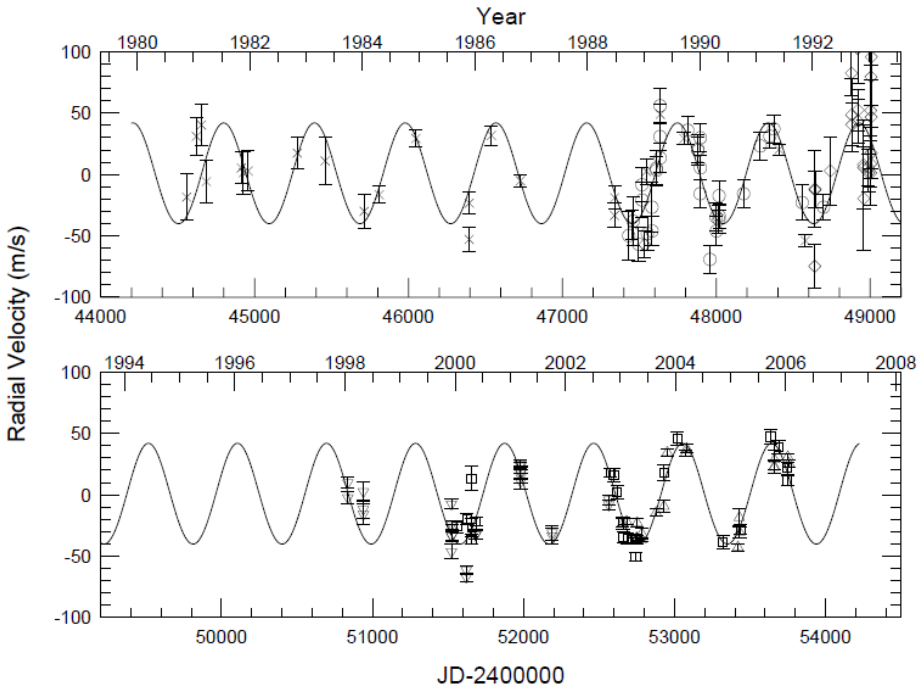

Figure 1.2.3 - *Radial velocity measurements for β Gem from the 6 data sets: CFHT (crosses), DAO (diamonds), McD-2.1m (circles), McD-cs21 (inverted triangles), McD-MOPS (squares), and TOPS (triangles). (Hatzes, Cochran, Endl et al., 2006).*

The Doppler method is a very popular method for detection of exoplanets because of its precision and simplicity. Currently some of these groups are: AFOE, Anglo-Australian Planet Search Program, Automated Planet Finder, Carmenes, Coralie at Leonard Euler Telescope, Mt John Observatory, Elodie, ESO Coude Echelle Spectrometer, Exoplanet Tracker, High Accuracy Radial velocity Planetary Search (HARPS), Hobby-Eberly Telescope, Magellan 6.5 m Telescope, Mc Donald Observatory, N2K Consortium, Sophie, SARG, and UVES.

1.3 Other Indirect Methods of Detection

1.3.1 The Transit Method

When a planet passes in between an observer and its host star some of the light is blocked by the planet, casting a shadow on the observer. The effect has been observed numerous times in our own solar system when either Mercury or Venus pass between the Earth and the Sun. Transits within our own solar system are relatively easy to observe as the planet itself can be seen passing in front of the Sun, but in the case of a distant star the transit can only be measured indirectly via the change in brightness of the star with time giving a light curve similar to Figure 1.3.1.

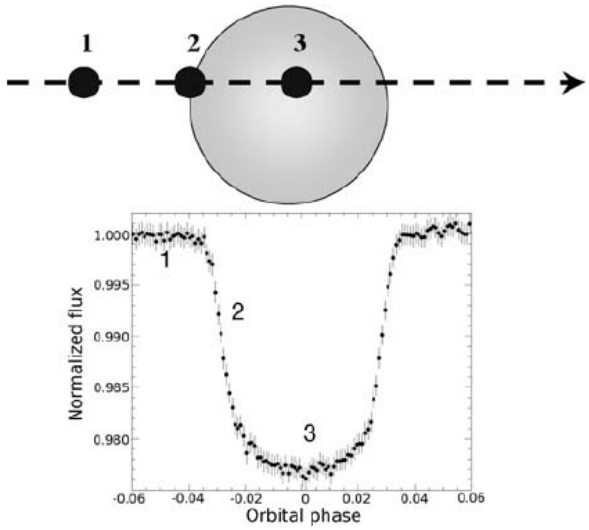

Figure 1.3.1 - *Diagram illustrating a planetary transit and the associated photometric light curve (Ollivier, Encrenaz et al., 2008).*

The relative amplitude of the photometric decrease during a transit, to a first approximation, is equal to the ratio of the apparent projected surfaces of the planet and star and may be written as:

$$\frac{\Delta F}{F} = \frac{r_p^2}{r_*^2} \tag{1.3.1}$$

where r_p and r_* are the radii of the planet and star respectively, and F is the flux (Ollivier, Encrenaz et al., 2008). In the case of a Jupiter-sized planet orbiting a Sun-like star, there is a 1 per cent (10^{-2}) reduction in stellar flux and for an Earth-sized planet a 0.01 per cent (10^{-4}) reduction. For a planetary transit to be detected one needs to carry out photometry better than the relative photometric dip. Ground based photometry can reach a precision of 10^{-3} under the effects of atmospheric turbulence, and therefore to reach a precision of 10^{-5} space based observations are required.

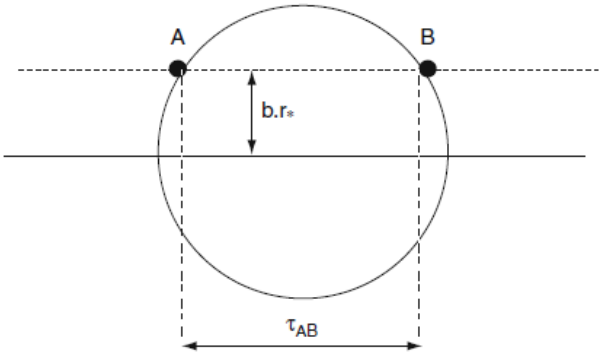

Figure 1.3.2 - *The geometry of a transit (Ollivier, Encrenaz, Roques et al., 2008).*

While the magnitude of the dip helps to determine the size of the planet, timing multiple transit durations (τ_{AB}) is used to determine the period (P) and semi-major axis (a_p) of the planetary orbit. Figure 1.3.2 shows the geometry of a transit which allows the derivation of the relationship between τ_{AB} and the period or semi-major axis, written as:

$$\tau_{AB} = \frac{2r_*\sqrt{1-b^2}}{(GM_*)^{1/2}} a_p^{1/2} = \frac{(2\pi)^{2/3}\, 2r_*\sqrt{1-b^2}}{(GM_*)^{1/3}} P^{1/3}\,, \qquad (1.3.2)$$

where b is the impact parameter and M_* the mass of the star (Ollivier, Encrenaz et al., 2008). It can be concluded from equation 1.3.2 that larger periods or semi-major axes produce longer transit times.

One of the conditions for a transit to occur is that the observed system is very close to edge-on with respect to the observer. One can estimate the probability of a transit, assum-

ing a circular orbit, by considering the ratio between a sphere of radius a_{p} to a cylinder of radius a_{p} and height $2r_*$ (Ollivier, Encrenaz et al., 2008). Therefore the probability can be written as:

$$p_{\mathrm{T}} = \frac{r_*}{a_{\mathrm{p}}} = \frac{r_*}{P^{2/3}}\left(\frac{4\pi^2}{GM_*}\right)^{1/3} . \qquad (1.3.3)$$

From equation 1.3.3 one can calculate the probability of a hot Jupiter around a Sun-like star to be 10 per cent and for an Earth-like planet to be 0.5 per cent. Therefore it can be concluded that the transit method is most efficient at detecting large planets close to their host star.

Even though the probability of a transit is low, this can be compensated for by performing wide field surveys of many thousands of stars at once. The NASA Kepler mission which consists of a 0.95 m space telescope attached to a photometer, can observe 105 square degrees of the sky containing over 100,000 stars and is a current example of a wide-field survey (Borucki, Koch, Basri et al., 2003). As of February 27 2012, 2321 candidate planets and 74 confirmed planets have been observed in just 3 years. Kepler22-b, discovered in the Kepler mission, is an interesting case since it is a 2.4 Earth-radius planet orbiting a Sun-like star in the habitable zone with a period of 290 days (Borucki, Koch et al., 2011), being the most Earth-like analogue discovered to date. Figure 1.3.3 shows the light curve of Kepler22-b.

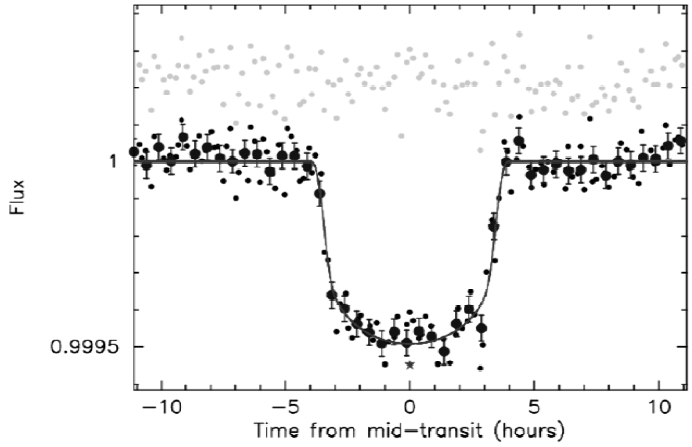

Figure 1.3.3 - *Photometric light curve of Kepler 22-b (Borucki, Koch, Batalha et al., 2011).*

1.3.2 Gravitational Microlensing

Suppose we have a foreground (lens) star which passes between an observer and some background (source) star. By Einstein's theory of relativity a photon emanating from the source star and passing the lens star at radius (r) will undergo a path deviation (α) because of the gravitational field of the lens star (Einstein, 1936), that is, light that would normally miss the observer will instead focus at the observers location. Now assuming a point mass, the deviation can be expressed as (Ollivier, Encrenaz et al., 2008):

$$\alpha = \frac{4GM_*}{c^2 r}. \tag{1.3.4}$$

From equation 1.3.4 it can be concluded that if a massive object lies between the observer and source star the image of the source is thus deformed depending on the mass and the position from the lens star relative to the observer.

In the case where the angular deviation is larger than the instruments diffraction disks then an odd number of secondary-images appear around the lens star, known as an Einstein ring. This is called macrolensing (Ollivier, Encrenaz et al., 2008). When the angular deviation is less than the instruments diffraction disks the effect is an overall amplification in

intensity of the source star, and when measured a symmetric light curve, similar to the main curve in Figure 1.3.4, is observed. This is defined as microlensing.

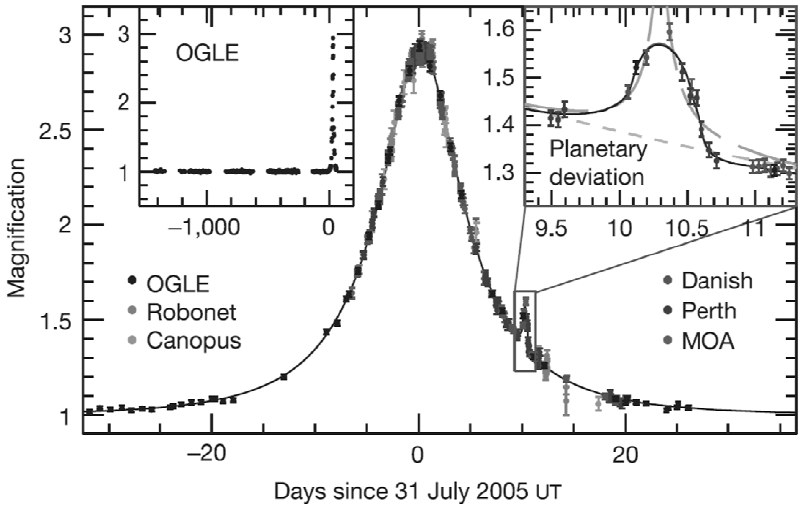

Figure 1.3.4 - *Photometric light curve of OGLE-2005-BLG-390Lb (Beaulieu, Bennett, Fouque et al., 2006).*

If a planet is orbiting the lens star then a small but noticeable brightening will occur in addition to the main light curve because of the planet's gravitational field. From the observed magnification of the planet one can accurately calculate the mass ratio of the planet to that of the star. Furthermore, the separation between the lens and planet can be determined from the time difference between the two events. OGLE-2005-BLG-390Lb in Figure 1.3.4 shows the microlensing effect of a 5.5 Earth-mass planet 2.6 AU from an M-dwarf star (Beaulieu, Bennett et al., 2006).

The main advantage of microlensing is that, in principle, it is extremely sensitive and enables giant planets to be detected reasonably easily, for example, OGLE-2005-BLG-71 which has a mass of 3.5 Jupiter masses (Udalski, Jaroszy'ski, Paczy'ski et al., 2005). This method can also detect lower mass planets (terrestrial planets), for example, MOA-2004-BLG-192 with a mass of 3.3 Earth masses (Bennett, Bond, Udalski et al., 2008), the smallest planet to date detected by Microlensing.

The disadvantage of Microlensing is that the probability of an alignment between the observer and two distant stars is very low, but is compensated from by performing wide-field observations of dense star fields, thus increasing the chance of an alignment dramatically.

Current Projects in the area are; MOA, OGLE III, PLANET, ROBONET, UStAPS, LCOGT, MicroFUN, and MPS (Schneider, 2012).

1.3.3 The Pulsar Timing Method

Pulsars are highly magnetised, rotating neutron stars which emit beams of electromagnetic radiation. They can only be seen when the beam is pointing directly at Earth, similar to the way a light house is only seen when the light points directly at the observer. Neutron stars are very dense, and have short, regular rotational periods that produce very precise intervals between pulses on the magnitude of a few milliseconds to a few seconds.

If a planet is orbiting a pulsar, the star and planet must orbit their barycentre. Now as the star 'wobbles' the Earth-pulsar distance increases and decreases, thus increasing and decreasing the travel time for the pulsar's signal to reach Earth. This variation in the travel distance, and thus the travel time, is indicated by the period of the pulsar over the course of time. Assuming the pulsar describes an orbit with a semi-major axis a_{planet} about the centre of mass, inclined at angle i to the sky plane, then the variation in the pulsar's period can be expressed as (Ollivier, Encrenaz et al., 2008):

$$\delta T_* = \frac{m_{\text{planet}}\, a_{\text{planet}}}{m_{\text{star}}\, c} \sin i, \tag{1.3.5}$$

where c is the speed of light. Equation 1.3.5 can be used to estimate what one might measure in the variation of a pulsar, for example, a Jupiter-mass planet orbiting a solar-mass pulsar with a semi-major axis of 5.2 AU would cause a variation of 250 ms, while an Earth-mass planet with a semi-major axis of 1 AU would cause a 0.15 ms variation. The periods of pulsars can easily be measured to a precision of milliseconds, and thus this method has the capability of detecting moon-sized bodies around pulsars.

The first confirmed extrasolar planets in the system PSR1257+12 were detected by the pulsar timing method in 1992 (Wolszczan and Frail, 1992). To date, three planets have been found in this system which produce the residual time of arrival (TOA) variations shown in Figure 1.3.5. Planet A orbits the pulsar with a period of 25.3 days with a mass of 0.020 Earth masses, Planet B orbits the pulsar every 66.5 days with a mass of 4.3 Earth masses,

and planet C has a mass of 3.9 Earth masses orbiting the pulsar every 98.2 days (Konacki and Wolszczan, 2003). As of Dec 2011 only 15 planets have been detected via pulsar timing which may be due to the fact that pulsars do not contain a very hospitable environment for life to exist and therefore not many groups feel inclined to use this method.

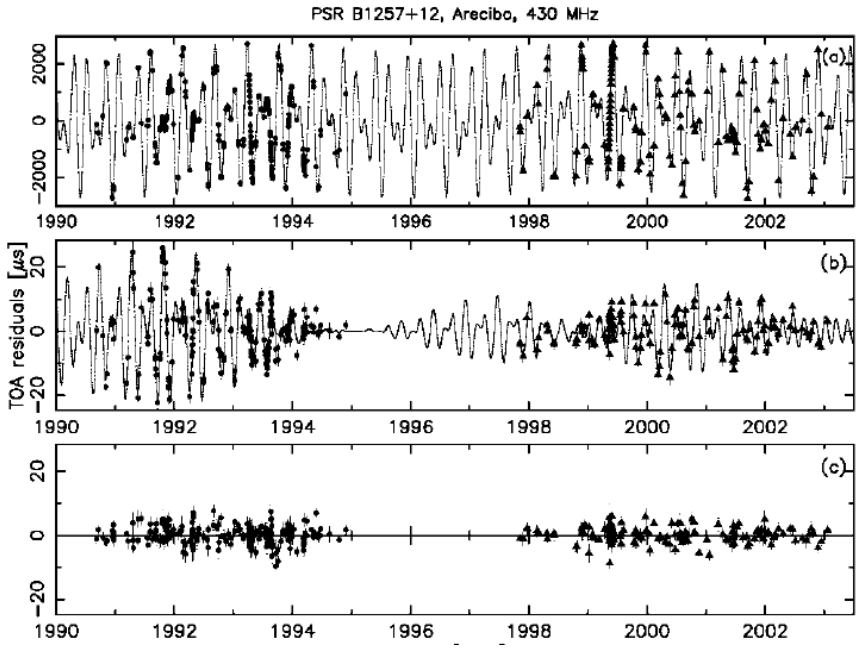

Figure 1.3.5 - *TOA residuals after the fit of the standard timing model without planets. TOA variations are dominated by the Keplerian orbital effects from planets B and C. (b) TOA residuals for the model including the Keplerian orbits of planets A, B, and C. Residual variations are determined by perturbations between planets B and C. (c) Residuals for the model including all the standard pulsar parameters and the Keplerian and non-Keplerian orbital effects (Konacki and Wolszczan, 2003).*

1.4 Giant Planets

Giant planets can be defined as planets mostly made of hydrogen and helium and are too light to ignite deuterium fusion. It is fortunate that our solar system contains four giant planets (Jupiter, Saturn, Uranus, and Neptune) which has enabled them to be studied in great detail.

Giant planets, as the name suggest, are very massive and in the case of our solar system the masses are shown in Table 1.2. However their densities are much smaller relative to terrestrial planets (3.9 - 5.5 $g\,cm^{-3}$) ranging from 0.69 - 1.64 $g\,cm^{-3}$ (Guillot and Gautier, 2009). When considering how compression strongly increases with mass, one is naturally led to the conclusion that Jupiter/Saturn like planets consist of an important proportion of light elements, while less massive Neptune/Uranus planets contain a larger proportion of heavier elements and can be sub-classified as 'sub-giants' or 'ice-giants'.

Planet	Mass (Earth masses)
Jupiter	317.834
Saturn	95.161
Uranus	14.538
Neptune	17.148

Table 1.2 - Solar system giant planet masses (Guillot and Gautier, 2009).

The giant planets in our solar system are also found to be very fast rotators with a period of ~10 h for Jupiter/Saturn and ~17 h for Neptune/Uranus (Seidelmann, Archinal, A'Hearn et al., 2007). This visibly affects the shape of the planets where significant differences between the polar and equatorial radii have been observed. However, because of the fluidic nature of these planets atmospheric zonal winds, different latitudes rotate at different velocities, in fact, the magnetic field also produces another rotational frame (Guillot and Gautier, 2009).

Magnetic fields of giant planets are generally dipolar with axes close to the rotational axes. It is thought that they are generated by a dynamo mechanism related to interior convection (David 2003). In the case of Jupiter and Saturn, their magnetic fields are very symmetric and have dipole moments of 4.27 Gauss R_J^3 (Connerney, Ness and Acuna, 1982) and 0.21

Gauss R_S^3 (Acuña, Connerney and Ness, 1983) respectively, while the ice-giants Uranus and Neptune contain very complex magnetic fields with dipole moments 0.23 Gauss R_U^3 (Ness, Acuna, Behannon et al., 1986) and 0.133 Gauss R_N^3 (Ness, Acuna, Burlaga et al., 1989) respectively.

Hydrogen and helium are the most important components of giant planets, but owing to their inefficiency in absorbing visible and infrared light it is therefore difficult to detect. The Galileo probe which was dropped into a dry region of Jupiter's atmosphere (von Zahn, Hunten and Lehmacher, 1998) measured the helium mole fraction to be $q_{He} = 0.1359 \pm 0.0027$ (number of He atoms over the total number of species in a given volume). Since the mixing ratio of He (Y) is constrained by the ratio of hydrogen (X) we can imply that $X = 0.238 \pm 0.05$, which by coincidence is the same as in the Sun's atmosphere, but because of He sedimentation in the Sun's radiative zone it was larger in the proto-solar nebula ($X_{proto} = 0.275 \pm 0.01$) (Bahcall, Pinsonneault and Wasserburg, 1995). The heavy elements that have been detected in our giant planets are; oxygen, carbon, nitrogen, and sulphur, which exist in the upper troposphere as molecules of CH_4 , NH_3, H_2S, and H_2O (Fegley Jr and Lodders, 1994).

Another feature of our giant planets is that they emit more radiation than they receive from the Sun, for example, Jupiter absorbs 50.14×10^{16} Js^{-1} from the Sun but emits 83.65×10^{16} Js^{-1} (Lindal, Wood, Levy et al., 1981). This can be explained by the progressive contraction and cooling of the planets as explained in Hubbard (1968), and a crucial consequence of the presence of an intrinsic heat flux is that it requires high interior temperatures (+10,000 K) and as a result giant planets are 'fluid'. Their atmospheres have been observed to be close to adiabatic and have temperature profiles as shown in Figure 1.4.1, where the stratosphere has a negative gradient (i.e. increasing temperature with decreasing pressure) and the troposphere a positive gradient (Hubbard, 1968). It has also been observed that in all four cases when the atmosphere becomes convective at a few tens of bar the temperature gradient becomes almost constant, suggesting an almost linear increase in temperature with depth.

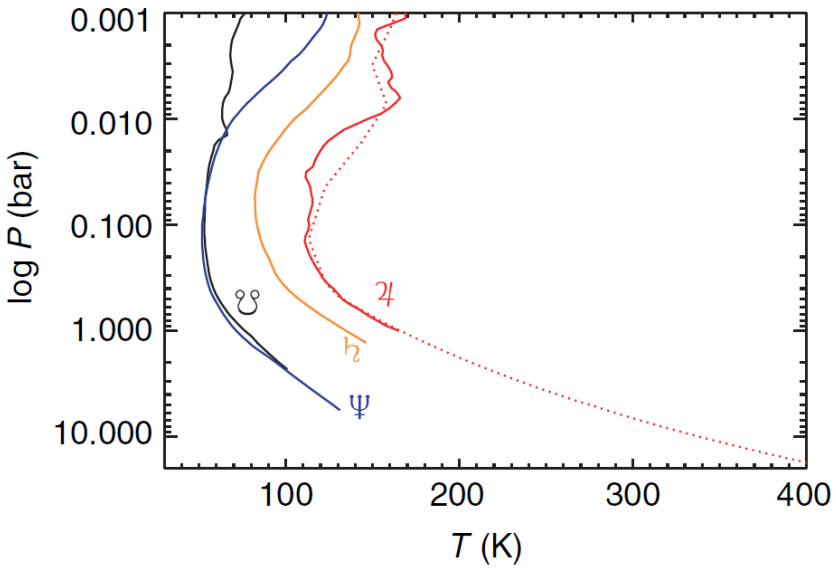

Figure 1.4.1 - *Atmospheric temperatures as a function of pressure for Jupiter, Saturn, Uranus, and Neptune, as obtained from Voyager radio-occultation experiments. The dotted line corresponds to the temperature profile retrieved by the Galileo probe, down to 22 bar and a temperature of 428K (Guillot and Gautier, 2009).*

The atmospheres of giant planets are very complex and turbulent in nature. The mean zonal winds vary rapidly as a function of latitude (Ingersoll, Barnet, Beebe et al., 1995), while some regions rotate at the same speed as the magnetic field, most atmospheres do not. In the case of Jupiter and Saturn they have superrotating equators at velocities of +100 ms^{-1} and +400 ms^{-1} (Guillot and Gautier, 2009) respectively (inferred by cloud tracking). Uranus and Neptune have both superrotating equators and high latitude jets, with latitudinal wind variations of about 600 ms^{-1} (Ingersoll, Barnet et al., 1995). The surface winds are thought to be related to the motions of the planet's interiors, which, according to the Taylor-Proudman theorem (Proudman, 1916; Taylor, 1917), should be confined by the rapid rotation of the planet perpendicular to the axis of rotation (Busse, 1978). To date no model is yet capable of modelling with sufficient accuracy both the interior and surface layers.

Storms on giant planets can range from planetary-scale down to small-scale with very different temporal variations. For example, Jupiter's great red spot is 12,000 km in diameter and has lasted for at least 300 years (Simon-Miller, Gierasch, Beebe et al., 2002), and planetary-scale storms have been observed forming on Saturn (Sanchez-Lavega,

Lecacheux, Gomez et al., 1996). These storms however rely on the abundance of the important condensing chemicals: ammonia and water for Jupiter and Saturn, and methane for Uranus and Neptune. These species may only condense in cold atmospheres thus providing latent heat to fuel storms, and therefore hot exoplanets may not produce these storms (Guillot, 1999).

A discussion on giant planets is incomplete without mentioning the moons and rings these planets possess. The satellites/moons can be distinguished from their orbital characteristics as regular, with circular prograde orbits, or irregular, with eccentric, and/or retrograde[2] orbits. Currently 67, 62, 27, and 13 satellites for Jupiter, Saturn, Uranus, and Neptune respectively have been discovered (Sheppard, 2012). In the case of Jupiter, there 15 satellites in a prograde orbit all within 0.013 AU, and 52 satellites in retrograde orbits which all have semi-major axes greater than 0.013 AU. In the case of Saturn there are 41 satellites in prograde orbits with semi-major axes less than 0.012 AU and 21 satellites in retrograde orbits with semi-major axes greater than 0.012 AU. Saturn is a good example for rings around giant planets, where their considerable size allows them to reflect a sizable fraction of solar flux, making the rings as bright as the planet itself. It is believed that regular satellites and rings were mostly formed in the protoplanetary subnebulae surrounding the giant planets at the time they accreted their envelopes, whereas, the irregular satellites are thought to have been captured by the planet.

[2] Orbital motion in the opposite direction to the rotational direction of the host planet.

Chapter 2

ν Octantis

2.1 Properties of ν Octantis

ν Octantis is a single-lined spectroscopic binary system where the primary star ($21^h41^m29^s$, $-77^\circ23^m24^s$) has had its spectral type classified as K0III (Houk, 1978). The V magnitude has been measured to be V = 3.743 ± 0.015 mag (Mermilliod, 2006), and the *Hipparcos* parallax ϖ = 47.18 ± 1.93 mas (van Leeuwen, 2007). Thus the distance to ν Octantis is 27.20 ± 0.87 pc and the absolute magnitude is M_V = +2.10 ± 0.13 mag. ν Octantis has been determined to be photometrically stable by 133 *Hipparcos* observations, where H_P = 3.8981 ± 0.0004. The metallicity of ν Octantis has also been estimated to be [Fe/H] = −0.11 (Eggen, 1993). Table 2.1 shows the V magnitude and some colour indices for ν Octantis.

Parameter (mag)	ν Oct
V	3.743 ± 0.015
M_V	+2.10 ± 0.13
$(B-V)$	0.992 ± 0.004
$(U-B)$	0.898 ± 0.004
$(R-I)_C$	0.465 ± 0.020
$(V-I)_C$	0.985 ± 0.020

Table 2.1 - *The V magnitude and some colour indices for ν Oct. V, (B-V), (U-B) from Mermilliod (2006), and Cousins indices from Bessel (1990).*

Spectral type K stars generally have weak H lines, if they are present at all, and their spectra show mostly natural metals such as Ca, Fe, and Si. Their effective temperatures can range from 3000 - 5200 K, and in the case of the ν Octantis primary star the effective temperature (T_{eff}) can be estimated by a metallicity dependent temperature versus $(R-I)_C$ calibration for giant stars, derived by Ramírez and Meléndez (2005). They report a 1σ dispersion of about 60 K and so along with the photometric uncertainty the effective temperature of the primary can be estimated as $T_{\text{eff}} = 4815$ K.

In general, many giant stars are located in a region of the Hertzsprung Russell diagram called the red clump (RC). Stars in this region have reached the stage in their evolution where most of the hydrogen has been fused to helium, which accumulates in a helium-rich core held together by electron degeneracy pressure. A shell of hydrogen, which expands and cools over time, continues to fuse into helium about the core. Over this stage of the star's life its brightness remains reasonably constant in the K band (Böhm-Vitense, 1992). Van Helshoecht (2007) discusses how RC giants can be used as distance indicators and have derived a mean RC-star M_K value of $\langle M_K \rangle_{RC} = -1.57 \pm 0.05$. In the case of the primary star of ν Octantis, $K = 1.458 \pm 0.306$ mag (Cutri, Skrutskie, van Dyk et al., 2003), and therefore M_K can be estimated to be $M_K = -0.17 \pm 0.32$ mag. Consequently, the primary star is significantly less luminous in the K band than a typical RC-star.

The luminosity (L) of the ν Octantis primary star can be calculated by the equation:

$$M_{\text{bol},*} - M_{\text{bol},\odot} = -2.5 \log\left(\frac{L}{L_\odot}\right), \qquad (2.1.1)$$

where $M_{\mathrm{bol},*}$ and $M_{\mathrm{bol},\odot}$ are the bolometric magnitudes of the ν Octantis primary and the Sun respectively. $M_{\mathrm{bol},*}$ can be calculated using the calibration relation of Bessell and Wood (1984) with the value for $(\mathrm{V}-\mathrm{I})_{\mathrm{C}}$, giving

$$\mathrm{BC} = 0.3 - 0.62(\mathrm{V}-\mathrm{I})_{\mathrm{C}} - 0.14(\mathrm{V}-\mathrm{I})_{\mathrm{C}}^{2}, \qquad (2.1.2)$$

valid for all late type stars. Thus for the ν Octantis primary star BC = -0.45 ± 0.02 and $M_{\mathrm{bol},*} = +1.65 \pm 0.03$, resulting in a luminosity of $L \cong 17\ L_{\odot}$.

The radius of the ν Octantis primary star can be estimated from the effective temperature and bolometric magnitude by the equation:

$$\log\frac{R}{R_{\odot}} = \frac{4.74 - M_{\mathrm{bol},*}}{5} - 2\log\frac{T_{\mathrm{eff}}}{T_{\odot}}, \qquad (2.1.3)$$

where $T_{\odot} = 5780$ K. Therefore the radius of the ν Octantis primary star is $R = 6.0 \pm 0.3\ R_{\odot}$.

The precise age of an evolved star such as the ν Octantis primary can be difficult to determine since the RC region consists of stars with different metallicities and ages. One can estimate the age by comparing its location on the colour-magnitude diagram (CMD) to isochrones generated by the Geneva group (Lejeune and Schaerer, 2001) stellar models, which indicated an age of 2.5 - 3 Gyr for the ν Octantis primary (Ramm et al. (2009)) .

The first RV's of ν Octantis were derived from eleven Chilean spectra taken between 1904 - 1920 (Campbell and Moore, 1928) and ten Cape spectra between 1909 - 1924 (Jones, 1928). The orbital solution for these data was first determined by Colacevich (1935) and Christie (1936), both shown in Table 2.2. Ramm et al. (2009) also found a revised orbital solution for the same data set using modern fitting methods, which is also shown in Table 2.2 as historical RVs.

Table 2.2 - *The orbital elements of Historical and Mt John University Observatory spectroscopic observations for ν Octantis.*

ν Octantis	K_1 (kms^{-1})	e	ω_1 (°)	$T_{0,1}$ (24...)	T (24...)	P (d)	γ (kms^{-1})	$a_1 \sin i$ (Gm)	f_{M1} $(M_\odot)$	Fit rms (kms^{-1})
Colacevich (1935)	8.0	0.25	90	-	17506	1037	+35.7	110.4	0.050	0.85
Christie (1936)	8.0	0.4	80	-	18525	1020	+34	-	-	-
Historical RVs	7.95	0.401	82	18289	18534	1037	+34.17	103.9	0.042	1.4
±	0.90	0.084	14	18	26	5	0.4	8.7	0.011	
Ramm et al. (2009) keplerian + perturbation	7.0516	0.23603	74.30	52959.74	53176.47	1050.15	-	98.952	0.035010	0.036
±	0.0049	0.00054	0.14	0.10	0.36	0.23	-	0.067	0.000067	
Ramm et al. (2009) Primary keplerian	7.0323	0.23588	75.051	52959.817	53178.74	1050.11	35.237	98.682	0.034727	0.019
±	0.0026	0.00028	0.075	0.054	0.19	0.13	0.020	0.036	0.000035	
Ramm et al. (2009) Perturbation	0.0518	0.123	260	52581.4	52882	417.4	0.0073	0.2951	5.88×10^{-9}	0.019
±	0.0016	0.037	21	3.7	24	3.8	0.0015	0.0097	0.58×10^{-9}	

The mass of the ν Octantis primary star was also estimated in Ramm et al. (2009) by comparing the position of the primary on the CMD with respect to model evolutionary tracks for different masses at solar metallicity, provided by the Geneva group (Lejeune and Schaerer, 2001). Thus the primary was determined to have a mass of approximately $1.4 \pm 0.3\ M_{\odot}$. The secondary star was estimated to have a mass of $0.5 \pm 0.1\ M_{\odot}$, which was derived from the mass function (f_{M1}), the primary's mass, and the inclination ($70.8 \pm 0.9°$) of the system through equation 2.1.4:

$$\frac{q^3}{(1+q)^2} = \frac{f_{M1}}{M_1 \sin^3 i}, \tag{2.1.4}$$

where $q = M_2/M_1$. From the mass of the secondary (M_2) one can estimate the spectral type to be between K7 and M1, where M0 is the mean and is approximately 7 magnitudes dimmer than the primary star. Kepler's third law allows us to estimate the semi-major axis of the binary as $a_{bin} = 2.55 \pm 0.13$ AU.

2.2 Possible Planetary Perturbation in the RVs of ν Octantis

According to Ramm et al. (2009) (first mentioned in Ramm (2004)) when the solution to the binary's orbit is subtracted from the RVs obtained between 2001-2007 an extra sinusoidal perturbation is revealed, which has a period of approximately 413 days based on a periodogram and appears to be in a 5:2 period resonance with the binary's period. The residual RV after a single keplerian fit is shown in Figure 2.2.1(b), which clearly shows the presence of a perturbation. The cause of the perturbation could be a result of rotational modulation of surface features, radial and/or non-radial pulsations, and/or the presence of an orbiting body, or due to the presence of another close binary system (see Section 2.4).

Over the period of six years over which the RVs have been recorded, the perturbation has had RV behaviour that is more or less coherent, and the phase has remained the same. This

is consistent for an orbiting body or pulsations, but provides less support for surface features such as star-spots, which are known to vary in size, number, and location over much shorter time spans. However, long-lived star-spots have been known to exist, for example, ξ Boo A (Toner and Gray, 1988) had a star-spot with a period of 6.4 days which lasted for at least three years. Therefore more evidence is still needed to rule star-spots out.

Photometry of ν Octantis was not acquired during the acquisition of spectra in Ramm et al. (2009) and so it can only be assumed, based on 133 Hipparcos observations, that ν Octantis is photometrically stable, since $H_P = 3.8981 \pm 0.0004$ (van Leeuwen, 2007). ROSAT observations were also taken during the same period as Hipparcos (Huensch et al. (1996)) and determined that ν Octantis is also stable in the x-ray regime. However, it is entirely possible that ν Octantis was in a less active phase of its behaviour during both the Hipparcos and ROSAT observations. If we are to assume ν Octantis remained quiet during the acquisition of its spectra, this is strong evidence that radial pulsations and rotational modulation of surface features are not the cause of the perturbation. However, according to Ramm et al. (2009) this does not rule out non-radial pulsations, as photometric stability and the size of the perturbation is consistent with both non-radial pulsations and/or an orbiting body.

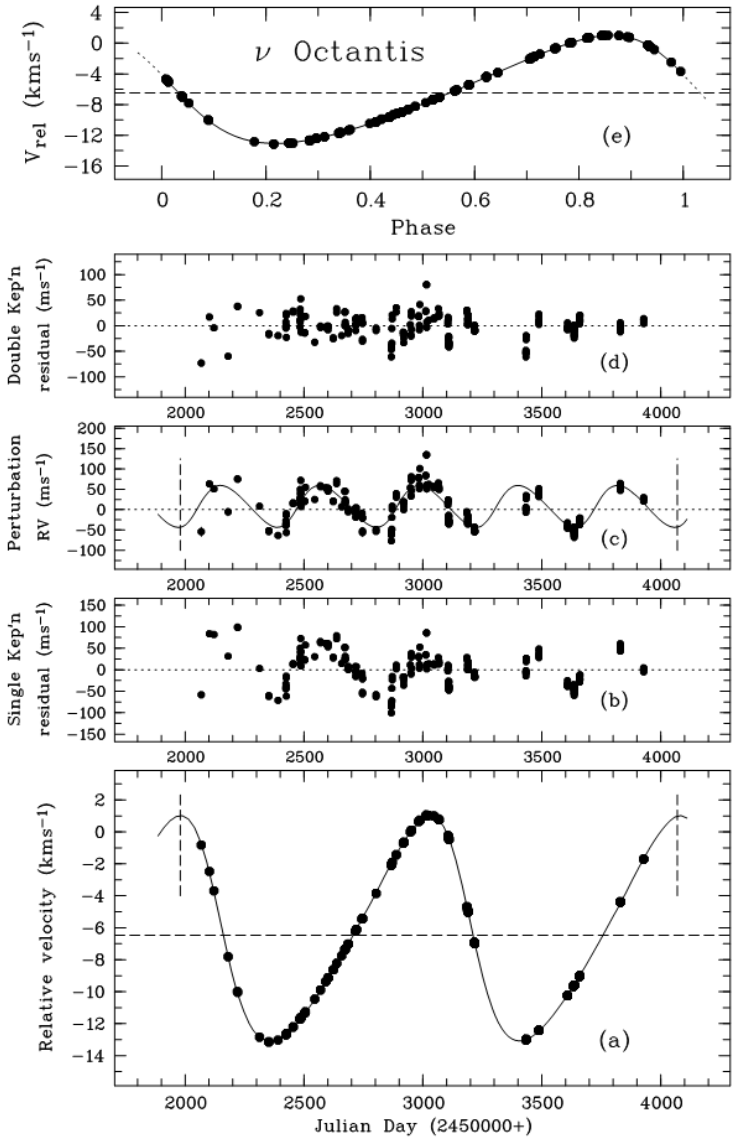

Figure 2.2.1 - *(a) the relative radial velocity of v Oct obtained from spectra between June 2001 to July 2006. (b) Residual radial velocity after a single Keplerian fit. (c) Perturbations derived using a double Keplerian fit, including the corresponding best fit curve. (d) Double Keplerian-fit residuals. (e) Phase plot of Primary stars radial velocity, where the zero-point corresponds to the time of periastron passage, T (Ramm, Pourbaix et al., 2009).*

Asymmetric spectral lines can be attributed to stellar processes such as radial or non-radial pulsations, rotational modulations, or patches and active regions. To measure asymmetries in spectral lines one can use the bisector analysis technique (see Gray, 1983). Ramm et al. (2009) used this technique by analysing the cross-correlation function of all the spectra

used for RV determination (Santos et al. (2001)) and found no correlation between the RV perturbation and the bisector velocity span, shown in Figure 2.2.2. Therefore is can be concluded that, to within the precision of the spectrograph, non-radial pulsations and rotational modulation of star-spots are unlikely to be the cause of the perturbation (Ramm et al. (2009)).

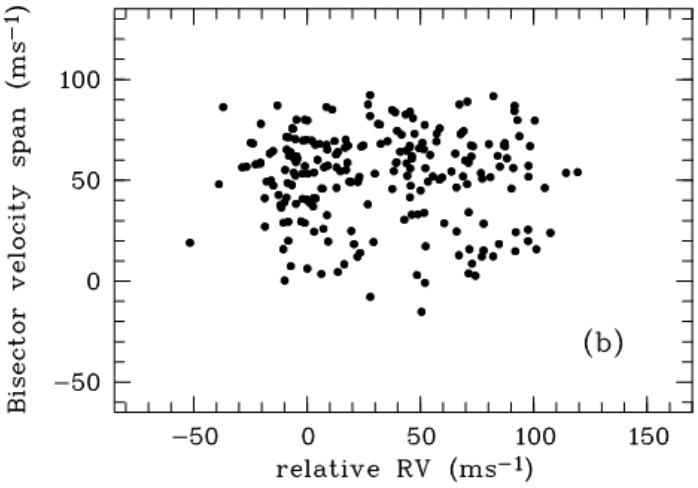

Figure 2.2.2 - *Bisector velocity span as a function of the perturbations velocities (Ramm, Pourbaix, Hearnshaw and Komonjinda, 2009).*

Rotational modulation of surface features, radial pulsations, and non-radial pulsations have all been ruled out by Ramm et al. (2009) to within the precision of the spectrograph, leaving the only possible cause of the perturbation to be a third body orbiting the primary star of ν Octantis. Figure 2.2.1(c) shows the planetary perturbation for which Ramm et al. (2009) derived an orbital solution by first fitting a keplerian solution to the binary's orbit, which is then subtracted so that another keplerian solution can be fitted to the perturbation. This is then subtracted from the binary's RVs so as to fit a more accurate orbital solution to the binary's orbit. This is repeated until convergence of the orbital elements is achieved. The elements of the perturbation are also given in Table 2.2.

Therefore, assuming a prograde coplanar planetary orbit one can use equation 2.1.4 to estimate the mass of the planet to be 2.5 M_{Jupiter} and the semi-major axis to be $a_3 = 1.2 \pm 0.1$ AU, which is approximately $0.45 a_{\text{bin}}$.

Orbital instability of a planet in a binary system occurs when the gravitational perturbative effects of the secondary star cause the semi-major axis and eccentricity to change in such a way that the planet either leaves the gravitational field of the system or collides with another body. The closer the planet is to the primary star the less the planet will be affected by the gravitational field of the secondary and therefore may be able to sustain its dynamical state for a longer duration (Harrington, 1977), which implies the long term stability of planetary orbits within binary systems is entirely possible.

The perturbative effect of the secondary on a planet's orbit depends on the mass-ratio, eccentricity, and semi-major axis of the binary system. Therefore it is possible to estimate the upper limit of the semi-major axis for the planet for which it will be stable. Holman and Wiegert (1999) derived from 3-body simulations of varying mass-ratio, eccentricity, and semi-major axis, an equation which estimates the maximum semi-major axis a planet can have before the secondary's perturbations will cause instability, which is:

$$\begin{aligned}\frac{a_{\mathrm{c}}}{a_{\mathrm{bin}}} = {} & (0.464 \pm 0.006) + (-0.380 \pm 0.010)\mu \\ & + (-0.631 \pm 0.034)e_{\mathrm{bin}} \\ & + (0.586 \pm 0.061)\mu e_{\mathrm{bin}} + (0.150 \pm 0.041)e_{\mathrm{bin}}^2 \\ & + (-0.198 \pm 0.074)\mu e_{\mathrm{bin}}^2,\end{aligned} \tag{2.2.1}$$

where a_{c} is the critical semi-major axis, $\mu = M_2/(M_2+M_1)$, a_{bin} and e_{bin} are the semi-major axis and eccentricity of the binary, and M_1 and M_2 the masses of the primary and secondary, respectively.

In the case of ν Octantis the mass ratio is $\mu \approx 0.30$. Therefore, according to Holman and Wiegert (1999), the maximum semi-major axis for a stable planetary orbit about the primary is $a_{\mathrm{c}} = 0.25a_{\mathrm{bin}}$. It is immediately obvious from this result that the assumed prograde coplanar planet has a semi-major axis almost double this value and therefore should have an unstable orbit, contradicting the observed stability. This result is also in agreement with a comparative study by Cuntz, Eberle and Musielak (2007).

The closest binary to date with a confirmed planet orbiting the primary star is γ Cephei (Hatzes et al. (2003)), which consists of a K0III spectral type primary star with a mass of

$1.467 \pm 0.046\ M_{\odot}$ and a M4 spectral type secondary with a mass of $0.4112 \pm 0.0063\ M_{\odot}$ which orbit at a semi-major axis of 20.18 ± 0.66 AU with a period of 67.5 ± 1.4 yr (Neuhäuser et al. (2007)). The planet has a mass of $1.60 \pm 0.13\ M_{\text{Jupiter}}$ which orbits with a semi-major axis of 2.044 ± 0.057 AU and a period of 902.9 ± 3.5 days. In many ways this system is very similar to the ν Octantis system except for the secondary's much larger separation from the primary. No other planets have ever been detected in such a close binary system and so the ν Octantis planet is observationally unique but does have some theoretical support which is discussed in Section 2.3.

2.3 Retrograde Orbit of the Planetary Companion

The orbit of the planetary companion to the ν Octantis primary star has no support theoretically, both in formation and stability assuming a coplanar prograde[3] orbit. A possible solution to this problem was suggested by Eberle and Cuntz (2010), whereby a retrograde orbits allows for a greater region of orbital stability compared to a prograde orbit.

Eberle and Cuntz (2010) performed simulations via a sixth-order symplectic integration scheme with both prograde and retrograde orbits (see Yoshida, 1990). These simulations were performed with nine different mass ratios reflecting the uncertainties in the mass of the primary and secondary stars. The planetary mass is assumed to be negligible. For each mass configuration a range of semi-major axes between 0.561 - 1.377 AU in thirty equal increments was used. For each configuration of mass and semi-major axis simulations were integrated over 10^3 years for prograde orbits and were assumed to be stable if the planet survived the 10^3 years. In the case of a retrograde orbit simulations were integrated over 10^4 years interval and assumed to be stable if the planet survived the 10^4 years. Furthermore, to probe the stable orbit cut-off point more precisely Eberle and Cuntz (2010) performed further simulations between 1.071 - 1.301 AU in ten equal increments (i.e. higher resolution).

[3] From this point onwards prograde motion is defined as orbital motion in the same direction as the secondary star's motion, while retrograde motion is defined as orbital motion in the opposite direction to the secondary star's motion.

For their prograde orbit simulations they found a stable orbit limit of $0.251a_{\text{bin}}$ which is in agreement with Holman and Wiegert (1999), and as seen in Section 2.2 the region does not include the orbit of the planet. For their retrograde orbit simulations they found a stable orbit limit of $0.479a_{\text{bin}} \pm 0.008a_{\text{bin}}$, for which Eberle and Cuntz (2010) conclude that there is a probability of 60 per cent for a planet to exist in a retrograde orbit which also encapsulates the probability distribution of mass ratios of the stellar components. This result is almost double that of a prograde orbit and is also in line with an earlier work by Jefferys (1974).

The results of Eberle and Cuntz (2010) show that a planet orbiting the ν Octantis primary star can remain in a stable orbit for at least 10^4 years assuming retrograde motion, even with the observational uncertainties. After this result Eberle and Cuntz (2010) performed a 10^7 yr simulation of just the observed planetary case and found that the orbit still remained stable. Figure 2.3.1(b) shows the 10^7 yr retrograde orbital simulation done by Eberle and Cuntz (2010) which clearly shows a much more stable orbit which varies its distance from the primary over a range of 0.6452 - 1.2879 AU, an effect owing to the ellipticity of the stellar and planetary orbits. Figure 2.3.1(a) is an example of an equivalent prograde orbit for which the perturbative effects of the secondary destabilises the planets orbit after only 9.88 years causing it to eventually collide with the primary star.

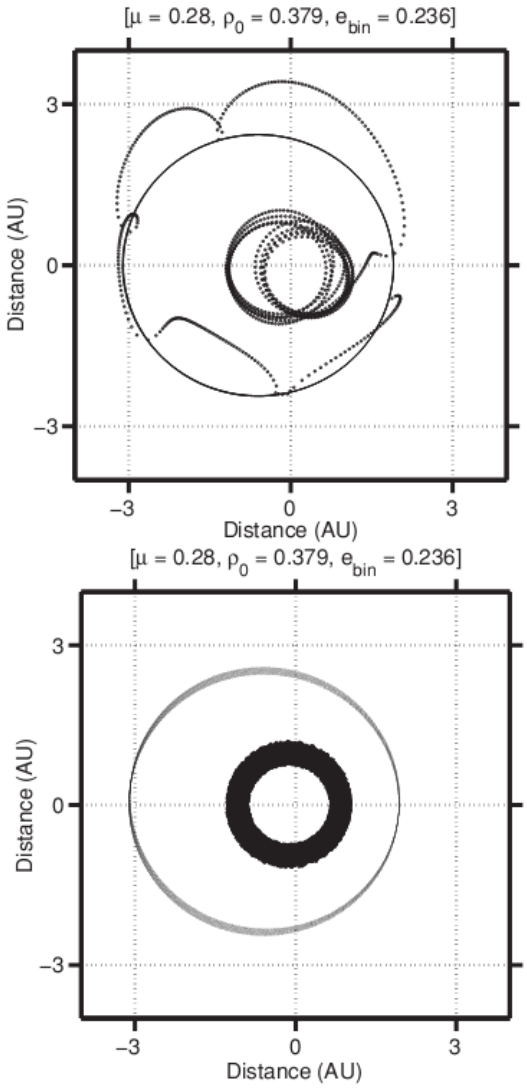

Figure 2.3.1 - *Top:(a) Prograde orbital simulation of the v Oct planet (inner orbit) and the secondary star (outer orbit) about the primary star centred at the origin. Bottom:(b) Retrograde orbital simulation of the same configuration over 10^7 years (Eberle and Cuntz, 2010).*

A recent paper by Quarles et al. (2012) performed simulations in a similar fashion to Eberle and Cuntz (2010) but took into account the observational uncertainties of the orbital elements derived by Ramm et al. (2009) and they used a more quantitative means of measuring the stability, that is, they derived the maximum Lyapunov exponent (MLE) which measures the rate at which nearby trajectories diverge (Lyapunov, 1907). If the MLE becomes greater than -0.82 as determined in Quarles et al. (2011) then the orbit is classed as unstable. They also experimented with two different planetary starting potions, the 3

o'clock and 9 o'clock positions, which are defined by a mean anomaly of 0° and 180° respectively.

The results from Quarles et al. (2012) for prograde orbits integrated over 10^4 binary orbits showed a 9.2 per cent probability that the planet would be in a stable orbit when initiated from the 3 o'clock position and a 0.6 per cent probability if initiated from the 9 o'clock position. For a retrograde orbit integrated over 10^5 binary orbits they found a probability of 94.9 per cent that the planet would be in a stable orbit if initiated from the 3 o'clock position and a 100 per cent probability if initiated from the 9 o'clock position.

According to the papers discussed above it can be concluded that if a planet does exist in the ν Octantis system orbiting the primary star as described by Ramm et al. (2009) then a prograde orbit will not allow a stable orbit as previously thought, based on Holman and Wiegert (1999). However, it is almost certain to have a retrograde orbit if it is to be consistent with the observed stability.

2.4 Precession due to a Close Binary System

Another solution to the unstable planetary orbit is that the perturbation is not a planet at all, but is due to the secondary star itself being a close binary, suggested by Morais and Correia (2012). The RV perturbation seen in the observations is thought to be the result of both the inner binary's wobble about its own centre of mass and the inner binary's orbit precessing. Morais and Correia (2012) derived an equation from the secular Hamiltonian to approximate the precession rate ($\dot{\omega}_2$) of the inner binary to be:

$$\dot{\omega}_2 = \frac{12C}{G_2}A, \tag{2.3.1}$$

$$A = \left(\frac{1}{2} + \frac{3}{4}e_1^2\right)(3\theta^2 - 1) + 15e_1^2(1-\theta^2)\cos(2\omega_1),$$

$$C = \frac{G}{16}\frac{M_0 M_1}{M_0 + M_1}\frac{M_2}{(1-e_2^2)^{2/3}}\frac{a_1^2}{a_2^3},$$

$$G_2 = \frac{M_2(M_0 + M_1)}{M_0 + M_1 + M_2}\sqrt{\mu_2 a_2(1 - e_2^2)},$$

where M_0, M_1, and M_2 are the masses of the primary star and inner binary, respectively, a_2, e_2, a_1, and e_1 are the semi-major axis and eccentricity of the main binary and inner binary, respectively, and $\mu_2 = G(M_0+M_1+M_2)$.

The radial velocity of a star with a close binary system can be expressed as:

$$V_r = K_0(\cos(\theta_0 + \Omega t)) + K(\cos(f_2 + \omega_2) + e_2 \cos\omega_2), \qquad (2.3.2)$$

$$K = \frac{2\pi}{P}\frac{a_2 \sin i_2}{\sqrt{1 - e_2^2}}\frac{M_0 + M_1}{M_0 + M_1 + M_2},$$

where K_0 is the semi-amplitude of the outer binary, and ω_2 changes linearly with time, so $\omega_2 = \omega_{20} + \dot{\omega}_2 t$ (Morais and Correia, 2012). The radial velocity of the stars orbit can be inferred from the RV curve and is mostly due to the term $e_2 \cos\omega_2$, which represents the wobble of the inner binary about its own centre of mass. Typically the observational time t_{obs} is much shorter than a precession cycle, thus if $\omega_{20} \neq 0°, 180°$:

$$Ke_2 \cos\omega_2 \approx Ke_2[\cos(\omega_{20}) - \sin(\omega_{20})\ \dot{\omega}_2\ t]. \qquad (2.3.3)$$

Thus equation 2.3.3 is approximately keplerian whose amplitude has a linear drift of at most $(\omega_{20} = 90°, 270°)\ Ke_2\dot{\omega}_2\ t_{\text{obs}}$.

Morais and Correia (2012) have fitted their precessing keplerian orbit to the data given in Ramm et al. (2009) with a precession rate of -0.86 °/yr. After subtracting this orbit from the data they obtained an RMS of 36.3 ms^{-1} which is only slightly better than Ramm et al. (2009) who got 39.1 ms^{-1} for their single keplerian orbit. However, this scatter is still much larger than the fit for a double keplerian assuming the perturbation is caused by a planet, which gave an RMS of 19 ms^{-1}. Morais and Correia (2012) comment that this could be due to the short-observation time span, or even due to this particular sampling of RV data.

One of the main reasons that Morais and Correia (2012) believe that ν Octantis may be a triple star system is that in their analysis of retrograde precession for which the binary has an inclination greater than 45° with respect to the main binary's orbit, they found that it can

produce peaks in a periodogram which can be mistaken for a planetary perturbation. In particular these peaks appear near period harmonics such as the 5:2 period ratio that is exhibited in the observed perturbation and is strong evidence that the secondary is another close binary. If this is the case then the precessing close binary will cause an additional perturbation with a period close to the original perturbation which must agree with the relations $\frac{2\pi}{P_2} - \frac{2\pi}{P_1} = 2\Omega$, and $K_1 = 5|K_2|$ (Morais and Correia, 2008), where Ω is the longitude of ascending node. Therefore, perturbations with very low amplitudes such as ν Octantis's 51.8 ms^{-1}amplitude would have a very small secondary perturbation (i.e. 10 ms^{-1} for ν Octantis) which can be below the precision of the spectrograph, and thus would be very hard to detect.

Assuming precession due to a close binary is the case for ν Octantis, Morais and Correia (2012) estimated the masses of the inner binary to be $M_1 = 0.23\ M_\odot$ and $M_2 = 0.27\ M_\odot$ with a semi-major axis, eccentricity, and inclination of 0.35 AU, 0.76, and 60° respectively.

Chapter 3
Modelling the Orbit of the ν Octantis Planet

3.1 Modelling the Orbit

According to Holman and Wiegert (1999) who performed many simulations over many different orbital configurations and derived the general equation (2.2.1) for the outer stable orbit limit of prograde orbits, the ν Octantis primary star has a stable orbit limit of 0.6375 AU, assuming coplanar prograde motion. Therefore, the observed ν Octantis planet which has a semi-major axis of 1.2 AU should be in an unstable orbit, contradicting the observed stability. Eberle and Cuntz (2010) showed in their simulations that a retrograde orbit allows for a stable planetary orbit, but do not explain why. Mean-motion resonance and/or an enlarged region of stability are two possible explanations for the observed stability.

Orbital resonance occurs when two orbiting bodies exert regular periodic gravitational perturbations on one another. This can result in either an unstable orbit whereby the two bodies exchange momentum until the resonance no longer exist, or, under some circumstances a resonant orbit can be very stable and self-correcting, allowing orbits to exist where they would normally be unstable. This is the case with mean-motion resonance (Malhotra, et al., 1998). Mean-motion resonance is where the periods of two bodies are close to a ratio of small integers, for example, Pluto has an orbit which crosses the path of Neptune but because the two bodies are in a 2:3 period resonance (i.e. Pluto completes two orbits in the time it takes for Neptune to complete three orbits) they never pass within 18 AU of one another, thus avoiding collision (Cohen and Hubbard, 1965). Extra-solar multi-planet systems have also been discovered with mean-motion resonances, for example, HD 82943 (Israelian et al., 2001) and GJ 876 (Marcy et al., 2001; Rivera and Lissauer, 2001), which are systems in a 2:1 resonance.

In the case of ν Octantis there appears to be a near mean-motion resonance of 5:2 between the secondary and the suggested planet. If resonance is the cause of the stable retrograde orbit then it is highly probable that other resonances can be achieved. The possible resonances in the ν Octantis system include 3:1, 5:2, 2:1, 7:4, and 3:2 for which the details are given in Table 3.1.

Period Ratio	**Planet Period (d)**	**Semi-major axis (AU)**
3:1	350.04	1.0874
5:2	420.04	1.2279
2:1	525.05	1.4249
7:4	600.06	1.5576
3:2	700.07	1.7261

Table 3.1 - *Mean - motion resonances for the ν Octantis system.*

Another possible cause for the stability of the retrograde orbit in the ν Octantis system is that the retrograde motion simply increases the region of stability about the primary star. One possible explanation suggested by Jefferys (1974) is that in a general rotating frame of reference with respect to the central body both prograde and retrograde orbits have identi-

cal velocities but of opposite sign. However, in a fixed coordinate frame the prograde orbit has a larger velocity and therefore more kinetic energy resulting in a less tightly bound orbit. Thus the retrograde orbits are stable at a larger distance from the central body.

In order to understand the cause of the stable retrograde orbit in the ν Octantis system one needs to know more about how the planet orbits in such a close binary system. Since we cannot observe the system directly this can be achieved by performing 3-body simulations of the system via the N-body integrator Mercury6, written by Chambers (1999). Mercury6 takes Hamilton's equations of motion which give the rate of change of position (x) and momentum (p) for each body in the N-body system:

$$\frac{dx_i}{dt} = \frac{\delta H}{\delta p_i}, \qquad \frac{dp_i}{dt} = -\frac{\delta H}{\delta x_i}. \tag{3.1.1}$$

The Hamiltonian H, is the sum of the kinetic and potential energy in terms of all bodies:

$$H = \sum_{i=1}^{N} \frac{p_i^2}{2m_i} - G \sum_{i=1}^{N} m_i \sum_{j=i+1}^{N} \frac{m_j}{r_{ij}}, \tag{3.1.2}$$

where m_i is the mass of body i, and r_{ij} is the separation between bodies i and j. Therefore, by equation 3.1.1 the rate of change of any quantity q is:

$$\begin{aligned} \frac{dq}{dt} &= \sum_{i=1}^{n} \left(\frac{\delta q}{\delta x_i} \frac{dx_i}{dt} + \frac{\delta q}{\delta p_i} \frac{dp_i}{dt} \right) \\ &= \sum_{i=1}^{n} \left(\frac{\delta q}{\delta x_i} \frac{\delta H}{\delta p_i} + \frac{\delta q}{\delta p_i} \frac{\delta H}{\delta x_i} \right) = Fq\,, \end{aligned} \tag{3.1.3}$$

where F is an operator. The variable q can represent either position or momentum or any combination of the two. The general solution to equation 3.1.3 is:

$$\begin{aligned} q(t) &= e^{tF} q(t-\tau) \\ &= \left(1 + \tau F + \frac{\tau^2 F^2}{2} + \ \ldots \right) q(t-\tau), \end{aligned} \tag{3.1.4}$$

where $q(t-\tau)$ is the value of q at some earlier epoch. In order to solve this ordinary differential equation (ODE) numerically over time and thus determine the time evolution of an orbit, Mercury6 employs the use of a very accurate Bulirsch-Stoer algorithm (Bulirsch and Stoer, 1965).

The Bulirsch-Stoer algorithm involves three key ideas; Richardson extrapolation, rational functions, and the modified midpoint method (Bulirsch and Stoer, 1965). One implementation of the Bulirsch-Stoer algorithm evaluates an ODE over the time interval t to $t + \delta t$, where δt is a large, not at all infinitesimal, time interval and determines numerically the change in the function with time to a high accuracy.

Suppose we have a body orbiting a central mass, at some initial time t_0 the body is at position (x_0, y_0, z_0) and has a time dependent function $g(t)$, with velocity $\mathrm{d}g/\mathrm{d}t = \mathrm{f}(t,g(t))$. We then want to calculate the position at some later time $t_0 + \delta t$ via the modified midpoint method. The modified midpoint method takes the step $t_0 + \delta t$ and divides it into n smaller even numbered sub-steps (i.e. n = 2, 4, 6, 8, ...), where the sizes of the sub-steps are $h = \delta t/n$. We then evaluate the ODE at each step via the following formulae (Press et al., 2007):

$$\begin{aligned} G_0 &= g(t_0), \\ G_1 &= G_0 + h\, f\big(t_0, g(t)\big), \\ G_{m+1} &= G_{m-1} + 2h\, f(t_0 + mh, G_m), \qquad m = 1, 2, \dots, n-1. \end{aligned} \tag{3.1.5}$$

The value of the function $g(t_0 + \delta t)$ can then be expressed as:

$$g(t_0 + \delta t) \approx g_n = \frac{1}{2}\big(G_n + G_{n-1} + hf(t_0 + \delta t, G_n)\big). \tag{3.1.6}$$

The modified midpoint method can itself be used as an ODE integrator, but can be made more accurate via Richardson extrapolation.

Richardson extrapolation (Richardson, 1911) is the process of fitting an analytical form to a data set and then evaluating it with a zero step size (h = 0). In the Bulirsch-Stoer algorithm the modified midpoint method provides the data set of n data points between the time interval t_0 to $t_0 + \delta t$, then Richardson extrapolation is used to fit a rational function to the

data points which in turn gives the value and error estimated for the point $g(t_0 + \delta t)$. If the error is not satisfactory the entire process is repeated with a larger number of sub-steps in the modified midpoint method. In the case of ν Octantis the accuracy is on the order of 10^{-12} in terms of conservation of energy and momentum.

Another similar general ODE integrator algorithm is the Runge-Kutta algorithm (Runge, 1895). This algorithm uses the midpoint method and is similar to the modified midpoint method as the name suggests. The midpoint method basically evaluates the ODE at the point half way between t_0 and $t_0 + \delta t$ via the formulae (Press et al., 2007):

$$\begin{aligned} k_1 &= hf(t_n, g_n); \\ k_2 &= hf\left(t_n + \frac{1}{2}h\,, g_n + \frac{1}{2}k_1\right); \\ g_{n+1} &= g_n + k_2 + O(h^2). \end{aligned} \tag{3.1.7}$$

The Runge-Kutta algorithm takes this to the next level by dividing the sub-step further and performs the midpoint method either side of the main steps midpoint. The fourth-order form of this algorithm can be expressed as (Press et al., 2007):

$$\begin{aligned} k_1 &= hf(t_n, g_n); \\ k_2 &= hf\left(t_n + \frac{1}{2}h\,, g_n + \frac{1}{2}k_1\right); \\ k_3 &= hf\left(t_n + \frac{1}{2}h\,, g_n + \frac{1}{2}k_2\right); \\ k_4 &= hf\left(t_n + \frac{1}{2}h\,, g_n + \frac{1}{2}k_3\right). \end{aligned} \tag{3.1.8}$$

Thus the value $g(t_0 + \delta t)$ can be expressed as:

$$g_{n+1} = g_n + \frac{1}{6}k_1 + \frac{1}{3}k_2 + \frac{1}{3}k_3 + \frac{1}{6}k_4 + O(h^5) \tag{3.1.9}$$

When compared to the Bulirsch-Stoer algorithm the Runge-Kutta algorithm can obtain a similar accuracy but requires four derivative evaluations per step h, whereas the Bulirsch-Stoer algorithm requires only one and a half derivative evaluations per step h, thus requires less computational time. However, in other applications which involve non-smooth ODE

integrations the Bulirsch-Stoer algorithm fails to work where the Runge-Kutta algorithm succeeds (Press et al., 2007). This is not the case for the ν Octantis system and so the Bulirsch-Stoer algorithm was used.

Symplectic integrators are an attempt to decrease the computational time for an N-body problem. This is done by splitting the exponential equations of motion (equation 3.1.4) into two parts, one which calculates the normal two body keplerian motion ignoring the other bodies, and the other calculates just the gravitational perturbations due to the presence of other bodies (Wisdom and Holman, 1991). Each part can be integrated over different time intervals (i.e. normal keplerian motion can be integrated over say ten-day intervals while the perturbations are integrated over one-day intervals). This prioritising allows a much faster computational time since less time is spent on lower priority computations. Higher order integrators can be devised by splitting each of the exponential terms still further (Yoshida, 1990).

Examples of symplectic integrators include HNbody by Rauch and Hamilton (2002) and the mixed-variable symplectic algorithm by Wisdom et al. (1996). The disadvantage of symplectic integrators is that with each close encounter between each body the time step must be altered and therefore energy errors are introduced which are cumulative, thus over a long period of time the accuracy becomes very low. Mercury6 has attempted to overcome this problem with their hybrid symplectic/Bulirsch-Stoer algorithm by changing over to a Bulirsch-Stoer algorithm during close encounters (Chambers, 1999). However, the hybrid version was not used for the ν Octantis simulations because the accuracy over long time intervals was not satisfactory for such a close binary system.

To investigate the orbit of the ν Octantis planet, Mercury6 was first used to confirm the unstable and stable orbits of the prograde and retrograde orbits respectively by performing 10^3-yr simulations with the orbital elements in Table 3.2. Both simulations have a time step of one day, and were initiated from the 9 o'clock position (or mean anomaly of 180°) with the semi-major axes aligned, as shown in Figure 3.1.1. Investigations of the long term behaviour of the retrograde orbit was carried out by performing a 10^8 yr simulation with the same orbital elements in Table 3.2, but with a time step of ten days, needed because of the time consuming computations. It should also be noted that this simulation was done on the BlueFern super computer at the University of Canterbury.

Table 3.2 - Orbital Elements	
$M_1(M_{\text{sun}})$	1.4 ± 0.3
$M_2(M_{\text{sun}})$	0.5 ± 0.1
$M_{\text{pl}}(M_{\text{J}})$	2.5
P_{bin} (d)	1050.11 ± 0.13
P_{p} (d)	417.4 ± 3.8
e_{bin}	0.2358 ± 0.0003
e_{p}	0.123 ± 0.037

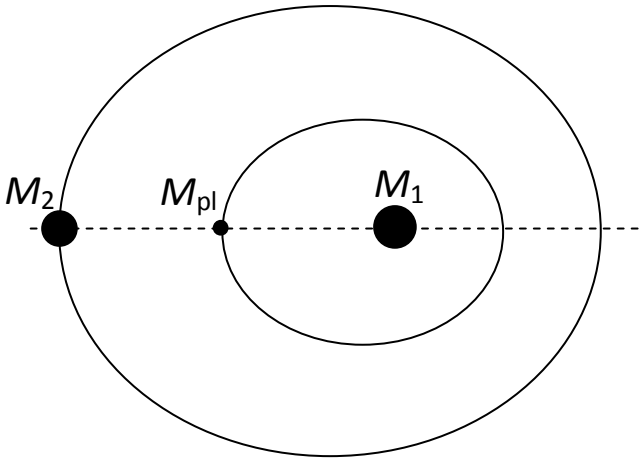

Figure 3.1.1 - *Configuration of initial conditions of orbital simulations for the primary star (M_1), secondary star (M_2), and the suggested planet (M_{pl}).*

In order to investigate the two hypotheses stated previously, namely mean-motion resonance and a greater region of stability, a systematic procedure was devised whereby a test mass of 2.5 M_{J} was used in simulations over a range of eccentricities. Three eccentricities values were chosen consisting of the observed planetary eccentricity and the corresponding upper and lower limits of the uncertainty, which are e_{pl} = 0.086, e_{pl} = 0.123, and e_{pl} = 0.160 (Ramm et al., 2009). For each of these eccentricities a set of nine mass combinations or mass ratios (M_2/M_1) pertaining to the masses of the primary and secondary star were chosen also by within the upper and lower limits of the uncertainty. The chosen masses consist of 1.1, 1.4, and 1.7 solar masses for the primary and 0.4, 0.5, and 0.6 solar masses

for the secondary. For each mass ratio a range of initial semi-major axes between 1.010 and 1.798 AU was chosen with a resolution of 0.004 AU. Note that the uncertainty in the mass of the planet, period of the secondary, and its eccentricity, were neglected since changing these parameters within their respective uncertainties does not dramatically affect the planet's orbit. All the above simulations were performed over a 10^4-yr period with a time-step of five days. The information gathered from these simulations will allow the calculation of the probability for an orbit to exist with a planet pertaining to the observed perturbation at specified initial semi-major axes, and in turn the characteristics of the ν Octantis system.

In order to investigate the relationship between the eccentricity period and the semi-major axis in both prograde and retrograde orbits a systematic procedure was devised. Mercury6 simulations were performed over a range of semi-major axes between 0.1 AU to 0.6 AU for the prograde orbits and 0.1 AU to 1.2 AU for the retrograde orbits. These simulations were done using the values Ramm et al. (2009) obtained for the masses and eccentricities of the primary star, secondary star, and planet shown in Table 3.2, which were integrated over a 10^4-yr time interval with a time step of one day.

To investigate if non-coplanar retrograde orbits contain stable orbits a systematic procedure was devised where a test mass of 2.5 M_J was used in simulations over a range of inclinations between 135° to 225° about the 180° coplanar orbit at a resolution of 5°. This was done using the masses, eccentricities, and semi-major axis of the primary star, secondary star, and the planet as determined in Ramm et al. also shown in Table 3.2. The simulations were first integrated for a 10^4-yr time interval with a time step of 5 days. The orbits which survived the 10^4-yr were then integrated over a 10^5-yr time interval with the same time step. Orbits which survived the 10^5-yr period were assumed to be stable, however, this does not mean they will remain stable over longer periods of time.

3.2 Simulation Results and Discussion

3.2.1 Confirmation of Retrograde Orbital Stability

In order to confirm the unstable and stable orbits of the prograde and retrograde orbits respectively, Mercury6 was used to perform simulations for both cases. Figure 3.2.1(a) shows the orbital path for the planet undergoing prograde motion along with the orbital path of the secondary star, also assumed to be in a prograde orbit. Figures 3.2.1(b), and (c) show the time evolution of the eccentricity and of the semi-major axis respectively for both the planet and secondary star in the prograde orbit. It can be seen that, owing to the gravitational perturbations of the secondary, the planet's orbit becomes more and more erratic over time with both the eccentricity and semi-major axis largely increasing for 12 years, at which point the planet is ejected from the system entirely.

In the case of a retrograde orbit seen in Figure 3.2.1 (d) the planet's motion over the same time interval is very stable and lasts for at least 20×10^3 yr. The semi-major axis (Figure 3.2.1 (e)) varies periodically by a maximum of 0.1 AU and the eccentricity (Figure 3.2.1 (f)) varies periodically by about 0.1 over the 2.9 yr period of the secondary, but it also seems to have a downward trend, suggesting another longer periodic effect due to the secondary. In fact a plot of eccentricity over 100 yr shows another period of about 40 yr, shown in Figure 3.2.2. From these results it can be concluded that the retrograde motion allows for a stable orbit whereas prograde motion cannot.

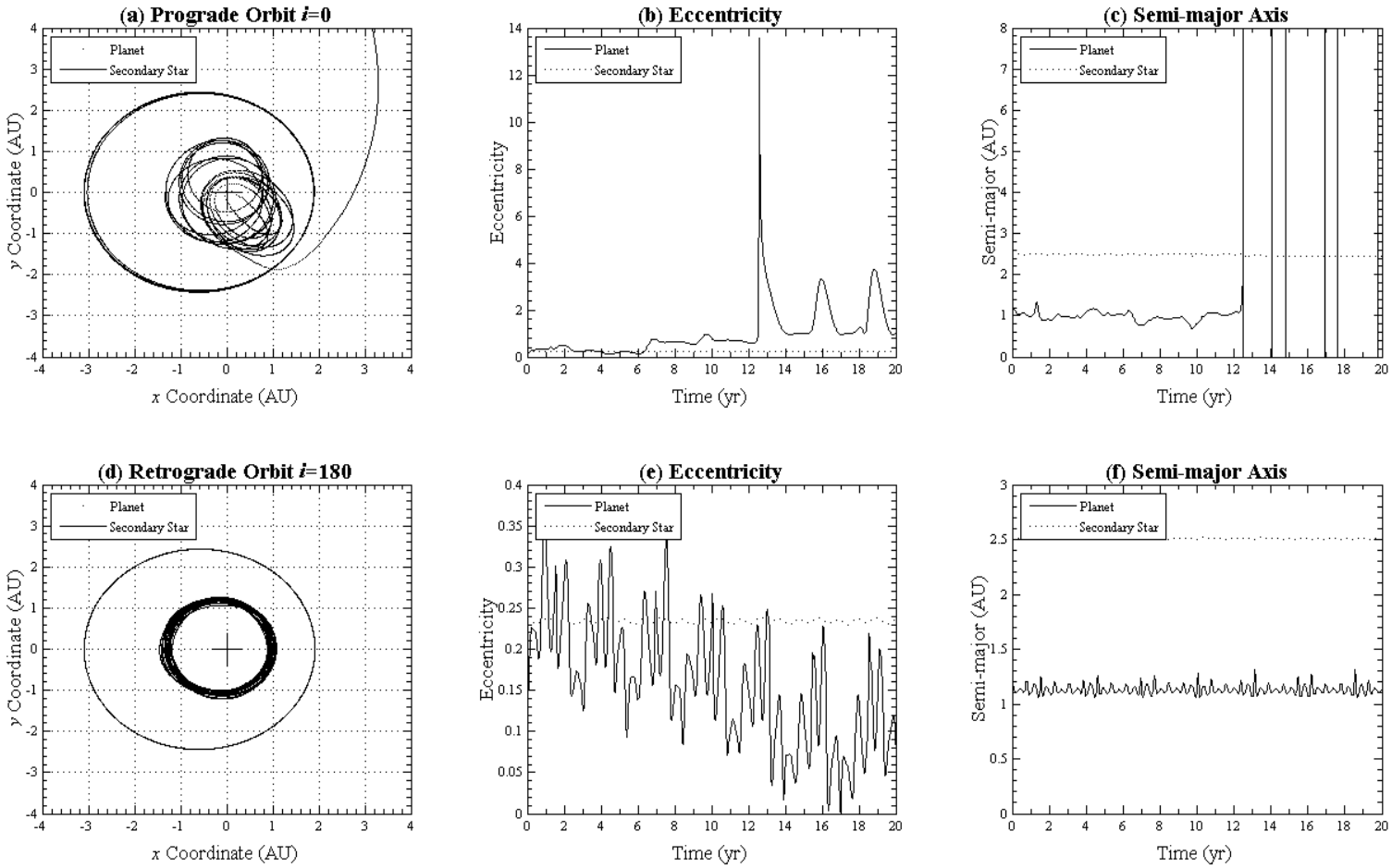

Figure 3.2.1 - *(a) Simulation of a 417.4-day planetary coplanar prograde orbit (dots) in the v Oct system together with the resulting secondary motion (dashed-line) about the primary, situated at the origin. (b),(c) The change in semi-major axis and eccentricity respectively over 20 yr of the prograde orbit. (d) Retrograde orbit (inner region) of the same situation and the resulting secondary motion (outer region) about the primary at the origin. (e),(f) Corresponding semi-major axis and eccentricity respectively of the retrograde orbit over same 20-yr interval.*

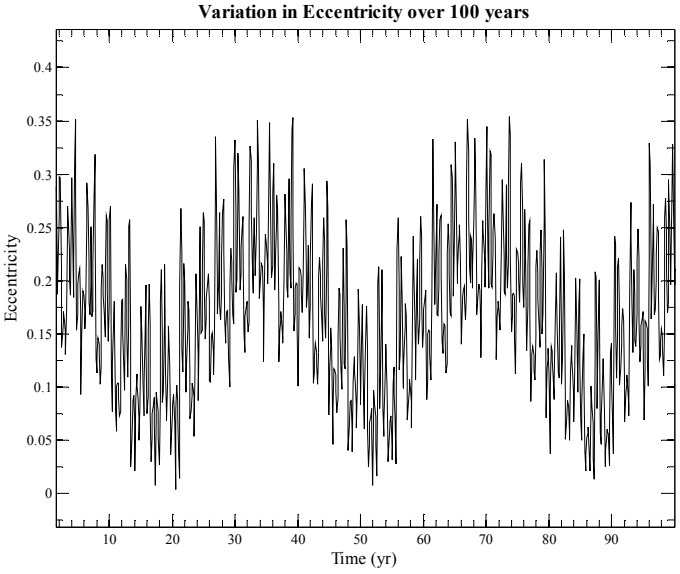

Figure 3.2.2 - *The periodic variation in planet's eccentricity in a retrograde orbit over 100 yr.*

3.2.2 100-Million year Retrograde Orbit Simulation

To investigate the long term stability of the ν Octantis planet in a retrograde orbit a 100 million-year simulation was performed with Mercury6 using the University of Canterbury's BlueFern super-computer. Figure 3.2.3 shows the results of this simulation plotting a data point every 100 years. Note that not all points at a time step of 10 days were plotted, because the total raw file size of the simulation was approximately 80 GB which cannot be handled by Matlab.

It can be seen in Figure 3.2.3(a) that the planetary retrograde orbit over the 10^8 years, corresponding to 3.5×10^7 binary orbits, stays within a ring slightly offset from the origin. This is an unequivocal indication of long-term stability for the planet undergoing retrograde motion. To further strengthen the support for orbital stability the distances between the primary and secondary as well as the primary and planet were assessed over the 10^8 yr time period. The semi-major axis in Figure 3.2.3(c) has a mean value of 1.131 AU and varies with a standard deviation of 0.039 AU. The distance between the primary star and planet varies between 0.869 and 1.462 AU over the 10^8 yr period, while the distance be-

tween the two stars varies between 1.915 and 3.095 AU. In the case of the secondary these results compare very well to the apoapsis and periapsis of the binary component, and so the binary essentially undergoes two-body keplerian motion. In the case of the planet the apoapsis and periapsis are 1.07 and 1.37 ± 0.1 AU which also agree with the maximum and minimum distances between the planet and primary to within the uncertainties of observation. Therefore it can be assumed that these variations in distance are due to the elliptical orbits of the planet and secondary and not due to some long-term changes in the system. These results also agree with those of Eberle and Cuntz (2010).

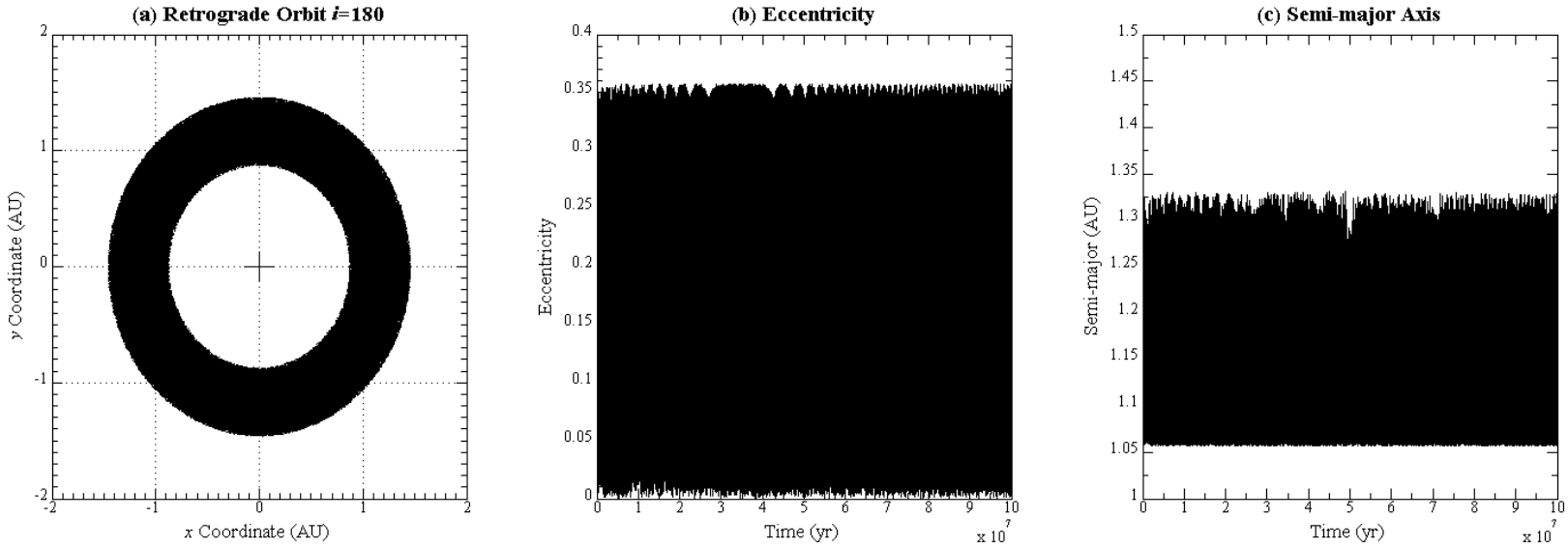

Figure 3.2.3 - *(a) Simulation of a 417.4-day planetary retrograde orbit (dots) in the v Oct system over* 10^8**-** *years about the primary, situated at the origin. (b),(c) The change in semi-major axis and eccentricity respectively over* 10^8**-***yr of the retrograde orbit.*

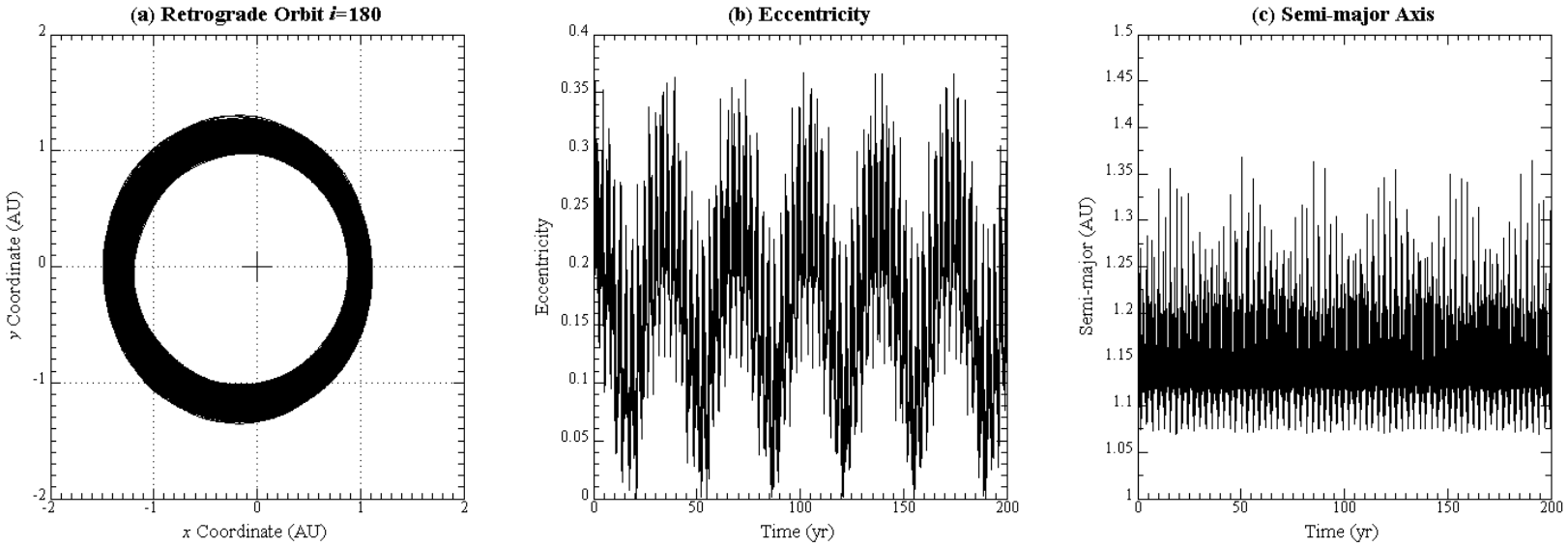

Figure 3.2.4 - *(a) Simulation of a 417.4-day planetary retrograde orbit (dots) in the v Oct system over 200 years about the primary, situated at the origin. (b),(c) The change in semi-major axis and eccentricity respectively over 200 years of the retrograde orbit.*

Figure 3.2.3(b) shows the variation in the eccentricity over the 10^8 yr which has a mean value of 0.1663 and a standard deviation of 0.071. The eccentricity also varies between a maximum of 0.35 and a minimum of 0 which also varies periodically with a period of about 40 years consistently.

3.2.3 Stability of Other Orbits in the ν Octantis System

Figure 3.2.5, Figure 3.2.6, and Figure 3.2.7 are plots showing the survival time for a test mass of 2.5 M_J over a range of period ratios (P_{bin}/P_{pl}), mass ratios, and eccentricities which were acquired by performing 10^4-yr simulations, as described in Section 3.1. The survival time represents the amount of time for which the test mass lasted in the system before it either collides with one of the stellar components or is ejected from the system entirely. It is assumed that if the orbit survived the 10^4-yr simulation then the orbit is stable; however, this does not mean the orbit will not become unstable over a longer time interval.

In general all orbital configurations in Figure 3.2.5, Figure 3.2.6, and Figure 3.2.7 behave in a similar manner, in that, there is an 'inner region' of stable orbits and an 'outer region' consisting of mostly unstable orbits, for example, Figure 3.2.5 with masses (0.4, 1.1) $M_\odot$ has an inner region with period ratios greater than 2.4 and the outer region has period ratios less than 2.4. The inner region appears to have a cut-off point after which most orbits become unstable or there is a kind of boundary between the inner and outer regions. We will call this the stable orbit limit (SOL). The SOL appears to depend largely on the mass of the primary star, for example, in Figure 3.2.6 where the eccentricity is 0.123, the mass ratios 0.4/1.1, 0.4/1.4, and 0.4/1.7 have SOLs of $P_{bin}/P_{pl} = 2.55$, $P_{bin}/P_{pl} = 2.27$, and $P_{bin}/P_{pl} = 1.98$ respectively. Thus the more massive the primary the larger the SOL. However, the mass of the secondary and the eccentricity of the planet appear only to have a small effect on the SOL. This can be explained by a simple comparison of forces, in that, an increase in the central mass results in a deeper gravitational potential well and therefore the orbit is

more tightly bound. Thus the planet is less susceptible to the gravitational perturbations of the secondary star.

The outer regions of all the orbital configurations in Figure 3.2.5, Figure 3.2.6, and Figure 3.2.7 seem to depend largely on the mass of the secondary and the eccentricity of the planet. For example, in Figure 3.2.5 the mass ratio 0.4/1.7 consists of many stable orbits in the outer region and can almost be considered to be stable at all period ratios. However, a larger secondary mass of 0.5 $M_{\odot}$ reduces the number of stable orbits severely and again this occurs also for a mass of 0.6 $M_{\odot}$. For the same mass ratios but with e = 0.123, the mass ratios of 0.4/1.7 only consists of a few stable orbits and no orbits for larger mass ratios. For e = 0.160 no stable orbits exist in the outer region.

The mean SOL for the suggested ν Octantis planet can be calculated from the average SOL over all orbital configurations in Figure 3.2.5, Figure 3.2.6, and Figure 3.2.7. This was calculated to be a = 1.315 ± 0.092 AU, where the uncertainty is the standard deviation over all simulations. This SOL is a little larger than what Eberle and Cuntz (2010) obtained (a =1.221 ± 0.008 AU) but does agree to within the error bars. Clearly the SOL for a retrograde orbit is about twice as large as a prograde orbit agreeing with earlier work by Jefferys (1974), who stated that prograde orbits have more kinetic energy than an equivalent retrograde orbit and therefore prograde motion give rise to less tightly bound orbits.

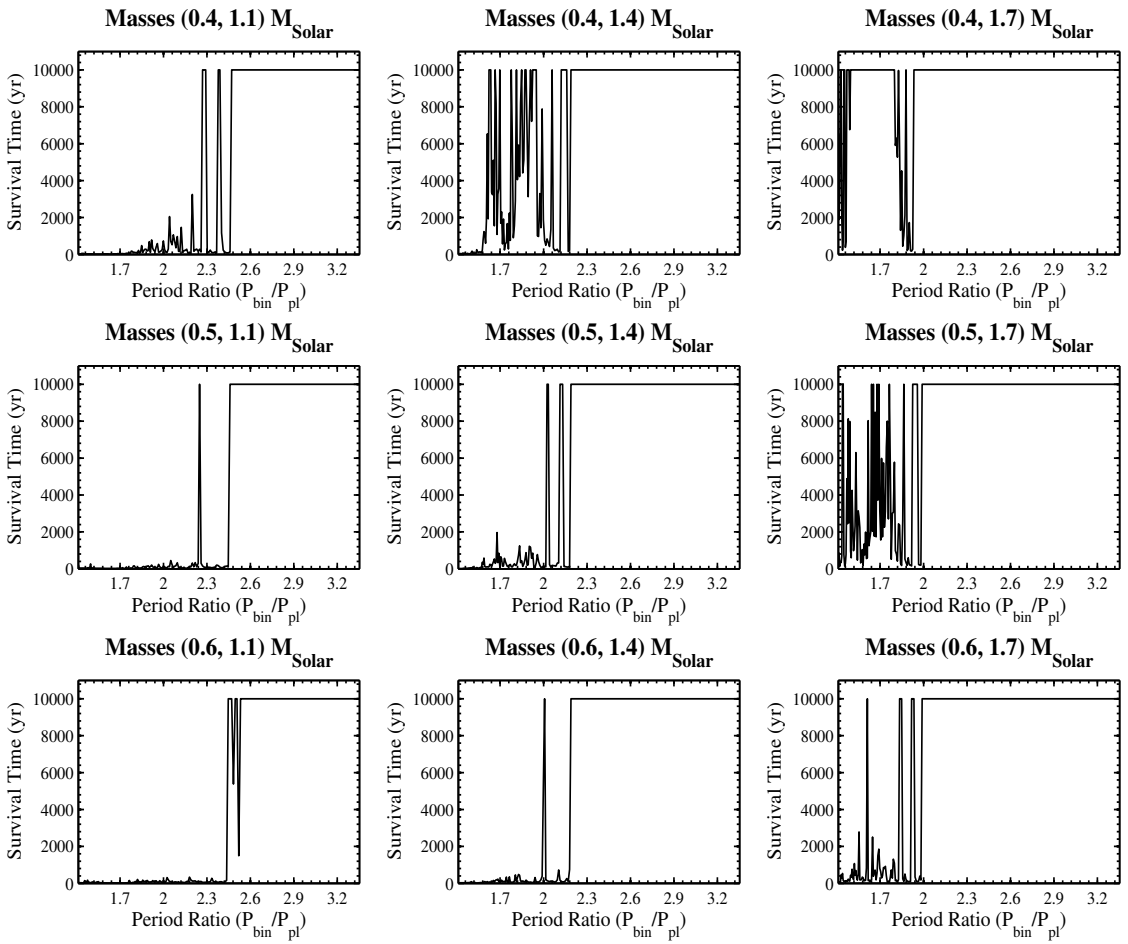

Figure 3.2.5 - *Orbital Survival times for a 2.5 M_J test planet with eccentricity 0.086 over a range of period ratios and mass combinations of the primary and secondary star within, the uncertainties of the observations.*

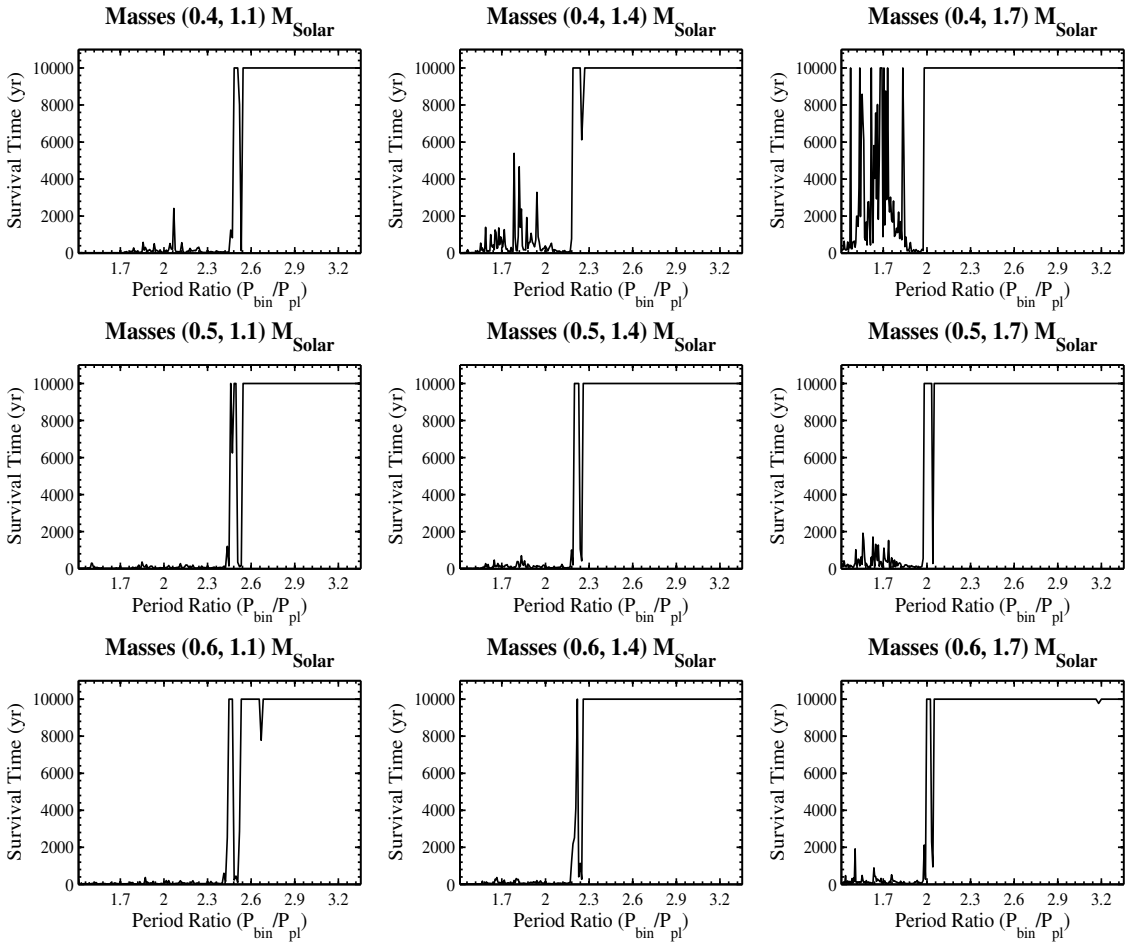

Figure 3.2.6 - *Orbital Survival times for a 2.5 M_J test planet with eccentricity 0.123 over a range of period ratios and mass combinations of the primary and secondary star, within the uncertainties of the observations.*

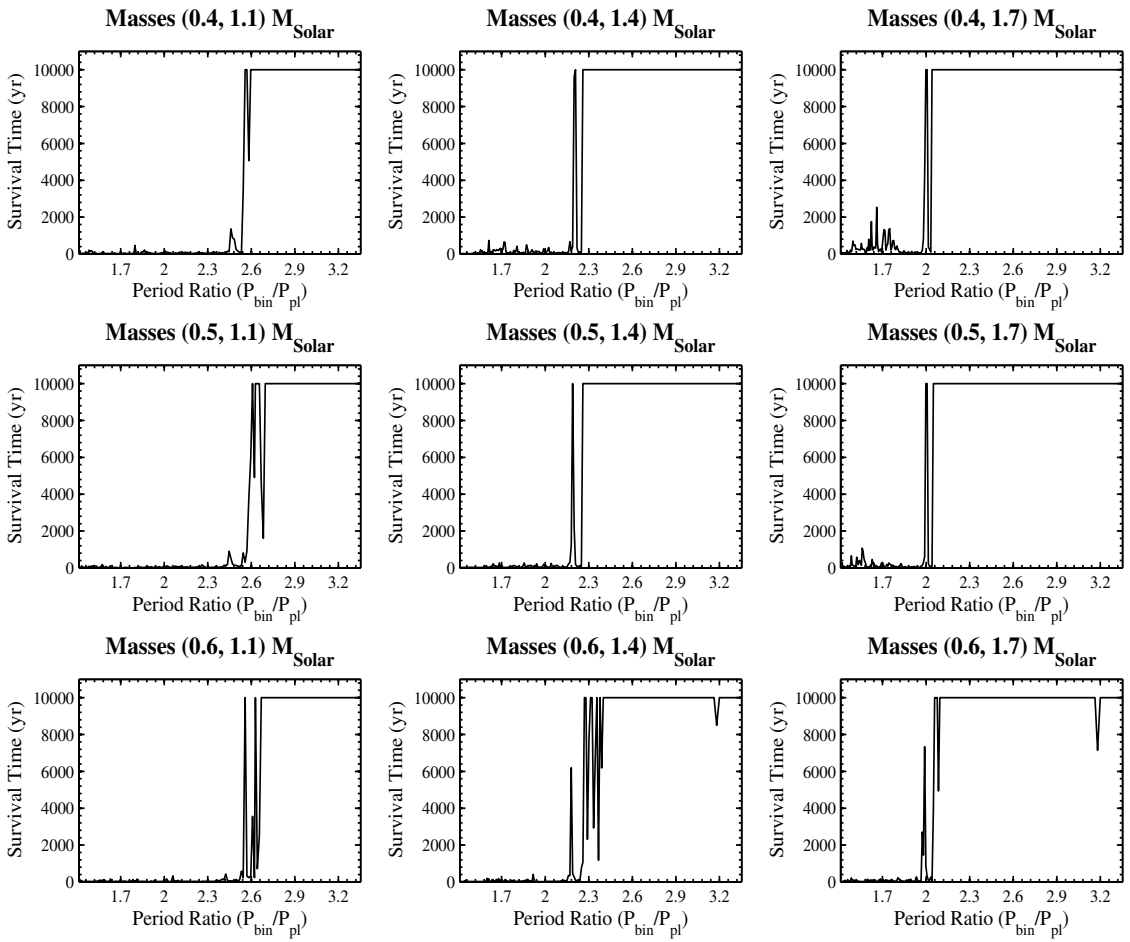

Figure 3.2.7 - *Orbital Survival times for a 2.5 M_J test planet with eccentricity 0.160 over a range of period ratios and mass combinations of the primary and secondary star, within the uncertainties of the observations.*

In order to investigate mean-motion resonance at different period ratios of the suggested planet one can calculate the fraction of stable orbits from Figure 3.2.5, Figure 3.2.6, and Figure 3.2.7 by assigning a 1 to orbits which survive the 10^4-yr interval and a zero to those that do not. Then by taking the mean of all the orbital configurations we can produce a plot representing the fraction of stable orbits which takes into account the major observational uncertainties, Figure 3.2.8 is a plot of this fraction of stable orbits. Note that 'probability' used in this chapter refers to the fraction of simulated orbits that survive the 10^4-yr interval

According to Figure 3.2.8, the observed perturbation which has a period ratio of 2.51, which is close to the 5:2 mean-motion resonance, has an 80 per cent probability of surviving the 10^4-yr time interval taking into account the error bars of the planetary period. The 3:2 mean motion resonance has a 100 per cent probability of surviving 10^4 years. However, this could be because it is within the stable orbit region. It should also be noted that at a higher period ratio of 3.18 the probability drops to 90 per cent for a single orbit, which suggest that orbits around this point may become unstable over longer time intervals. The 2:1 mean-motion resonance has a low survival probability of 30 per cent, as well as the 7:4 and 3:2 mean-motion resonances with probabilities of less than 10 per cent. Evidently, the absence of other mean-motion resonances strongly supports the conclusion that resonance is not the key to the stability of the retrograde orbit, otherwise these orbits could exist. It would appear that the more likely case is that retrograde orbits are inherently much more stable than prograde orbits, whether there is a mean-motion resonance or not.

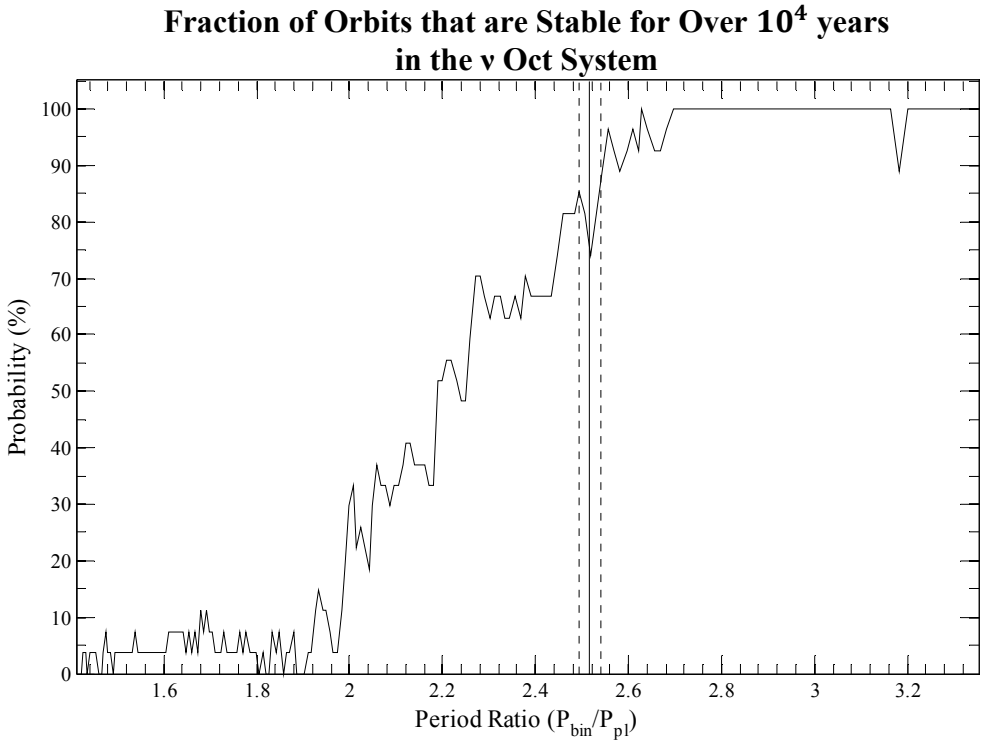

Figure 3.2.8 - *Fraction of orbits survived for a 2.5 M_J test planet over* $\mathbf{10^4}$ *years corresponding to the mean orbital elements of the ν Oct system within the observational uncertainties. Vertical solid and dotted lines represent the suggested ν Oct planet and its observational uncertainties respectively.*

3.2.4 The Periodic Variation in the Eccentricity of ν Octantis

It was found in Section 3.2.2 that the eccentricity of the ν Octantis planet in a retrograde orbit varies with a period of approximately 40 years, but is this connected to the stability of the retrograde orbit? Figure 3.2.9(a) is a plot of the periodic variations in the eccentricity of a 2.5 M_J planet in the ν Octantis system undergoing prograde motion with a semi-major axis of 0.5 AU, chosen because any value larger than 0.6374 AU becomes unstable. The period of the dominant eccentricity variation (P_e) is 76 years, however, in Figure 3.2.9(b), which is the same orbital configuration except for retrograde motion, the eccentricity period is 148 years, almost double that of the prograde orbit. Note also that a smaller semi-major axis greatly increases the eccentricity period when compared to Section 3.2.2.

To determine the period of the eccentricity a cosine function of the form:

$$e = A\cos\left(\frac{2\pi t}{P_e}\right) + B \tag{3.2.1}$$

was fitted to the eccentricity of each simulation, where A and B are constants. Table 3.3 and Figure 3.2.10 show the results of this procedure.

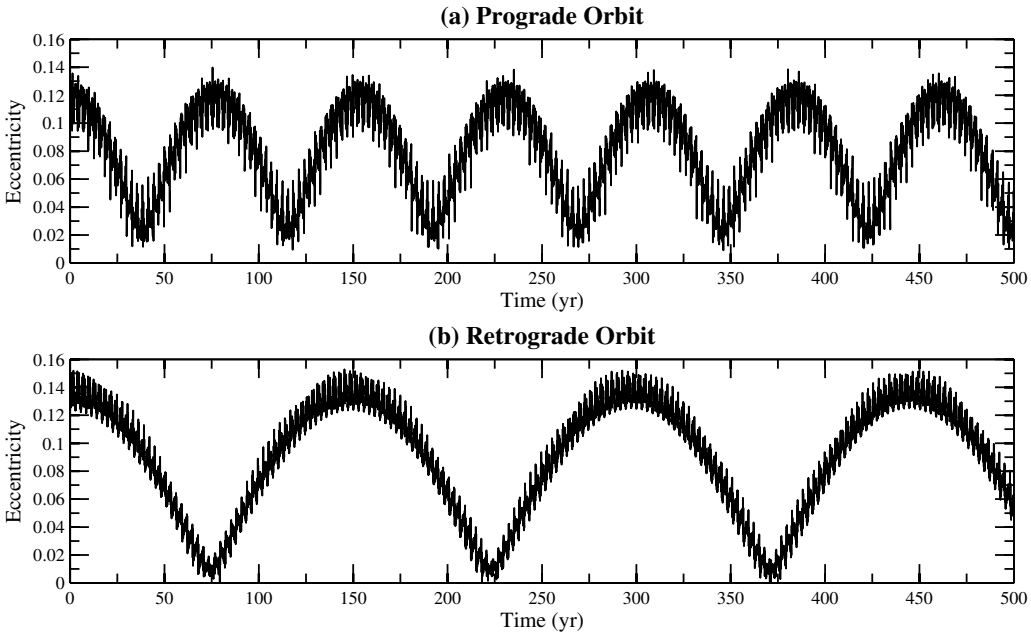

Figure 3.2.9 - *The eccentricity of a 2.5 M_J planet in the υ Oct system with a semi-major axis of 0.5 AU in both a (a) prograde and (b) retrograde orbit over 500 years.*

Table 3.3 - *The period of the eccentricity variations over a range of semi-major axes for both prograde and retrograde orbits.*

Semi-major Axis (AU)	Prograde Orbit Eccentricity Period (yr)	Retrograde Orbit Eccentricity Period (yr)
0.1	1494.64	1679.44
0.2	449.39	549.03
0.3	224.34	308.69
0.4	127.92	204.6
0.5	76.87	148.61
0.6	45.83	113.82
0.8	-	90.16
1.0	-	73.09
1.1	-	49.96
1.2	-	40

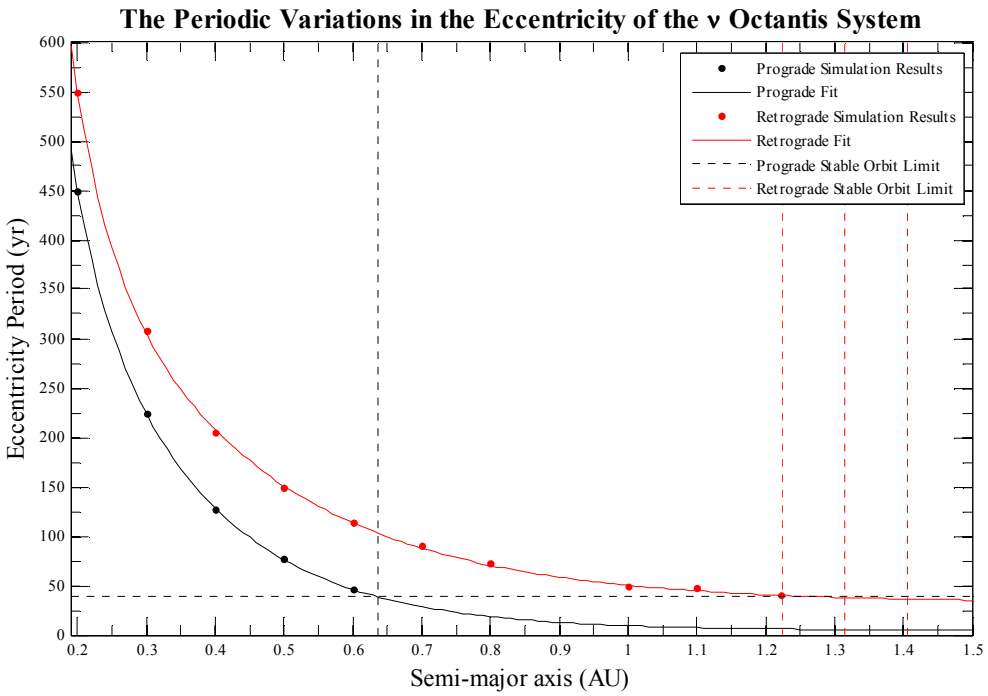

Figure 3.2.10 - *The eccentricity period of a 2.5 M_J planet in the ν Oct system over a range of semi-major axes.*

It was found from these data that both for prograde and retrograde orbits the period of the eccentricity variations decreases with increasing semi-major axis via a second order exponential function of the form:

$$P_e = A_1 e^{-\frac{a_{pl}}{t_1}} + A_2 e^{-\frac{a_{pl}}{t_2}} + A_3, \tag{3.2.2}$$

where A_1, A_2, and A_3 are constants, and $t_1$and t_2 are the decay time constants of the exponential. By fitting the second order exponential to the a_{pl} vs. P_e data in Figure 3.2.10 for both the prograde and retrograde orbits via a least squares fit, it was found that the eccentricity period related to the planet's semi-major axis by the equations:

$$\begin{aligned} P_{e,\,\text{prograde}} = {} & (1086.035 \pm 80.694) e^{-\frac{a_{pl}}{(0.1837 \pm 0.0095)}} \\ & + (9353.726 \pm 619.583) e^{-\frac{a_{pl}}{(0.0419 \pm 0.018)}} \\ & + (4.64 \pm 4.62), \end{aligned} \tag{3.2.3}$$

$$\begin{aligned} P_{e,\,\text{retrograde}} = {} & (750.409 \pm 202.096) e^{-\frac{a_{pl}}{(0.2595 \pm 0.0506)}} \\ & + (7947.312 \pm 1277.356)\, e^{-\frac{a_{pl}}{(0.0511 \pm 0.0065)}} \\ & + (44.083 \pm 10.554), \end{aligned} \tag{3.2.4}$$

where the coefficients of determination (R^2) for the prograde and retrograde cases are both 0.999 and the chi-square values are 0.91 and 7.46, respectively.

It can be seen from both Figure 3.2.10 and equations 3.2.3 and 3.2.4 that the decrease in the eccentricity period with semi-major axis are very similar for both retrograde and prograde motion. However, the retrograde orbits are offset larger than the eccentricity periods of the prograde orbits and also decreases with semi-major axis at a slightly smaller rate.

The SOL for the prograde orbit in the ν Octantis system is 0.6374 AU (Holman and Wiegert, 1999) which is marked on Figure 3.2.10, corresponding to an eccentricity period of 38.48 yr. The SOL for the retrograde orbit was determined to be 1.315 ± 0.092 AU (Sec-

tion 3.2.3) which has a eccentricity period of 39.99 ± 1.74 yr, according to equation 3.2.4. This eccentricity period is similar to the eccentricity period of the SOL for a prograde orbit to within the uncertainties. This suggests there is some kind of a hard limit for which the eccentricity can vary before the orbit becomes unstable.

We know that the variations in the eccentricity are a result of the presence of the secondary star and its gravitational perturbations. It would seem that from these results there is a connection between the orbital stability and the eccentricity period. This tells us that the shape of the a prograde orbit changes more frequently than for an equivalent retrograde orbit and therefore the prograde orbits must be gravitationally perturbed by the secondary star more frequently. The unclear element in this explanation is how does the secondary perturb the prograde orbit more frequently than the retrograde orbit?

To investigate the origin of the smaller eccentricity variations which can be seen in Figure 3.2.9, a Fourier analysis was performed on the eccentricity time series. Figure 3.2.11 is a plot of eccentricity period vs. normalised amplitude over a range of semi-major axes between 0.1 AU to 0.6 AU for the Fourier analysis. It can be seen in Figure 3.2.11 that for each semi-major axis the eccentricity period for both prograde and retrograde motion contains a strong peak at a period of approximately 1050 days corresponding to the period of the secondary star. However, these peaks are not exactly the same as the secondary's period and in the case of the retrograde orbits, this peak appears to increase in period by approximately 75 days over the range of increasing semi-major axis.

The synodic period of two bodies is the amount of time it takes for one body to complete a full orbit relative to the second body. In the case of ν Octantis this is the amount of time between the closest approaches for the secondary star and planet which is different for prograde and retrograde orbits and can be calculated with the following equations:

$$P_{\text{synodic, prograde}} = \left(\frac{1}{P_{\text{planet}}} - \frac{1}{P_{\text{binary}}} \right) \tag{3.2.5}$$

$$P_{\text{synodic, retrograde}} = \left(\frac{1}{P_{\text{planet}}} + \frac{1}{P_{\text{binary}}} \right) \tag{3.2.6}$$

It can be seen in Figure 3.2.11 that there do appear to be peaks corresponding to the exact periods of the synodic periods but they are very weak compared to the secondary's period and the surrounding peaks. However, the surrounding larger peaks increase in period with semi-major axis at a similar increment to the synodic periods, suggesting that they are aliases of the synodic period.

From this analysis it can be concluded that the smaller eccentricity variations are mainly caused by the secondary star's periodic orbit of 1050.11 days, but also consists of a shorter period perturbation when the secondary passes closest to the planet in its orbit about the primary. However, there does appear to be another relatively strong period (compared to the binary perturbation) in both the prograde and retrograde orbits at approximately 525 days which does not move very much with increasing semi-major axis. The cause of this perturbation is most likely due to the secondary star moving from periapsis to apoapsis since it is approximately half the period of the binary.

The variations in the eccentricity also prompted a similar investigation into the variation of the semi-major axis with time. Figure 3.2.12 is a plot of the Fourier analysis of the semi-major axis time series of the suggested planet over a range of semi-major axes between 0.1 AU to 0.6 AU. It can be seen that unlike the eccentricity variations the prograde and retrograde orbits do not contain a period at 1050 days. However, there do appear to be weak peaks close to the synodic periods of each case, but are not as close when compared to the eccentricity variation and so it is not certain if these peaks are a result of the synodic periods.

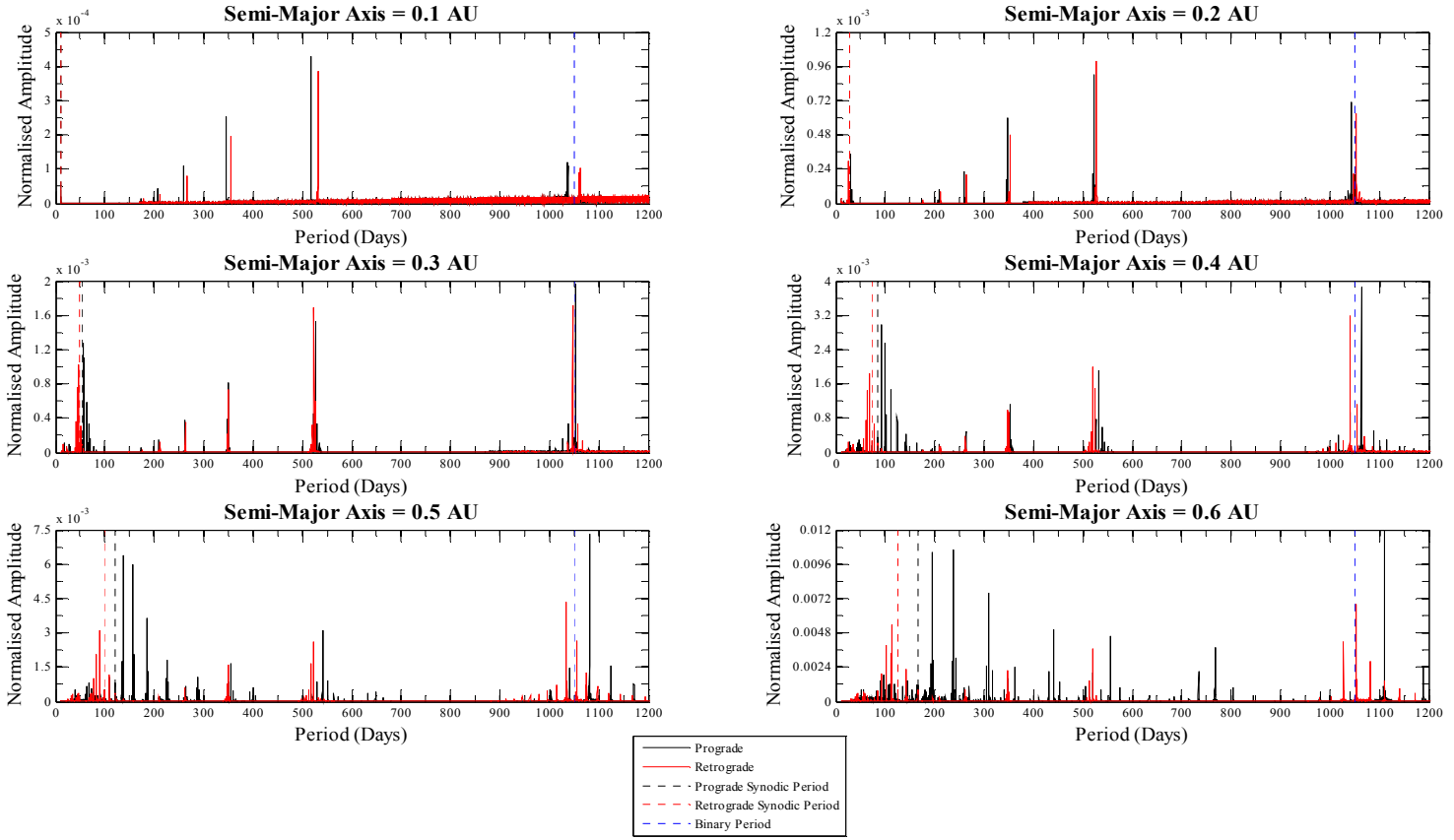

Figure 3.2.11 - *The Fourier analysis of the eccentricity of the 2.5 M_J planet in the υ Oct system over a range of semi-major axes, where the black and red lines represent prograde and retrograde orbits respectively. The vertical black and red dashed lines represent the synodic period for each semi-major axis, while the vertical blue dashed line is the period of the secondary.*

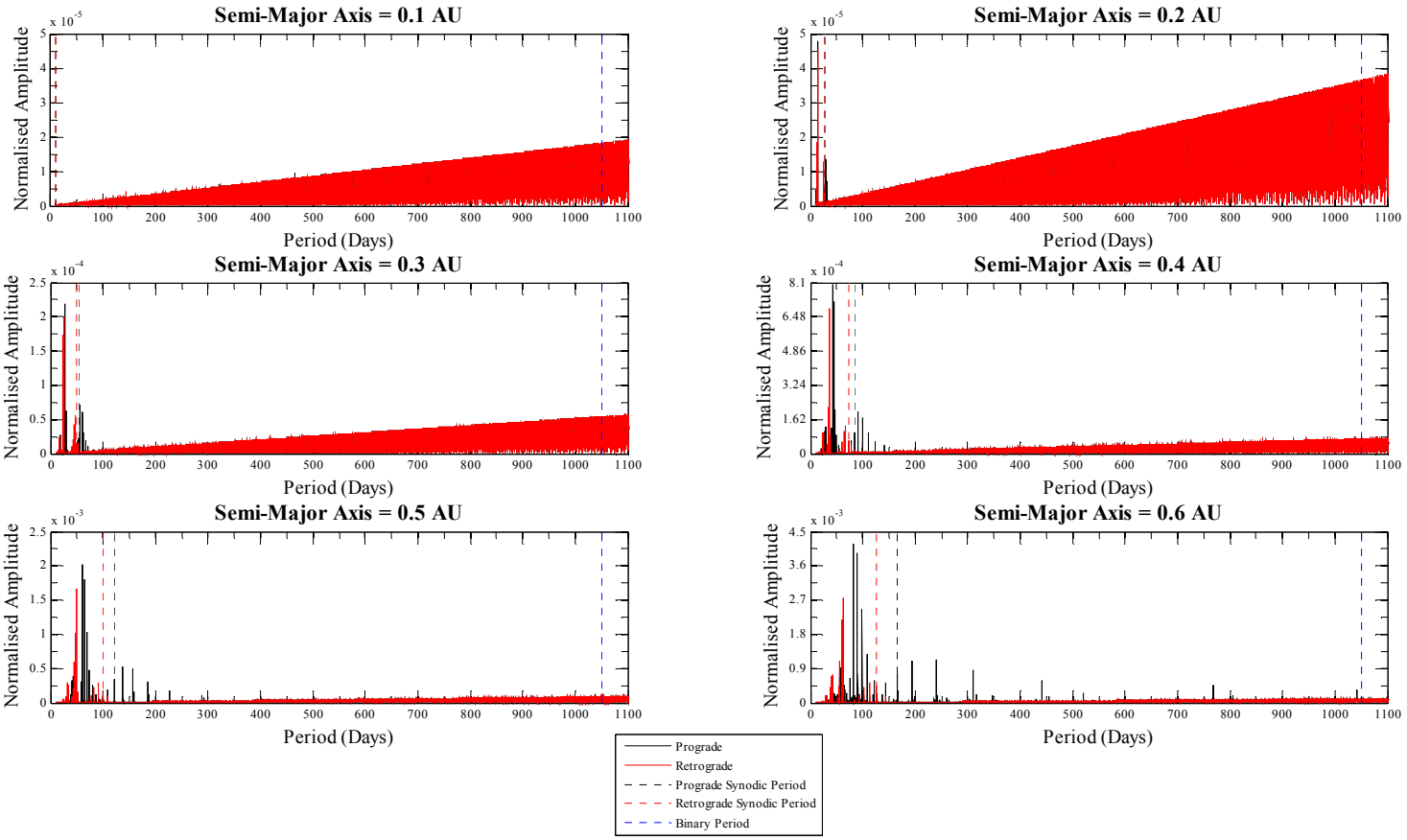

Figure 3.2.12 - *The Fourier analysis of the semi-major axis variations of the 2.5 M_J planet in the v Oct system over a*

3.2.5 Stability of Non-Coplanar Retrograde Orbits

Figure 3.2.11 is a plot of the survival time for a retrograde orbit with a test mass of 2.5 M_J at a semi-major 1.2 AU from the primary star over a range of planetary inclinations between 135° to 225° at a resolution of 5°, which is $\pm$ 45° either side of the 180° coplanar retrograde orbit. The masses and eccentricities for the primary star, secondary star, and the planet used in the simulations were those determined by Ramm et al. (2009), except for the inclinations. The simulations were first performed over a 10^4-yr interval for each inclination to determine which inclinations may survive long-term, that is, inclinations which survived the full simulation. The orbits that survived were then integrated over a 10^5 yr interval and are assumed to be stable if they survived this time period. However, this does not mean they will not become unstable over a yet longer time interval.

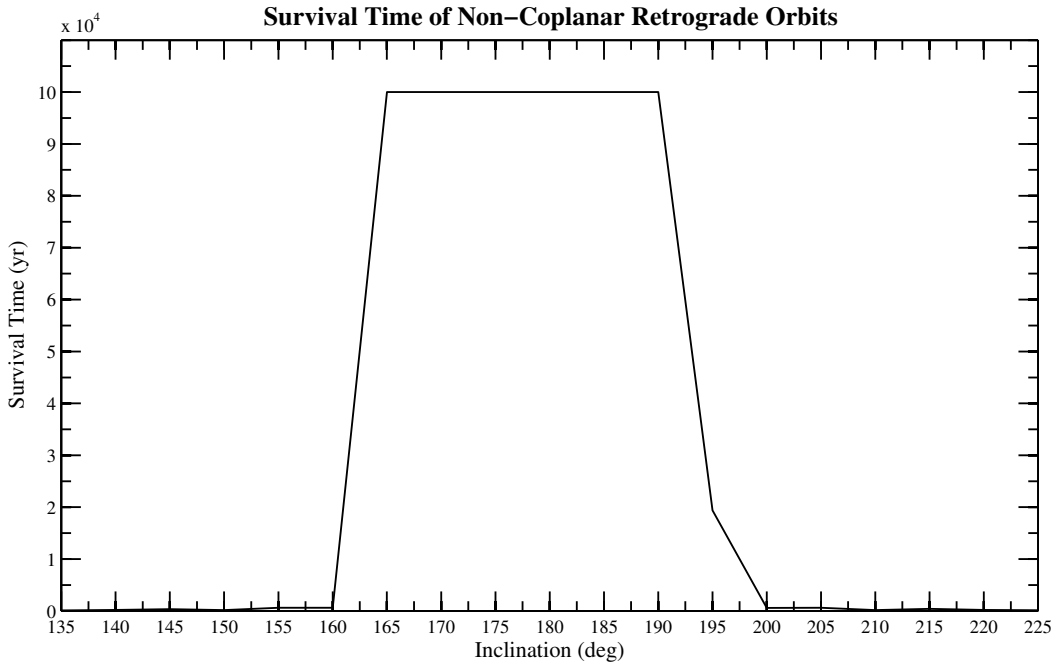

Figure 3.2.13 - *The survival time of a 2.5 M_J planet in the ν Oct system at a semi-major axis of 1.2 AU from the primary in a retrograde orbit over a range of inclinations about the 180 coplanar orbit.*

It can be seen in figure 3.2.13 that stable orbits can exist for the suggested planet between an inclination of about 165° and 190° in a retrograde orbit of the ν Octantis system. All

other inclinations are show to give unstable orbits. Therefore it is possible that the suggested planet could exist within this inclination range. However, one would expect this stable region to be symmetric about 180° (i.e. $\pm$15°), thus the simulation at 195° may be in error.

3.3 Conclusion

It was found from 3-body simulations in Section 3.2.1 that a prograde orbit is definitely not stable with the orbital elements of the suggested planet in the ν Octantis system, which only survived 12 years in the system before being ejected as a result of the gravitational perturbations of the secondary star. However, a retrograde orbit with the same orbital elements remains very stable over the same time period. It was also found that the eccentricity of the retrograde case varied periodically with a period of about 40 years.

The long-term 100 million-year simulation of the ν Octantis planet retrograde orbit showed that retrograde stability is very likely for this orbit. It was found that the maximum distance between the two stars and also between the planet and primary star represented the apoapsis and periapsis of the two orbits. This shows that both the secondary and the planet behave as if they are in a two-body keplerian system. Therefore it can be assumed that these variations in distance from the primary star are caused by the eccentricity of the corresponding orbits rather than from some long term effect. The periodic variation in the eccentricity of 40 years was also found to remain consistent for the 100 million years and could be a connection to the stability of the retrograde orbit.

It was found from 3-body simulations in Section 3.2.3 that the ν Octantis system consists of an inner stable region where all orbits are stable and an outer unstable region where the majority of orbits are unstable. The cut-off point for stable orbits depended largely on the mass of the primary, in that a larger mass gives a larger stable orbital region, while the secondary mass and planetary eccentricity only affect it a little. The 'outer region' (semi-major axes, on average, larger than 1.315 AU) appears to depend on the mass of the secondary and the planetary eccentricity, whereby a larger mass or eccentricity gives rise to

more unstable orbits. The mean stable orbit limit was determined to be $a = 1.315 \pm 0.092$ AU which agrees with the findings of Eberle and Cuntz (2010) and encompasses the orbit of the suggested ν Octantis planet.

The orbit of the suggested planet is said to be in a 5:2 mean-motion resonance with the secondary star and so in order to investigate the other mean-motion resonances a plot representing the fraction of stable orbits for a range of period ratios was calculated from the simulations of different mass ratios and eccentricities within the observational uncertainties. It was found that the suggested planet has a probability of 80 per cent at surviving 10^4 years while the 3:1 resonance has a 100 per cent probability. However, other mean-motion resonance such as 2:1, 7:4, and 3:2 have less than a 30 per cent probability of surviving the entire integration and so are considered not to viable. Thus the most likely case is that retrograde orbits give larger regions of orbital stability and that resonance is not a key factor in the stability of the suggested planet.

In Section 3.2.4 the variation in the eccentricity with time of the suggested planet was investigated. It was found that the period of the dominant eccentricity variation depends on the semi-major axis by a second order exponential relationship, where the larger the semi-major axis the smaller the eccentricity period. It was also found that the relationship for prograde orbits tends to have much smaller eccentricity periods when compared to the retrograde orbits and also decreases at a slightly greater rate with increasing semi-major axis. The eccentricity period for the SOL of both the prograde and retrograde orbits were both found to be approximately 38.48 years, which suggested that there is a hard limit for how frequently the shape of the planet's orbit can change.

The Fourier analysis of the eccentricities over time for each semi-major axis used in Section 3.2.4 showed that the smaller eccentricity variations corresponded mainly to the period of the secondary star and the synodic period of each case.

In Section 3.2.5 non-coplanar orbits were investigated to learn more about the characteristics of the ν Octantis system. It was found that in addition to the coplanar retrograde orbit at an inclination of 180° for the suggested planet, inclinations between about 165° to 190° allow for stable orbits to exist and therefore the planet could very well have an inclination within this range.

Chapter 4

ν Octantis Observations

4.1 Introduction

The simulations in Chapter 3 showed that a planet orbiting the primary star in a retrograde orbit at 1.2 AU for the ν Octantis system is definitely possible. However, more physical and precise radial velocity observations are needed to determine if the planetary perturbation continues to remain stable.

The radial velocity of the ν Octantis primary star was observed by taking advantage of the wobble about the system's barycentre, caused by the presence of the secondary star and possibly a planet, as shown in Chapter 1. Spectra were recorded using the High Efficiency and Resolution Canterbury University Large Echelle Spectrograph (HERCULES) by capturing the light of ν Octantis through the 1-m McLellan telescope situated at Mt John University Observatory (MJUO). These spectra are then reduced by the HERCULES reduction software package (HRSP) (Skuljan, 2007) and the Doppler shift between a ν Octantis pri-

mary template spectrum measured to obtain the radial velocity between December 2009 and January 2012.

In order to acquire high precision radial velocities an iodine absorption cell was incorporated into HERCULES which imprints an iodine spectrum into the observed stellar spectra. This acts as a stationary reference spectrum allowing the measurement and elimination of any radial velocity perturbations caused by instrumental effects.

Once the radial velocities are extracted from the spectra the orbital solution for the ν Octantis binary is determined and in turn the orbital solution of the planetary perturbation. This will then be compared to the Ramm et al. (2009) orbital solutions to see if the orbital elements have changed significantly in any way, which could be an indication that the perturbation is not caused by a planet. However, if the elements remain within the uncertainties one can conclude that the perturbation is stable and therefore this would be strong evidence for a planet orbiting the primary star.

Bisector analysis of spectral lines (Gray, 1983) is the measurement of the position of the line centre over a range of intensities between the line's peak value and the continuum, which is a good measure of line asymmetry. Asymmetry in spectral lines can be attributed to stellar processes such as radial/non-radial pulsations, or the rotational modulation of the velocities caused by star spots or patches and active regions. Therefore, if a correlation is found between the radial velocity perturbation and the line asymmetry, one can conclude that the perturbation may not the result of an orbiting planet (see e.g. Povich et al., (2001); Queloz et al., (2001)). A bisector analysis was done on the ν Octantis spectra for the three spectral lines at wavelengths 6109 Å (NiI), 6174 Å (FeI), and 6247 Å (FeI), which were chosen within the recommended region for K-giant stars by Gray (1983), for the lack of iodine lines in this region, and because they were non-saturated unblended and clearly defined spectral lines.

4.2 Acquisition of ν Octantis Spectra

4.2.1 The HERCULES Spectrograph, CCD and Telescope

The High Efficiency and Resolution Canterbury University Large Echelle Spectrograph (HERCULES) was used for the acquisition of ν Octantis spectra. HERCULES receives light from ν Octantis through the f/13.5 Cassegrain focus of the 1-m McLellan telescope situated at Mt John University Observatory (43.987° S, 170.463° E). The stellar light is passed to the spectrograph through a fibre optic cable with a core diameter of 100 μm over a distance of approximately 22-m (Hearnshaw et al., 2002). Three fibres with different resolving powers are installed on HERCULES and are mounted in the focal plane of the spectrograph. Fibre 3 is used for all ν Octantis spectra and gives a resolving power of 70000 (Hearnshaw et al., 2002), and giving a 4.5" angular size of the fibre core projected onto the sky plane. The choice of fibres can be made manually on the fibre-feed module which then directs either starlight, light from a Th-Ar cathode lamp or a white smooth-field lamp light into the chosen fibre.

A Watec 120N video camera is used as a guide camera and is installed at the focal plane of the telescope using a beam splitter to redirect 8 per cent of the star's light to this camera (Hearnshaw et al., 2002). This camera can be used for image acquisition as well as autoguiding.

HERCULES uses a large R2 31.6 gr/mm echelle grating from the master ruling MR152 (Hearnshaw et al., 2002). The grating has a blaze angle of 64.33° (Hearnshaw et al., 2002) which confers considerable simplicity on the optical design and permits prism cross-dispersion before and after the echelle grating, therefore giving a high efficiency spectrograph. The ruled area of the echelle grating has dimensions of 204 × 408 mm (Hearnshaw et al., 2002) and is a relatively coarse ruling allowing for smaller angular widths of the orders which is optimum for the CCD being used.

HERCULES uses a single BK7 prism cross-dispersion (PH3 quality glass: refractive index deviation no more than $\pm 2\times10^{-6}$) in double-pass mode. This was chosen because of the

high peak efficiency of 80 per cent and a larger wavelength range when compared to a grating, which typically has a 70 per cent peak efficiency and a wavelength range limited by the blaze angle (Hearnshaw et al., 2002). The double-pass mode allows us to record more of the spectrum on the CCD by vertically partitioning the spectrum, whereby the end of one order represents the start of the next order. Figure 4.2.1 shows the format of a single spectral image produced by HERCULES.

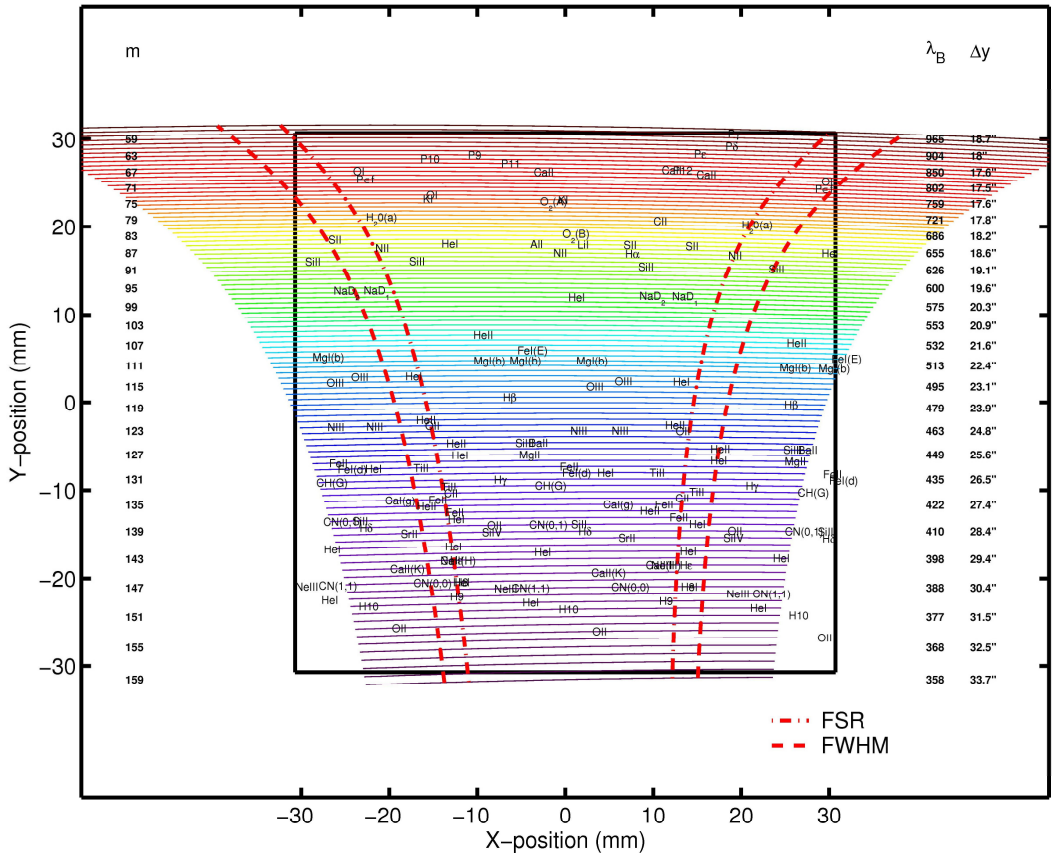

Figure 4.2.1 - *The spectral format of HERCULES. Shown are orders m = 65 (875.1nm) to m = 150 (379. 3 nm) . The CCD has been rotated by 3° so that the slope of the orders is minimized. This has the effect of slightly increasing the average line tilt (Hearnshaw et al., 2002).*

The camera used to image the spectra produced by HERCULES is a folded Schmidt which gives outstanding performance with respect to aberrations over a very large wavelength range of 380 - 880 nm and with high efficiency. The CCD has a 60 mm square 4130 × 4096 pixel chip which allows for a large wavelength range to be recorded in a single expo-

sure and is attached to the exterior of the HERCULES vacuum tank for easy removal, recoding spectra through a flat-fielding lens which acts as a window.

The folded flat mirror within HERCULES (part of the folded Schmidt camera) contains a perforation in which some light is lost. This light is instead redirected by a diagonal mirror and relay lenses to a photomultiplier. The photomultiplier is mounted externally similar to the main camera and can be used to determine the flux-weighted time of mid-exposure. It can also be used to assist the observer when fine-tuning the position of the star on the fibre entrance (i.e. the star is centred when the photon count rate is at a maximum) and it is also used to predetermine the exposure time required to obtain a given signal.

HERCULES is housed in a vacuum tank which is set to a constant pressure of about 3 torr and is also set at a constant temperature of 21 $^{\circ}$C, which is kept constant by putting HERCULES in a totally controlled environment (i.e. an isolated room heated to a constant temperature). This is done to prevent short-term changes in the refractive index of the medium inside the spectrograph and hence the shifting of spectral lines which can be confused with Doppler shifts. The importance of preventing short-term pressure and temperature changes is emphasized by considering that a 1 mbar increase in pressure at about one atmosphere gives a spurious Doppler shift of -80 m s^{-1}, while a change in temperature from 24℃ to 25℃ gives a velocity shift of +240 m s^{-1} (Murdoch et al., 1993). This would prevent any observations of Jupiter mass planets such as in the ν Octantis system. HERCULES also has no moving parts and so is stable both thermally and mechanically to a high degree. Figure 4.2.2 shows the optical design of HERCULES.

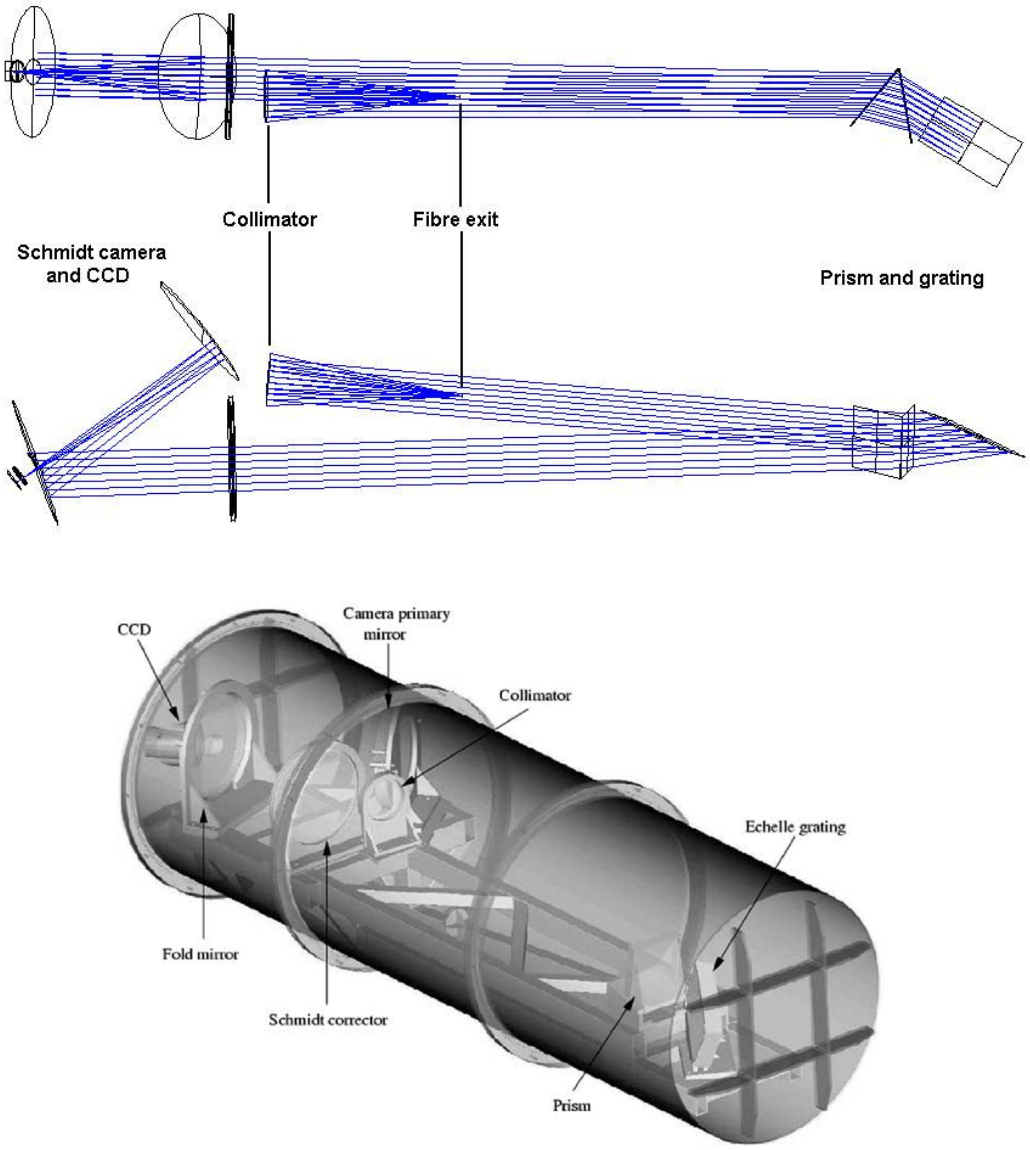

Figure 4.2.2 - *The optical design of HERCULES (Hearnshaw et al., 2002).*

4.2.2 The Iodine Absorption Cell

Conventionally, the measuring of Doppler shifts in optical spectra involve the determination of a wavelength-scale by a reference spectrum of known wavelengths. The wavelength-scale is then used to determine the wavelengths of the stellar spectral lines over time and therefore the Doppler shift with respect to some stellar template spectrum. The errors in Doppler shift measurements are typically larger than that of just photon statistics and are

thought to be the result of the two different optical paths taken by the stellar and reference spectra. The two exposures are usually taken at different times therefore spectrograph flexure, detector movement, different photocentres at the slit, and dissimilar illumination of imperfect optics cause spurious shifts and distortions in both the precision and point spread function (PSF). The average precision HERCULES has obtained for sharp-lined late-type stars by this method is about 14 ms^{-1} (Hearnshaw et al., 2002) using a Th-Ar lamp.

Griffin and Griffin (1973) suggest this problem could be solved by first passing the stellar light through an absorbing medium, thereby superimposing reference absorption lines in the stellar spectrum. The reference spectral lines will undergo the same instrumental effects and distortions at the same time as the stellar spectral lines and thus by subtracting the resulting instrumental shift of the reference lines one can eliminate any instrumental errors in the final radial velocity. Griffin and Griffin (1973) showed that by using the O_2 telluric band at 6300 Å in the Earth's atmosphere they could theoretically achieve a precision of about 10 ms^{-1}. Campbell et al. (1979) took this one step further by using a stabilised hydrogen fluoride gas absorption spectrum in front of the coudé spectrograph of CFHT, obtaining a precision of 15 ms^{-1}.

Marcy and Butler (1992) were the first to implement the use of a molecular Iodine (I_2) absorption cell in an echelle spectrograph to obtain precise radial velocities. The motive behind choosing an I_2 absorption cell is that it provides a strong absorption coefficient, producing sharp and stable spectral lines over a range of wavelengths between 5000 Å to 6300 Å with at least two 'features' per Å, and requires a path length of only a few centimetres. For an atlas of molecular iodine and a discussion on its origin see Gerstenkorn and Luc (1978). The major advantage of an I_2 cell is that it can be used to measure the instrument profile (IP) of a spectrograph (Valenti et al., 1995) and then used to obtain very precise radial velocities (Butler et al., 1996), therefore allowing the detection of lower mass and longer period planets, which would otherwise be lost in the RV errors. One example of this is the cases of ε Eridani and γ Cephei, which were claimed by Walker et al. (1995) to have no planets present. However, planetary companions were found after combining their data with McDonald Observatory data obtained using an I_2 absorption cell (Hatzes et al., 2000, 2003).

From the beginning of 2007 HERCULES began using an I_2 absorption cell situated just before the Cassegrain focus. The arrangement was further developed in March 2011 by placing the cell in a pinhole relay system just ahead of the fibre entrance. In this arrangement the I_2 absorption cell has the option of being moved out of the optical path both manually and automatically for white lamp and Th-Ar lamp exposures. The I_2 absorption cell is set at a temperature of 50 ± 0.1 ℃ with an optical path of 100 mm. It should be noted that in March 2011 a new I_2 absorption cell was installed which contains slightly stronger spectral lines. Endl et al. (2009) analysed 963 α Cen A observations taken in April 2009 with HERCULES and obtained a precision of 2.68 ms^{-1}. This same setup was used in the acquisition of ν Octantis spectra.

4.2.3 Mt John Observing Program

The α Cen observing program at Mt John University Observatory consists of several stars including ν Octantis, with observations beginning in January 2009. On average there are approximately 14 days of observing sessions per month, where about 2-4 ν Octantis full CCD chip spectra are recorded per run. Several observers have been trained to use HERCULES and the telescope to capture high quality spectra on their assigned star list. These observers include: Fraser Gunn, Erik Brogt, Pam Kilmartin and John Hearnshaw.

At the beginning of each observing session observers are asked to take 15 spectra of a white lamp with the iodine cell removed, each exposure is 30 seconds. When observing ν Octantis observers use the guide camera to first position the star over the fibre attached to the telescope focal point which is done by determining the position that gives the most photon counts on the exposure meter. Then the guide camera is set to automatically guide on the star for the entire ν Octantis exposure. ν Octantis exposures with the iodine cell in the optical path range between 10 and 20 min, which is roughly calculated from the photon count rate so as to obtain a total photon count of at least one million, sometimes three million counts, depending on seeing. Once per month a long 60-min exposure is done so as to record the faint calcium H and K lines. In addition to the ν Octantis spectra, a Th-Ar lamp is used to obtain a Th-Ar spectrum for wavelength calibration. These are 30-second expo-

sures with the iodine cell removed, taken both before and after a single ν Octantis exposure.

4.3 Reduction of Spectra

4.3.1 HERCULES Reduction Software Package (HRSP)

HRSP is a software package written by Skuljan (2007) to reduce spectra recorded by HERCULES. The reduction procedure consists of four main steps: preparation, wavelength calibration, white lamp reduction, and extraction of stellar wavelength data. The raw image size of a full CCD chip exposure is 4130 × 4096 pixels and so in preparation for reduction all raw spectral images are cropped. The cropping includes removing 30 pixel rows from the top and bottom of the images which contain no data, and are also cropped to isolate the pixel rows 2000 to 3200, the region containing the usable echelle orders 89 to 120. The spectra are then rotated +90° giving a final image size of 4036 × 1200 pixels. Fig. 1 is an example of a prepared ν Octantis spectrum.

Figure 4.3.1 - *The prepared image of a ν Oct spectrum taken on the 20th of December 2009 (JD2455186).*

The second step involves calibrating the wavelength-scale using the Th-Ar spectra. This is done by first performing a course alignment with a reference Th-Ar spectrum of known wavelengths by cross-correlating the two spectra over a range of angles between +2° and

−2°. The cross-correlation profile with the largest peak tells us the shift in the vertical and horizontal axes with respect to the reference spectrum giving a rough location of known spectral lines. Gaussian functions are then fitted to the known spectral lines over several iterations by first looking at the image centre then expanding to include more spectral lines, thus determining the line centres of each known spectral line in the image. The result is a table of transformation coefficients between absolute coordinates and pixel coordinates, which is saved in a file called 'transform.fit'.

The third step involves the reduction of the white lamp spectra to create a one-dimensional flat-field image, whereby a set of whites taken at the beginning of a session are combined by averaging the intensities of each pixel. Then the maximum pixel value over the entire image is determined so as to divide every pixel's intensity by this value and normalise it to one. The echelle orders of the white spectrum are also located by first converting to absolute coordinates using the table 'transform.fit' and then determining the minimum and maximum orders, respectively. Each pixel column is then examined and a gaussian function is fitted to each order giving three polynomial regression coefficients for each echelle order defining the central pixel position, full width at half maximum (FWHM), and the absolute order number, which is stored in a file called 'order.fit'.

The fourth and final step involves the reduction of the stellar spectra. The barycentric corrections in terms of the apparent right ascension, apparent declination, radial velocity, and Julian date are all calculated by specifying the star name (i.e. 'nu Octantis'), Hipparcos catalogue number, and the flux-weighted-mean time of exposure in Julian date format. HRSP uses an inbuilt Hipparcos catalogue for astrometric parameters, and a Barbier-Brossat and Figon (2000) catalogue for radial velocities. In order to remove any background scattered light from the stellar spectrum a median filter is applied, whereby every pixel is replaced by the median value of the surrounding pixels and is stored as a separate image. Then a background image is created by fitting a polynomial to the regions between the echelle orders of the median image. Therefore to remove any background scattered light one subtracts the background image from the raw spectral image. In order to remove any cosmic-rays each order of this image is then divided into boxes and a low order polynomial is fitted to each pixel row. If any pixel is found to be too high above the fitted value

then it is considered to be a cosmic-ray and so is replaced by the fitted value. Whenever this occurs the procedure is repeated to make sure the cosmic-ray is fully removed.

The echelle orders are extracted from the stellar image into intensities (ADU) and corresponding pixel number by first determining the locations of the orders from 'order.fit', created earlier. Then for each pixel column in an order of size 2.2 FWHM units, the sum of the pixel values is calculated and written into the extracted image. The extracted image is then divided by the flat-field image to remove any pixel to pixel variations in the CCD.

In order to obtain a precise wavelength-scale the Th-Ar emission spectra taken before and after the stellar spectra are first analysed to determine the pixel positions of the known calibration lines determined in 'transform.fit'. The dispersion solution is calculated as a two-dimensional polynomial regression of the form (Skuljan, 2007):

$$\text{Pixel}_{\text{centre}} = \sum_{j=0}^{k} \sum_{i=0}^{n} a(r) [m\lambda]_{\text{norm}}^{i} \, m_{\text{norm}}^{j}, \tag{4.3.1}$$

$$r = (n+1)j + i + 1, \tag{4.3.2}$$

$$(m\lambda)_{\text{norm}} = \frac{m\lambda - 564000}{10000}, \tag{4.3.3}$$

$$\text{and} \quad m_{\text{norm}} = \frac{157 - m}{81}, \tag{4.3.4}$$

where m is the absolute order number, λ the wavelength in Angstroms, k and n are the polynomial degrees, and $a(r)$ is the $k \times n$ matrix containing the dispersion solution coefficients, with r as the index. The dispersion solutions for each Th-Ar spectrum are then interpolated to the flux-weighted-mean time of exposure, thus taking into account any instrument movement between exposures. This dispersion solution is then used to calculate the air-wavelength of each pixel position, which is written to a text table with corresponding intensity values.

4.3.2 High Precision Radial Velocities

To obtain high precision radial velocities from the observed ν Octantis spectra an algorithm developed by Endl et al. (2000) and combined into a software package called 'Austral' was used. The algorithm can be divided into three major steps: reconstruction of instrumental effects and spectrograph instrument profiles by modelling pure iodine spectra using a high resolution Fourier transform spectrum (FTS) of an I_2-cell, deconvolution of the 'template' stellar spectrum using the maximum entropy method and the instrument profile, and complete modelling of the combined iodine and stellar spectra to determine the Doppler shift between the reference iodine and stellar absorption lines, respectively.

In order to obtain the high precision radial velocities one first needs to model a pure iodine spectrum recorded on the same spectrograph as the observations, which can be obtained on HERCULES by exposing a white lamp spectrum with the I_2-cell in the light path. In an ideal case the instrument would image the 'source' spectrum exactly as it is. However, because of diffraction and optical imperfections the observed spectrum g(x) is a combination of the intrinsic spectrum $f(x)$ and a convolving function ϕ corresponding to the instrument profile (IP). In general the IP is the instrumental point spread function in the dispersion direction and can be represented by a simple gaussian function centred on zero pixels, where the amplitude, and FWHM depend on the instrument being used. The convolution of the observed spectrum and IP can be described mathematically as (Valenti et al., 1995):

$$g(x) = \int_{-\infty}^{\infty} f(x')\phi(x - x')dx. \tag{4.3.1}$$

The goal is to approximate the function ϕ by reconstructing the observation with an appropriate model and thus deconvolving the IP from $g(x)$ to obtain an approximation of the observed intrinsic spectrum. This is done by first taking a high resolution FTS of the pure I_2-cell giving an iodine spectrum assumed to contain no instrumental alterations. Endl et al. (2000) obtained this by scanning their I_2-cell on the McMath FTS at Kitt peak, yielding a resolving power of R = 400,000 and this is the same model used in this thesis. In order to prevent strong cutting of the line peaks the FTS is ten times oversampled.

In order to approximate the IP, Endl et al. (2000) first divided the observed spectrum into chunks of 100 pixels wide (about 2 Å), oversampling the data by a factor of five and then modelled the observed spectrum using a multi-parameter χ^2 - optimisation algorithm (Press et al., 2007, Sect. 10.2) which derives information about the IP shape, dispersion solution, continuum slope, and line depth of each spectral chunk. The IP is then convolved with the I_2-FTS part corresponding to each chunk, where the first iteration uses a default gaussian function with parameters (wavelength zero-point, line-depth, and slope parameter) set to zero (Endl et al., 2000). After the first iteration the optimisation algorithm starts and iterates until $\chi^2 = N$ or a flat gradient of the χ^2- function is reached (Endl et al., 2000), thus obtaining the IP at the time of observation. The algorithm also includes several modes to model the IP, for example, the convolution of a box-function and a gaussian which allows optimisation of the width of both the box and gaussian functions, or a multi-gaussian function for asymmetric IP, where it models a symmetric main gaussian and up to four smaller gaussians in the wings. Furthermore, the Maximum Entropy Method (MEM) (Cornwell and Evans, 1985) can be used to apply additional corrections.

The second step is to obtain a pure high resolution stellar spectrum (i.e. ν Octantis) and deconvolving it with the IP obtained in the first step, which is done by employing the use of the MEM. Endl et al. (2000) tested this algorithm on simulated data convolved with a predefined IP and found the MEM deconvolution successfully recovers the structure of the intrinsic spectrum.

The final step involves modelling the combined stellar and iodine spectra to obtain the radial velocities. The combined stellar and iodine spectra are taken by inserting an I_2-cell into the light path of the stellar spectrum as described in Section 4.2.2. Thus mathematically the function *f* is simply the product of the intrinsic stellar and iodine spectra, and therefore the I_2-FTS and deconvolved stellar model from the previous step can be used to synthesize the observations. In order to compute the radial velocity one must first model the combined spectrum in the same way as the pure iodine in the first step, but now with additional parameters in the χ^2 - optimisation algorithm to account for two spectra instead of one. This then allows us to reconstruct the IP for a specific observation, modelled by a multi-gaussian plus MEM correction. The IP is then deconvolved from the observation to obtain a model of the intrinsic stellar and iodine spectra. It should be noted that the com-

bined stellar and iodine spectra are also divided into 90-pixel chunks which are modelled independently, and therefore each chunk can be treated in the overall RV statistic as providing one independent radial-velocity measurement.

Once the best-fit model is computed the radial velocity of the star may be computed from the Doppler shift between the iodine and star model. This is done by using the wavelength zero-point and dispersion parameters from the observation's model and calculating the wavelength for each oversampled pixel, for both the iodine and stellar models. From this one can calculate the Doppler shift between the iodine and stellar lines and hence the radial velocity of the star and iodine correction, which in turn is subtracted from the star's radial velocity. Each spectral order typically contains 35 chunks which are analysed per order, and so if a chunk has a radial velocity greater than 3σ from the mean of that order then it is rejected. Thus the raw radial velocity is the mean over all chunks for each order. The error in each observation is calculated as the mean standard deviation (RMS/$\sqrt{N}$, where N is the number of unrejected chunks). Finally the barycentric correction is applied, which was calculated by HRSP.

4.4 Results and Discussion

4.4.1 Raw Radial Velocities of ν Octantis

Figure 4.4.1 shows the radial velocities of ν Octantis corrected to the solar system bary-centre. The plot covers both the observations reduced in this thesis, taken after JD2455184 (see Table 6.1 in Appendix), and the observations reduced by Ramm et al. (2009) taken between JD2452068 to JD2453928. The 590 observations reduced in this thesis unfortu-nately do not cover a full binary orbit of 1050 days, therefore fitting the binary keplerian orbit to these data alone will not produce an accurate solution, and in turn an inaccurate planetary solution. However, in an attempt to solve this problem before the thesis deadline the radial velocities from Ramm et al. (2009), which covered multiple binary orbits can be used in combination with the current observations to model an accurate binary orbit. This therefore gave a grand total of 811 observations of the ν Octantis spectrum over an interval of 10.6 years.

To determine the keplerian solution for both the binary and planet the data were fitted by a least-squares differential correction approach, that is the Kepler equation:

$$V = K(\cos(\theta + \omega) + e\cos\omega), \tag{4.4.1}$$

was fitted to the observations as described in Sterne (1941) via the equation:

$$\begin{aligned}\Delta V = {} & (\cos(\theta+\omega) + e\cos\omega) \\ & + K\left[\frac{\left(\cos\omega - \left(\sin(\theta+\omega)\sin\theta\,(2+\cos\theta)\right)\right)}{1-e^2}\right]\Delta e \\ & - K\left[\sin(\theta+\omega) + e\sin\omega \right. \\ & \left. - \frac{(\sin(\theta+\omega)\,(1+e\cos\theta)^2)}{(1-e^2)^{3/2}}\right]\Delta\omega\end{aligned} \tag{4.4.2}$$

$$+\left[\sin(\theta+\omega)\,(1+e\cos\theta)^2\,\frac{2\pi K}{P(1-e^2)^{3/2}}\right]\Delta T_0$$

$$+\left[\sin(\theta+\omega)\,(1+e\cos\theta)\,\frac{2\pi K(t-T_0)}{P^2(1-e^2)^{3/2}}\right]\Delta P,$$

where the Δ[elements] represent the change in the orbital elements needed to obtain the best-fit (i.e. $K = K_0 + \Delta K$), and ΔV is the difference between the observed radial velocity and the current iterated fit. This least-squares method requires an initial 'first-guess' for each orbital element and is then repeated until convergence has been obtained.

It is known from Ramm et al. (2009) that an extra perturbation exists in the radial velocities of ν Octantis and so in order to obtain precision orbital elements best representing both the binary and planetary solutions an iterative procedure of least-squares fitting was devised. First a single-keplerian is fitted to the all 811 radial velocities (including Ramm et al. (2009) data) with the initial orbital elements chosen from Ramm et al. (2009). The residual radial velocities to the binary solution for the current data and the Ramm et al. (2009) data are then fitted to a single-keplerian separately and in turn subtracted from their respective raw radial velocities, leaving only the binary radial velocity perturbation. One then fits a single-keplerian to all the data points of the modified data to determine an orbital solution for the binary alone. The binary solution is then subtracted from the raw data to give a more accurate representation of the planetary perturbation. This process is then repeated until the orbital elements converge. The standard errors for each element have been estimated using methods of numerical simulation by generating 100 copies of the original radial velocities and replacing them with random values from a gaussian distribution determined by rms error of the original least-squares fit. Then a single-keplerian is fitted to each random copy to determine the orbital elements. One then calculates the standard deviation of each orbital element to obtain the corresponding standard error.

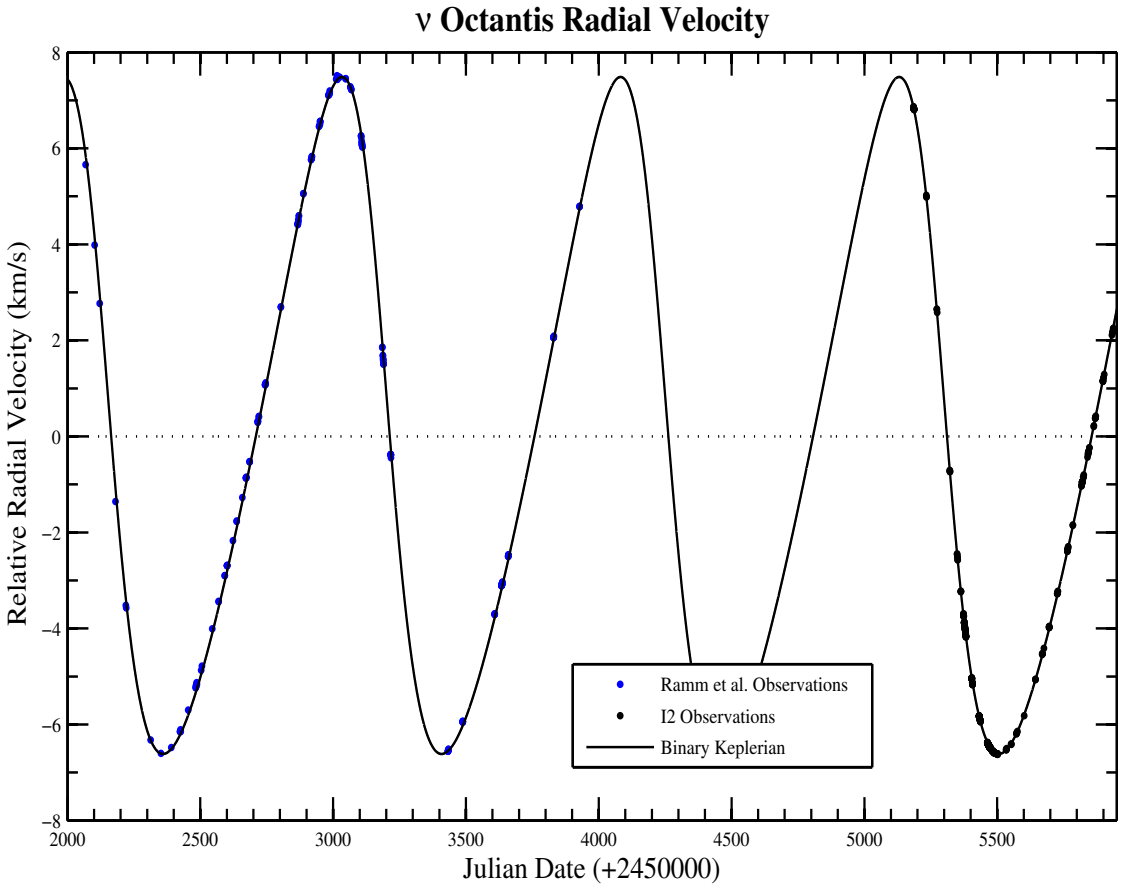

Figure 4.4.1 - *The relative radial velocity observation (dots) of the ν Oct binary corrected to the barycentre of the solar system and the corresponding line of best-fit (solid-line) as a result of the gravitational perturbation of the secondary star on the primary star about the centre of mass. Note observations between JD2452068 to JD2453928 were reduced in Ramm et al. (2009).*

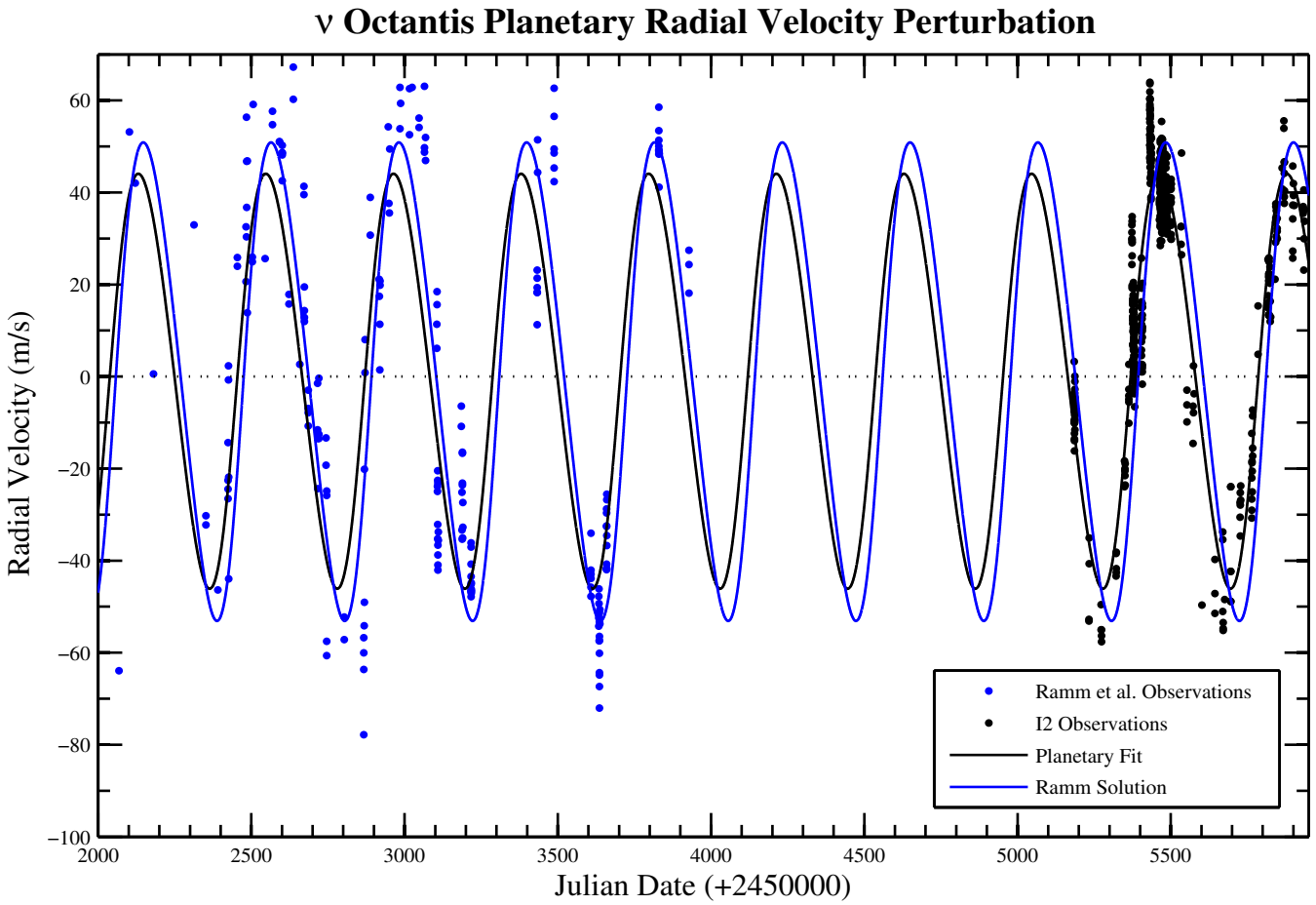

Figure 4.4.2 - *The relative radial velocity observation (dots) of the suggested planet orbiting the ν Oct primary star with the corresponding line of best-fit (solid-line) and the orbital solution derived by Ramm et al. (2009) (blue solid-line). Note observations between JD2452068 to JD2453928 were reduced in Ramm et al. (2009).*

Table 4.4.1 - *The orbital elements derived from the ν Octantis binary and planetary solutions. The binary orbital solution was determined from the combination of the Ramm et al. (2009) data and the current data. The planetary orbital solutions is derived from just the I_2-cell observations, while the second planetary orbital solution is derived from just the Ramm et al. (2009) data. The last planetary orbital solution is derived from the combination of the two data sets.*

ν Octantis	Number of data points	K_1 (kms^{-1})	e	ω_1 (°)	$T_{0,1}$ (24...)	T (24...)	P (d)	γ (kms^{-1})	$a_1 \sin i$ (Gm)	f_{M1} $(M_\odot)$	Fit rms (ms^{-1})
Primary keplerian	**811**	**7.0425**	**0.23659**	**75.363**	**52959.627**	**53179.95**	**1050.04**	**-**	**98.887**	**0.035012**	**-**
±		0.0008	0.00010	0.027	0.024	0.22	0.02	-	0.021	0.000019	
Perturbation (I_2-cell only)	**590**	**0.0450**	**0.096**	**256**	**52560**	**52857**	**416.4**	**-0.014**	**0.2570**	$\mathbf{3.90 \times 10^{-9}}$	**9.6**
±		0.0008	0.015	11	14	18	2.1	0.001	0.004	0.21×10^{-9}	
Perturbation (Ramm et al. (2009) data)	**221**	**0.0517**	**0.090**	**273**	**52574**	**52894**	**422.0**	**0.003**	**0.299**	$\mathbf{5.98 \times 10^{-9}}$	**23.5**
±		0.0017	0.035	34	4	40	4.2	0.001	0.011	0.62×10^{-9}	
Perturbation (combined)	**811**	**0.0449**	**0.096**	**234**	**52583.5**	**52851.8**	**413.48**	**-0.0124**	**0.2546**	$\mathbf{3.84 \times 10^{-9}}$	**15.4**
±		0.0006	0.011	8	1.3	9.1	0.26	0.0003	0.003	0.14×10^{-9}	

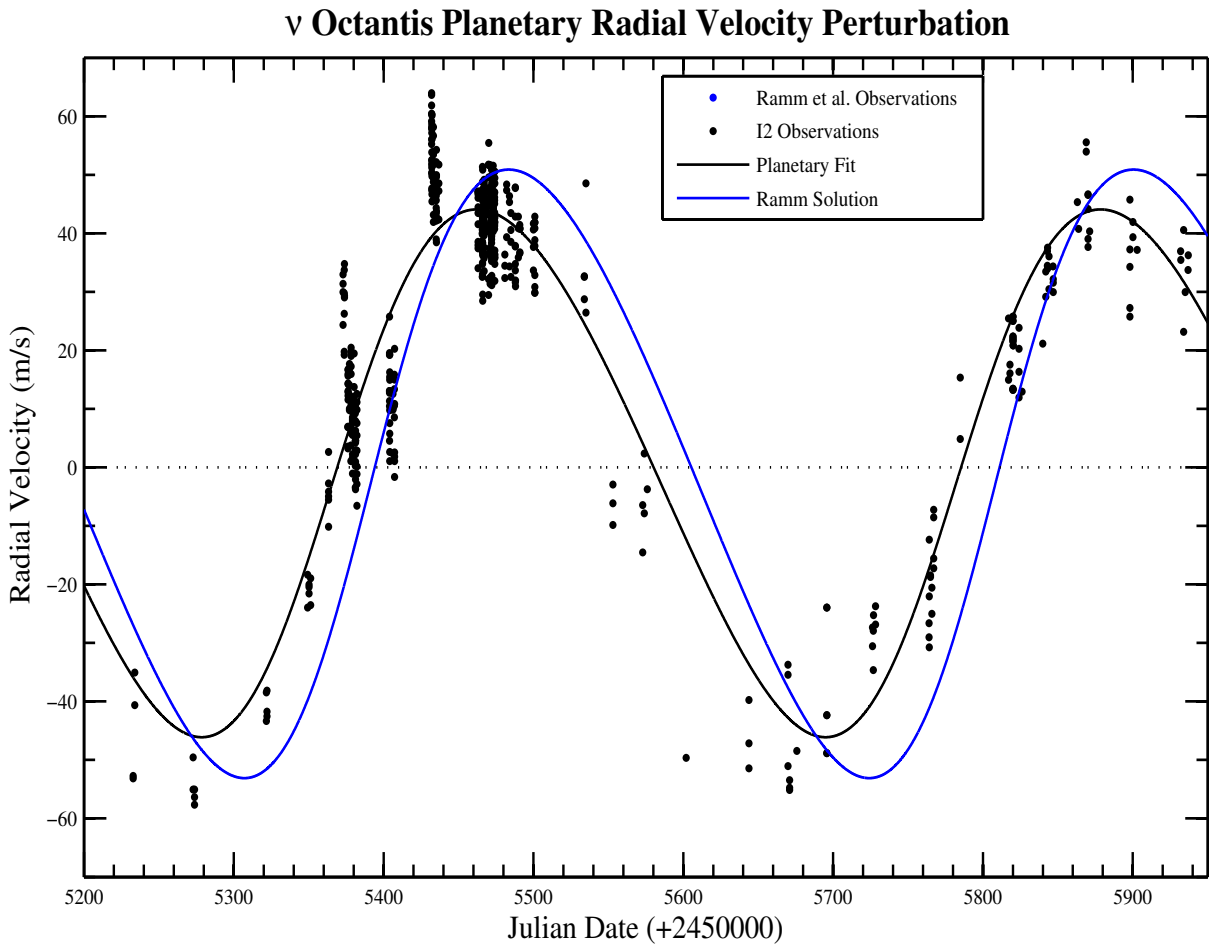

Figure 4.4.3 - *The relative radial velocity observations (dots) reduced in this thesis of the suggested planet orbiting the ν Oct primary star with the corresponding line of best-fit (black solid-line) and the orbital solution derived by Ramm et al. (2009)(blue solid-line).*

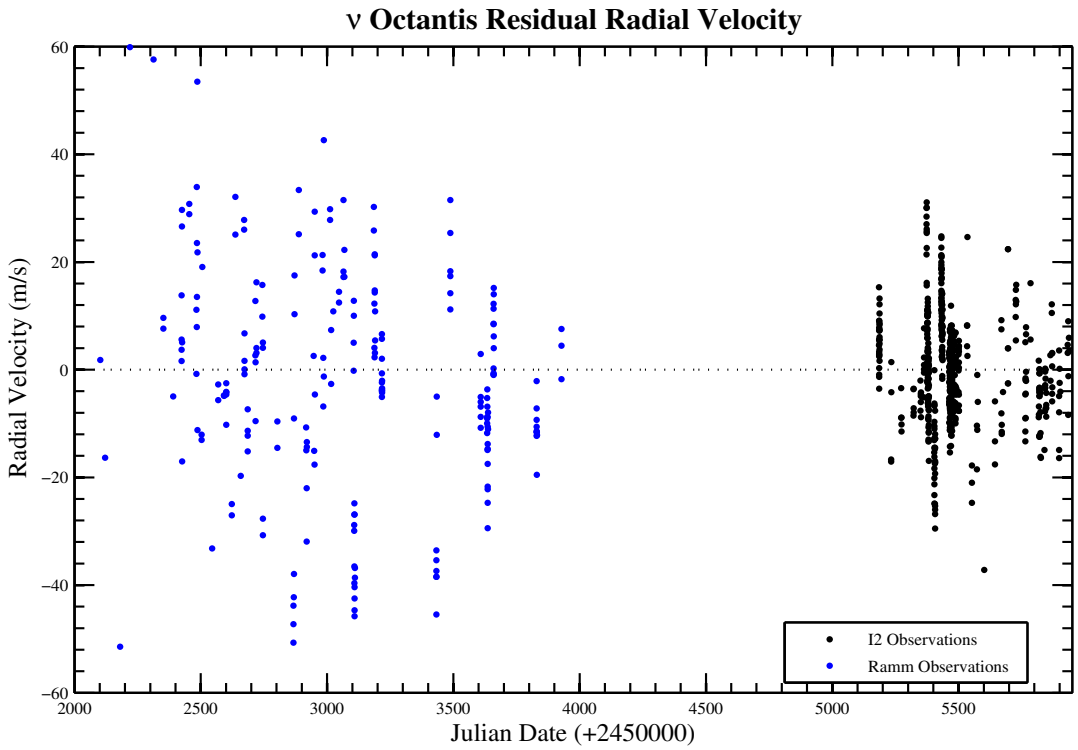

Figure 4.4.4 - *The residual radial velocity for the suggested planet orbiting the ν Oct Primary star, using the combined orbital solution. Note that observations between JD2452068 to JD2453928 were reduced by Ramm et al. (2009).*

The best-fit orbital solution for the binary radial-velocity perturbation, calculated from all 817 observations, gave a period of 1050.04 ± 0.02 days and an eccentricity of 0.2359 ± 0.0001, along with the other four orbital elements shown in the first row of Table 4.4.1, which give a reduced $(\chi^2)^{1/2}$ of 2.8. Figure 4.4.1 also shows the corresponding line of best-fit for these orbital elements. The orbital elements are in close agreement to the Ramm et al. (2009) orbital solution for the binary, but are not within the uncertainties of one another, however, the current values are have much smaller uncertainties. This could be due to the less precise radial velocities used in Ramm et al. (2009) and thus combining them with the more precise data in this thesis has improved the solution.

4.4.2 Analysis of the Suggested Planet's Radial Velocity Perturbation

The best-fit orbital solution for the planetary perturbation using only the current data gave a period of 416.9 ± 2.1 days and an eccentricity of 0.096 ± 0.015 along with the other four orbital elements shown in the third row of Table 4.4.1. The RMS for the fit to the planetary keplerian was 9.6 ms^{-1} with a reduced $(\chi^2)^{1/2}$ of 1.4. Figure 4.4.3 also shows the corresponding line of best-fit for these orbital elements and the orbital solution derived in Ramm et al. (2009). When comparing this result to Ramm et al. (2009), the semi-amplitude is about 5 ms^{-1} smaller and the time of periastron passage is slightly smaller, however, the period, eccentricity, and argument of periapsis are all the same within the uncertainties.

The best-fit orbital solution for the planetary perturbation using only the Ramm et al. (2009) data gave a period of 422.0 ± 4.2 days and an eccentricity of 0.09 ± 0.02 along with the other four orbital elements shown in the fifth row of Table 4.4.1. The RMS for the fit to the planetary keplerian was 23.5 ms^{-1} with a reduced $(\chi^2)^{1/2}$ of 4.6, which is quite a lot larger than the current data alone which may be due to less precise observations that do not use an iodine reference spectrum to remove instrumental effects. This can also be seen visually in the planetary residuals plot, Figure 4.4.4, where the Ramm et al. (2009) is much more scattered than the current radial velocities. This orbital solution is in agreement with Ramm et al. (2009) except for the eccentricity which is somewhat smaller.

The best-fit orbital solution for the planetary perturbation using the combination of both data sets gave the most precise period of 413.48 ± 0.26 days and an eccentricity of 0.096 ± 0.011 along with the other four orbital elements shown in the seventh row of Table 4.4.1. The RMS for the fit to the planetary keplerian was 15.4 ms^{-1} with a reduced $(\chi^2)^{1/2}$ of 2.8. Figure 4.4.2 also shows the corresponding line of best-fit for these orbital elements and the orbital solution derived in Ramm et al. (2009).

From the above analysis one can conclude that the orbital elements have not changed to within the uncertainties between the Ramm et al. (2009) and the current observations and therefore the planetary and binary perturbations have remained stable over the past ten

years. This is strong evidence that this perturbation is caused by a planet and not the result of star spots.

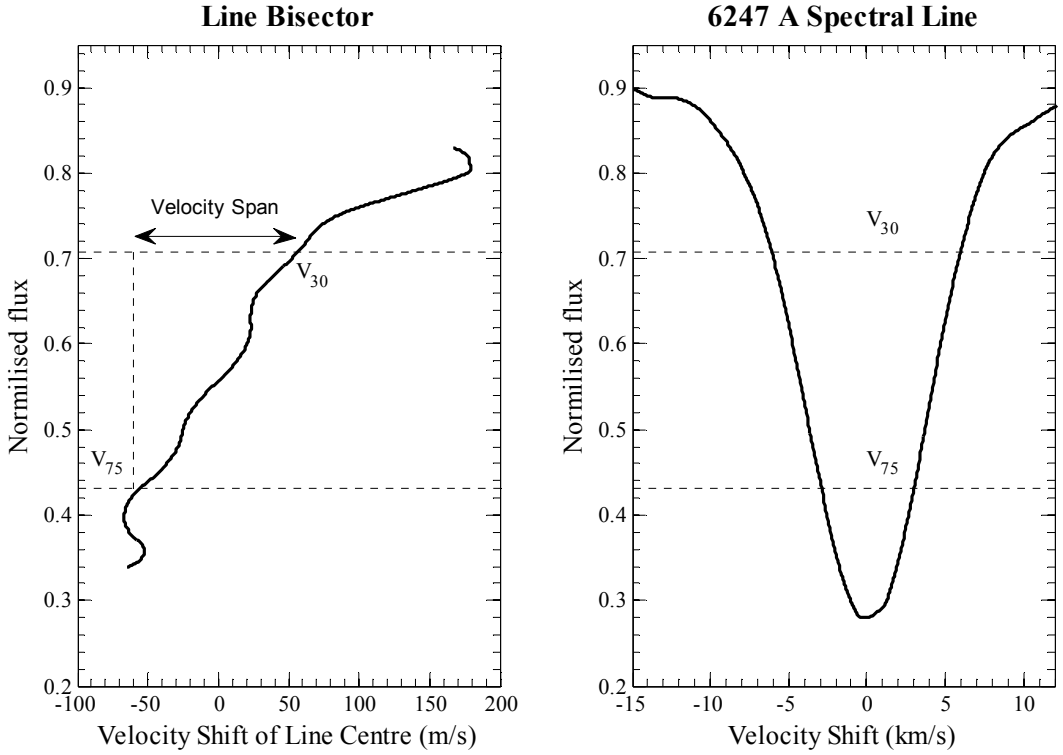

Figure 4.4.5 - *Right: A plot of an example ν Octantis spectral line at 6247 A used in the calculation of the bisectors. Left: The corresponding bisector for the spectral line. Both plots show the 30 percent and 75 percent (dashed line) of the line depth used in the calculation of the velocity span.*

To investigate the possibility of other phenomena causing the radial-velocity perturbation a bisector analysis was performed on the ν Octantis spectral data. This was done with the three spectral lines centred at wavelengths 6109 Å (NiI), 6174 Å (FeI), and 6247 Å (FeI), which were chosen within the recommended region for a K-giant star by Gray (1983) and for the lack of iodine lines in this region. These lines are also shown in Figure 4.4.8. Each side of the spectral lines was interpolated in relation to the opposing red and blue sides, respectively, for both the 75 per cent and 30 per cent of the peak value. The mean wavelength and hence the velocity shift at these two line heights allowed the calculation of the velocity span by the equation $V_{\text{span}} = v_{75} - v_{30}$. Figure 4.4.5 is an example of a line bisector showing both the 75 per cent and 30 per cent of the line depth values.

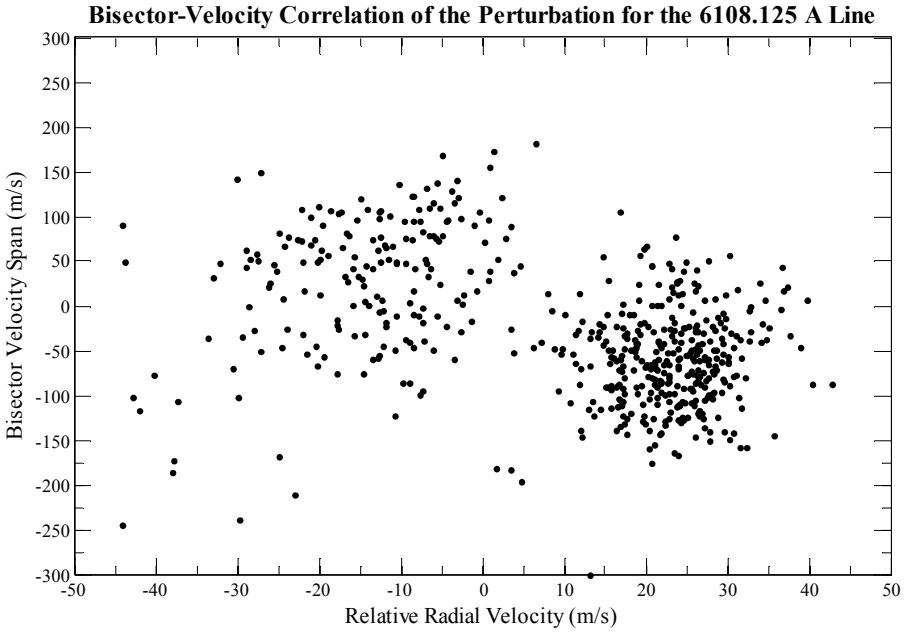

Figure 4.4.6 - *The bisector velocity span as a function of the perturbation velocities for the 6108.125 A spectral line, correlation coefficient of −0.378.*

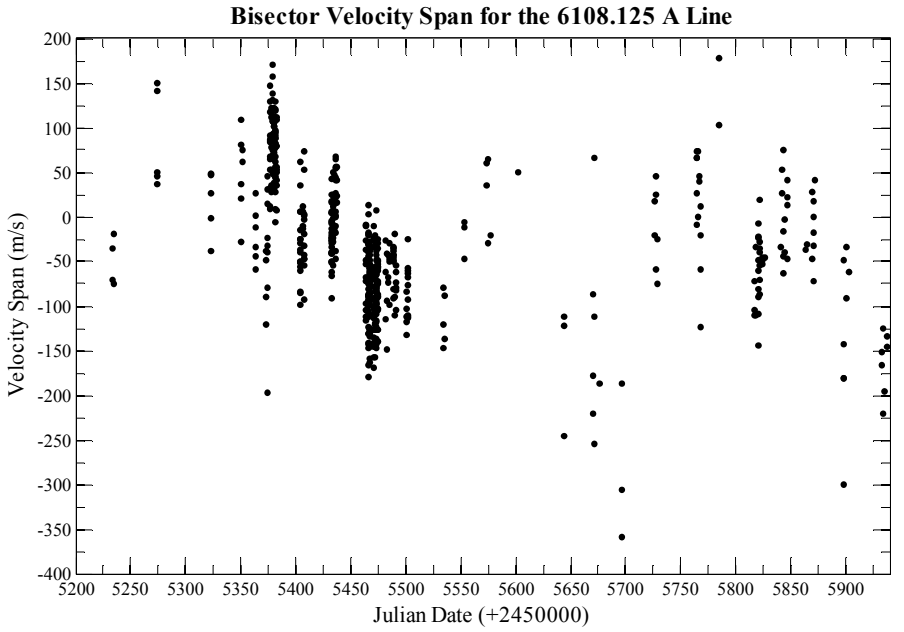

Figure 4.4.7 - *The bisector velocity span as a function of time for the 6108.125 A spectral line.*

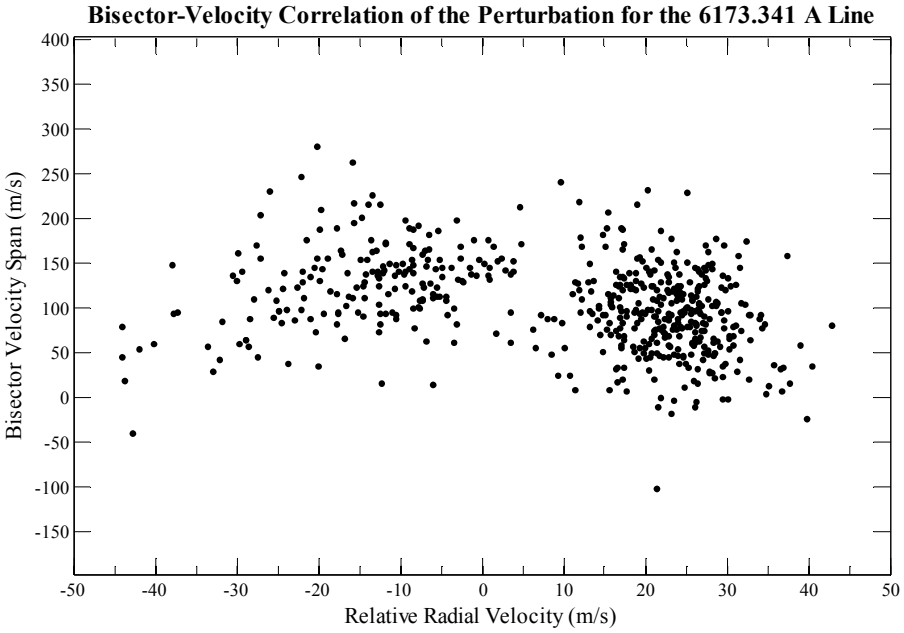

Figure 4.4.8 - *The bisector velocity span as a function of the perturbation velocities for the 6173.341 A spectral line, correlation coefficient of −0.295.*

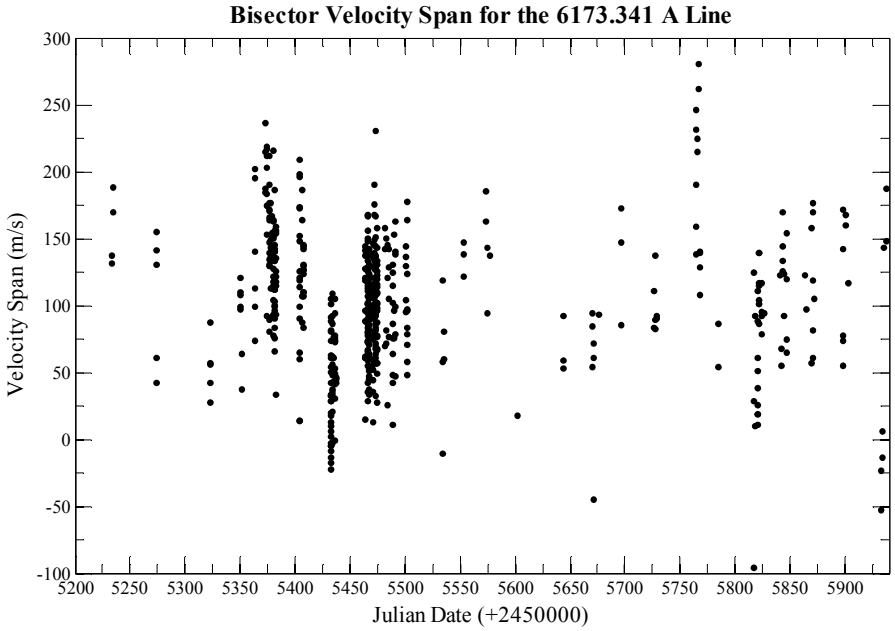

Figure 4.4.9 - *The bisector velocity span as a function of time for the 6173.341 A spectral line..*

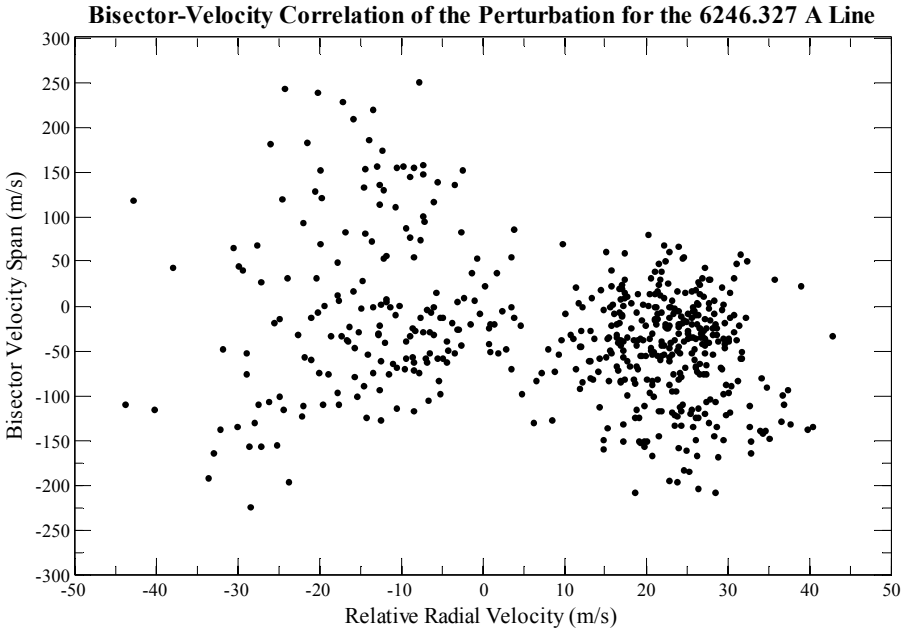

Figure 4.4.10 - *The bisector velocity span as a function of the perturbation velocities for the 6246.327 A spectral line, correlation coefficient of −0.297.*

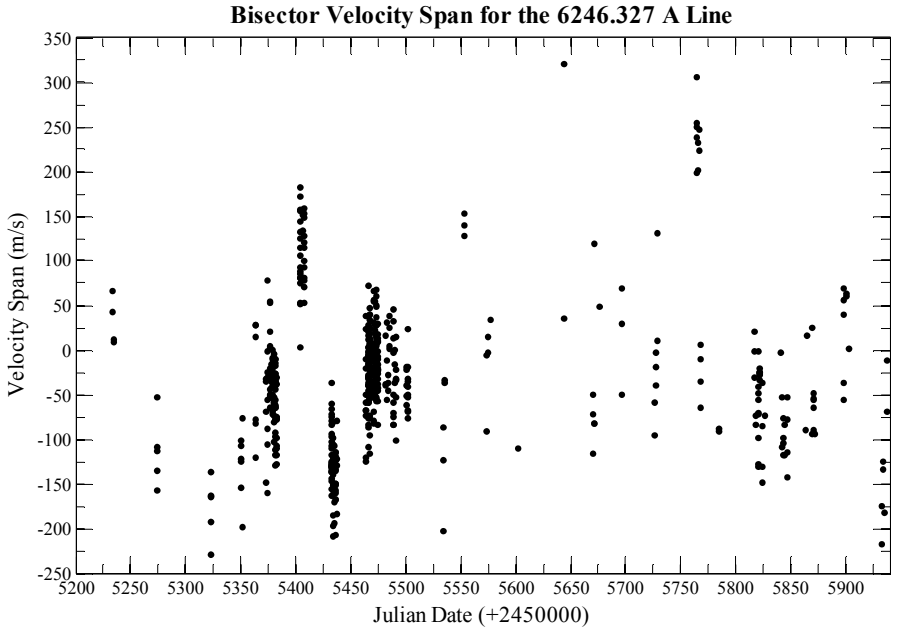

Figure 4.4.11 - *The bisector velocity span as a function of time for the 6246.327 A spectral line..*

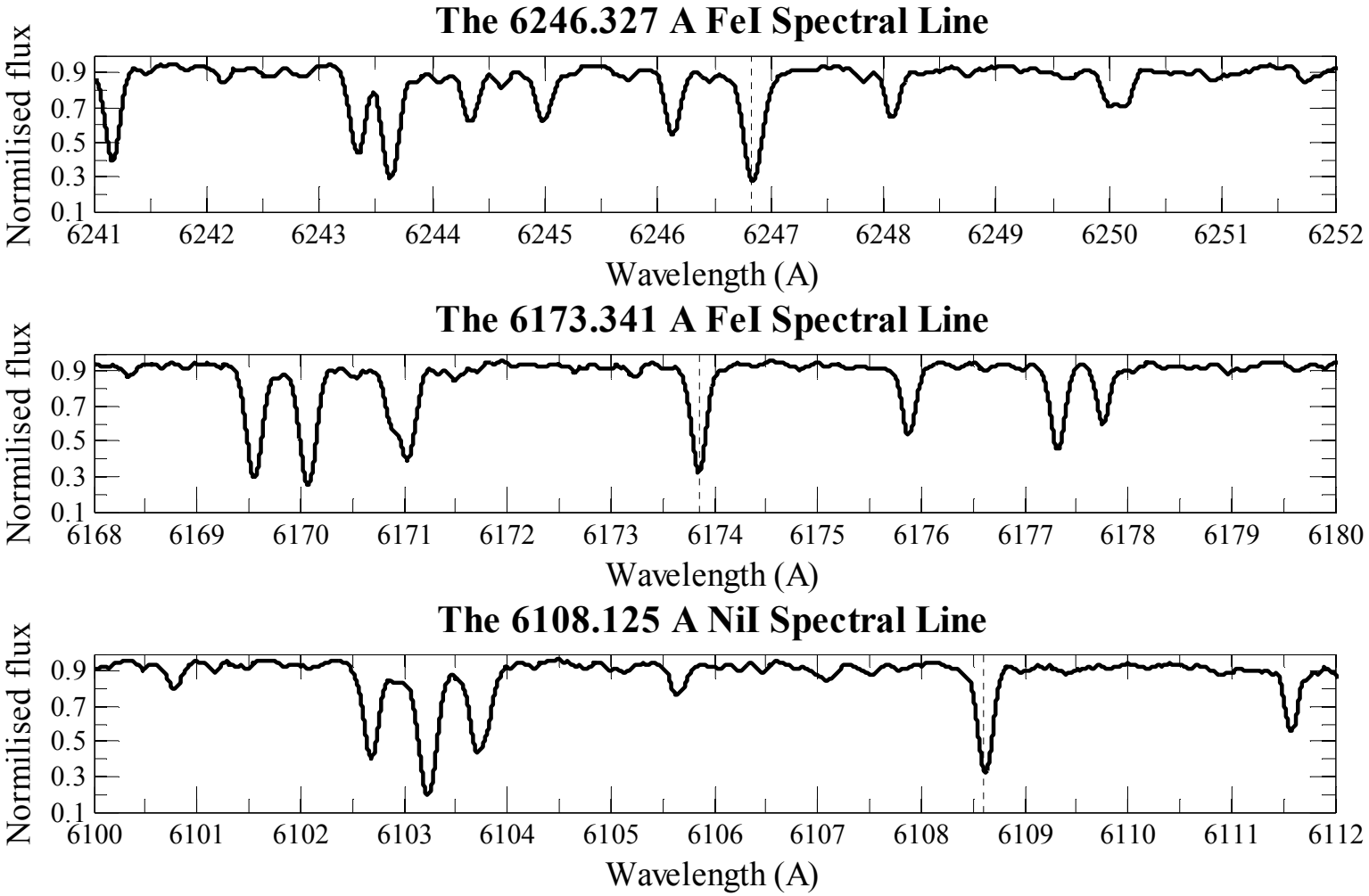

Figure 4.4.12 - *The v Octantis spectral lines used in the bisector analysis. The vertical dashed lines represent the centre of the spectral lines at 6246.327 A (FeI), 6173.341 A (FeI), and 6108.125 A (NiI).*

Figures 4.4.6, 4.4.8, and 4.4.10 are plots of the velocity span as a function of the perturbation radial velocity for each of the spectral lines mentioned, which all show a small anti-correlation with the perturbation. The 6108.125 Å (NiI) line has a correlation coefficient of -0.378, which is considered to be a moderate negative correlation. However, the 6246.327 Å (FeI) and 6173.341 Å (FeI) lines have correlation coefficients of -0.297 and -0.295, respectively, which are considered to be weak negative correlations. It should be noted that the scatter in the velocity span is quite large compared to the uncertainty in the radial-velocity, therefore these weak correlations may only be the result of random error.

One possible explanation for this anti-correlation is that the planet is reflecting light from the primary star in such a way that it contaminates the observed spectrum. Thus, as the planet and primary star orbit their common centre of mass they are always moving in opposite directions and therefore the Doppler shifts are of opposite sign. For example, the observer would see the spectral lines shift as the primary star moves towards and away from the observer due to the orbiting planet, as one would expect. However, the much dimmer reflected light from the planet has a separate Doppler shift of opposite sign which would manifest itself as line asymmetry on the opposite side to the lines Doppler shift direction (i.e. positive radial velocity gives asymmetry at the shorter wavelength side of a spectral line). Thus giving an anti-correlation between the radial velocity and velocity span. For this to even be possible the planet would have to have a very large atmospheric albedo or contain a very larger dust ring similar to Saturn in our Solar system.

The anti-correlation between the velocity span and the radial velocity could also be the result of star spots or pulsations. Assuming the primary star is rotating from left to right in the observers perspective, then a star spot just moving into view would give a negative Doppler shift. The star spot itself decreases the amount of light coming from a specific region of the star, thus appears as a small notch in the spectral lines. In the case of a spot just rotating into view the line asymmetry would appear at a shorter wavelength resulting in a positive velocity span. As the star rotates the spot increases in angular size to a maximum facing directly at the observer, then decreases in angular size as it rotates out of view. However, if this were the case for ν Octantis then we would see a variability in its brightness over time, which we do not. Star spots also do not generally last for a 10-yr period as we see in the observed radial velocity perturbation.

Radial pulsations are the physical expansion and contraction of a stars atmosphere. During the expansion and contraction phases the observer measures a range of Doppler shifts between a maximum at the centre of the stellar disk to zero at the limb. The shifts are, therefore, not true bodily displacements of the normal spectral line, but represent the broadening of the spectral line towards blue wavelengths during expansion and red wavelengths during contraction. This results in line asymmetry on the red side of a spectral line during expansion and for the blue side during contraction. Therefore, a plot of velocity span vs. radial velocity would produce an anti-correlation. However, pulsations also produce noticeable changes in the brightness of a star which is not observed in the ν Octantis primary and so it is very unlikely that this is the case.

Figure 4.4.7, Figure 4.4.9, and Figure 4.4.11 are plots of the velocity span as a function of time, which show there are no periodic variations in line asymmetry. One may conclude from this information that the perturbation is not the result of radial or non-radial pulsations to within the uncertainty of the spectrograph.

Assuming that this perturbation is the result of an orbiting planet one can calculate the mass of the planet via the mass-function f_{M1} with the equation:

$$\frac{q^3}{(1+q)^2} = \frac{f_{\mathrm{M1}}}{M_1 \sin^3 i}, \tag{4.4.3}$$

where $q = M_2/M_1$, and i is the inclination of the system chosen to be 71° (Ramm et al., 2009) assuming the planet is in a coplanar orbit about the primary star. The mass of the planet has been calculated to be $M_{\mathrm{pl}} \sin i = 2.18\ M_{\mathrm{J}}$ or $M_{\mathrm{pl}} = 2.3 \pm 0.4\ M_{\mathrm{J}}$ according to the data reduced in this thesis. The semi-major axis can also be calculated by Kepler's third law to be $a_{\mathrm{pl}} = 1.21 \pm 0.09$ AU.

4.4.3 Comparison to Simulations

It was found in Section 3.2.4 that the eccentricity of the planet orbiting the ν Octantis primary star varies with a period of about 40 years and an amplitude of 0.041, assuming the orbital elements derived from the third row of Table 4.4.1. If the observed perturbation is

indeed a planet orbiting the ν Octantis primary then the eccentricity should vary over time as predicted in the simulations. Figure 4.4.13 is a smoothed, 3-yr moving average, simulation of the eccentricity variations of the planet over an arbitrary 70-yr period, at a time step of half a day. In order to measure the maximum eccentricity variation one can expect between the Ramm et al. (2009) data and the I_2-cell data due to just the 40-year variation a second-order Fourier series was fitted to the simulated data via least-squares, resulting in the solid red-line in Figure 4.4.13.

When one fits a keplerian to a data set and determines the orbital elements, this represents the average of those elements over the observed time interval. In an attempt to compare the maximum eccentricity variation between the two data sets to the observations, the average eccentricity in the simulation, corresponding to the same length of time as the Ramm et al. (2009) (~5 years) and the I_2-cell (~2 years) observations, are calculated separately. In order to determine the maximum eccentricity variation between the two data sets one needs to differentiate the fitted curve to obtain the rate of change of the eccentricity, also shown in Figure 4.4.13. This can then be used to determine when the eccentricity is varying the most, thus by setting this time to be the midpoint between the two data sets and then calculating the difference in the mean eccentricity during the observations separately, one can calculate the maximum eccentricity we may observe if this perturbation is the result of a planet orbiting the ν Octantis primary.

For the Ramm et al. (2009) time interval the average eccentricity is 0.131, while the average eccentricity for the I_2-cell data time interval is 0.180, which were determined using a midpoint time of 41.6 years after the simulation start time. The difference in the eccentricity between the two time intervals is 0.049. The eccentricity of the planet from Ramm et al. (2009) was determined to be 0.123 ± 0.037, while the eccentricity for the I_2-cell data was determined to be 0.096 ± 0.015, which gives a difference of 0.027 ± 0.052. This value is within the maximum eccentricity variation predicted by the simulations and therefore is in agreement with the simulations, but it should be noted that the uncertainties are larger than this difference and so may not be a reliable indication of the eccentricity changing.

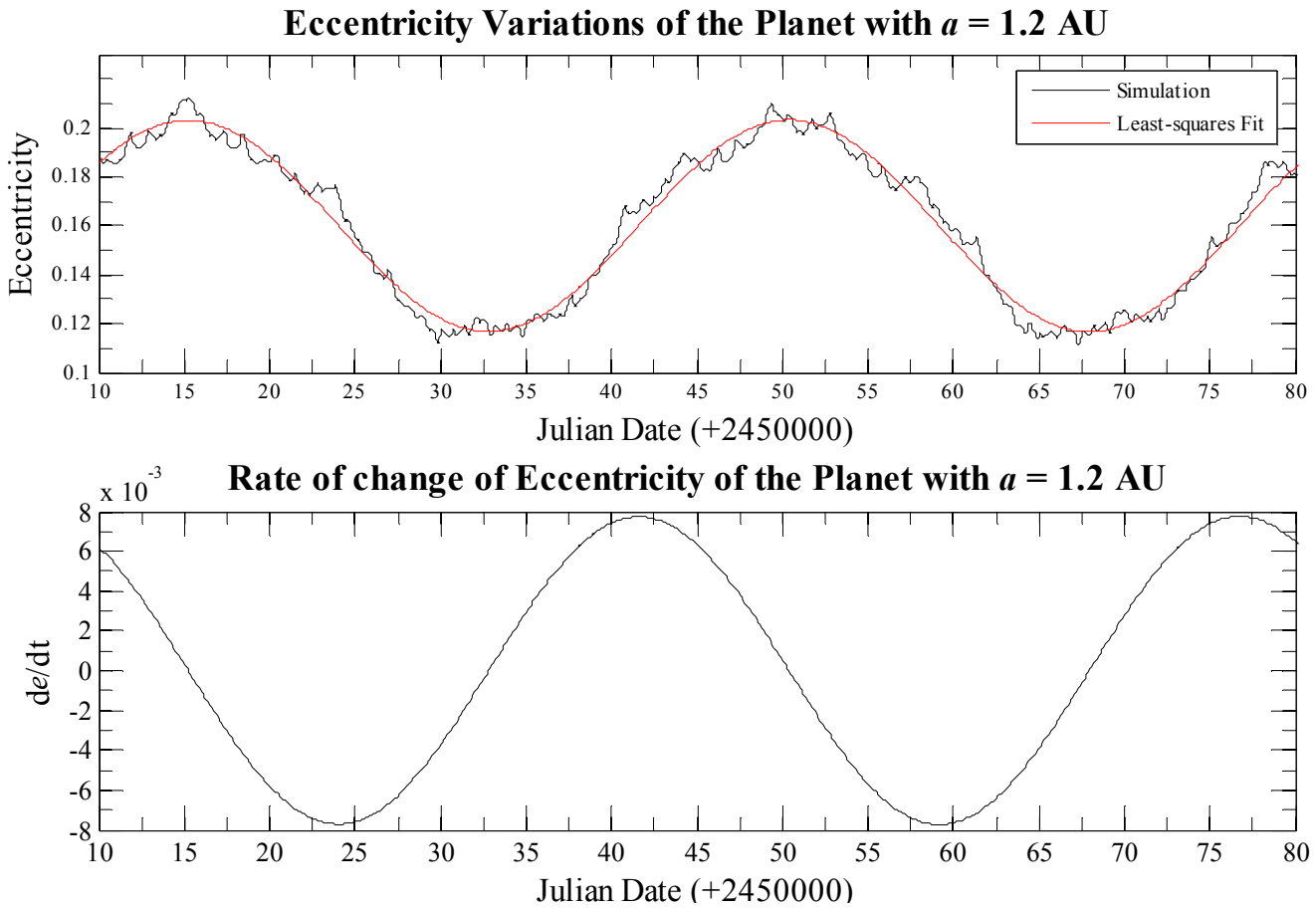

Figure 4.4.13 - *Top: Eccentricity simulation (black-line) of the v Octantis planet with an initial semi-major axis and eccentricity of 1.2 AU and 0.10, respectively, over a period of 70 years. The simulation has also been smoothed with a moving average over the previous 3 years. The red-line is the least-squares fit of the simulation to a 2nd-order Fourier series. Bottom: The derivative of the fitted curve in the Top plot, giving the mean rate of change of the eccentricity, which is used to determine the regions with the largest changes in eccentricity.*

4.5 Conclusion

It was found from 590 spectra imaged on HERCULES at MJUO between January 2009 and January 2012 combined with the Ramm et al. (2009) data that the radial velocity perturbation of the binary has a period of 1050.04 ± 0.02 days and an eccentricity of 0.2359 ± 0.0001 along with the other four orbital elements shown in the first row of Table 4.4.1. The orbital solution for the binary gave a reduced $(\chi^2)^{1/2}$ of 2.8 which corresponds to a good fit and was subtracted from the raw radial velocities to reveal the planetary perturbation.

The keplerian fit for the perturbation using only the data reduced in this thesis gave a period of 416.9 ± 2.1 days and an eccentricity of 0.096 ± 0.015, along with the other four orbital elements shown in the first row of Table 4.4.1, giving an RMS scatter of 9.6 ms^{-1}. A keplerian was also fitted to both the Ramm et al. (2009) data alone and the combination of the two data sets which gave a period of 422.0 ± 4.2 days and 413.48 ± 0.26 days, respectively, with eccentricities of 0.09 ± 0.02 and 0.096 ± 0.011, respectively. These two cases gave an RMS scatter of 23.5 ms^{-1} and 15.4 ms^{-1}, respectively. Overall it was found that the orbital elements were in strong agreement with Ramm et al. (2009) apart from a small change in the semi-amplitude which may be due to the incorporation of the I_2-cell giving a much higher precision in the current radial velocities. Therefore, one can conclude that the radial-velocity perturbation has remained stable for at least ten years, which is strong evidence for the presence of a planet orbiting the ν Octantis primary star. Further evidence to support this claim was found in a bisector analysis of three ν Octantis spectral lines over the observed time interval, which did show a weak anti-correlation between the perturbation's radial velocity and the velocity span of the asymmetries in spectral lines. This may be caused by reflected light from the planet but this is very unlikely when considering its size relative to the primary star. Furthermore, no time varying perturbations were found in the bisectors.

Assuming that the perturbation is indeed a planet, the mass was calculated from the current data to be 2.3 M_J with a semi-major axis of 1.21 ± 0.09 AU. Therefore, one can conclude that this planet is a gas giant similar in composition to Jupiter in our own solar system.

From simulations of the eccentricity for the ν Octantis planet it was found that the maximum eccentricity variation one can expect between the Ramm et al. (2009) and the I_2-cell observations is 0.049. This value just over double that if the observed difference of 0.024 ± 0.052 and so the observation are in agreement with the simulation. This is strong evidence that the perturbation is not the result of pulsations or changes in the primary stars atmosphere which would cause a bad keplerian fit, and hence, the eccentricity difference would be a lot larger. However, the uncertainties are larger than this difference and so this may not be a reliable indication of eccentricity change.

Chapter 5
Conclusion

ν Octantis is a single-lined spectroscopic binary with a period of 1050.11 ± 0.13 days and an eccentricity of 0.23588 ± 0.00028, as measured by Ramm et al. (2009). The mass of the K0III spectral-type primary star was determined to be 1.4 ± 0.3 $M_{\odot}$ by comparing its position on a colour-magnitude diagram to model evolutionary tracks. This, in combination to the Ramm et al. (2009) orbital solution, allowed the calculation of the mass of the secondary as $0.5 \pm 0.1\ M_{\odot}$ which has a semi-major axis of 2.55 ± 0.13 AU, and in turn one can estimate its spectral-type to be between K7 to M1.

In addition to the binary's radial velocity perturbation, Ramm et al. (2009) also detected a second perturbation with a semi-amplitude of 51.8 ± 1.6 ms^{-1} and a period of 417.4 ± 3.8 days, which is close to the 5:2 period ratio with respect to the binary's period. They showed that this perturbation does not depend on wavelength or the asymmetric variations of the spectral lines, that the perturbation was stable for at least the five years that ν Octantis was observed, and that ν Octantis is photometrically stable. This is strong evidence that this

perturbation is the result of a planet orbiting the ν Octantis primary star. However, if one is to assume the planet is in a prograde coplanar orbit then it has a semi-major axis of 1.2 AU, but according to the formula derived by Holman and Wiegert (1999), giving the maximum semi-major axis for a stable orbit in a binary system, stable orbits can only exist within 0.6 AU of the ν Octantis primary, thus contradicting the observed stability.

A possible solution to this problem was suggested by Eberle and Cuntz (2010). They proposed that a retrograde coplanar orbit allows for a greater region of stability about the primary star. They performed 10^4-yr orbital simulations of the planet over a range of primary and secondary star masses pertaining to the observational uncertainties and over a range of initial semi-major axes of 0.561 AU to 1.377 AU, for both prograde and retrograde orbits. It was found that prograde orbits have a stable orbit limit of 0.64 ± 0.01 AU as expected, but the retrograde orbits have a stable orbit limit almost double that of the prograde orbit at 1.22 ± 0.02 AU, resulting in a 60 per cent probability that the Ramm et al. (2009) planet can exist in a retrograde orbit about the ν Octantis primary star. Eberle and Cuntz (2010) also performed a 10^7-yr orbital simulation of the planet in a retrograde orbit and found the planet still remained stable. Further simulations by Quarles et al. (2012), who took a more quantitative approach by measuring the maximum Lyapunov exponent, also found that retrograde orbits give rise to a larger region of stability and that the starting position of the planet in the simulation only slightly affects the long-term stability.

Another solution to the unstable planetary orbit, suggested by Morais and Correia (2012), is that the perturbation is not a planet at all but is the result of the secondary star itself being another close binary system orbiting the ν Octantis primary star. It is thought that the radial-velocity perturbations seen in the observations is the result of both the inner binary's wobble about its own centre of mass and the precession or apsidal-motion of their orbits. By fitting a precessing keplerian orbit to the Ramm et al. (2009) data with a precession rate of -0.86 °/yr they obtained an RMS scatter of 36.3 ms^{-1}, which is a little better than the Ramm et al. (2009) single keplerian fit which had an RMS scatter of 39.1 ms^{-1}. However, when compared to the double keplerian, which assumes an orbiting planet, the RMS scatter was much better at only 19 ms^{-1}. Morais and Correia (2012) also say that in general these triple star systems which have inclinations larger than 45° exhibit periodogram peaks near

period harmonics such as the 5:2 period ratio seen in the observations, and state that this is strong evidence that the perturbation is the result of another close binary.

Assuming this perturbation is the result of another close binary Morais and Correia (2012) estimated the masses of the inner binary to be $M_1 = 0.23\ M_\odot$ and $M_2 = 0.27\ M_\odot$ with a semi-major axis, eccentricity, and inclination of 0.35 AU, 0.76, and 60° respectively.

In Chapter 3 the solution of retrograde planetary orbit stability was investigated by first confirming the instability of the suggested planet's prograde orbit by performing a 3-body simulation via a Bulirsch-Stoer algorithm. It was found that the prograde orbit only survives 12 years before being ejected from the system. However, over the same time interval a simulation of an equivalent retrograde orbit remained very stable. It was also found that in the retrograde case the eccentricity varies periodically with a period of about 40 years.

To investigate the long-term stability of a retrograde orbit a 100 million-year orbital simulation of the suggested planet was performed on the BlueFern super computer at the University of Canterbury. It was found that the maximum distance between the two stars and also between the planet and primary star represented the apoapsis and periapsis of the two orbits, showing that both the secondary and the planet act as if they were in a two-body keplerian system, and therefore it can be assumed that these variations in distance from the primary star are caused by the eccentricity of the corresponding orbits rather than some long term effect. The periodic variation in the eccentricity of 40 years was also found to remain consistent for the 100 million years and could be a connection to the stability of the retrograde orbit.

To gain a greater understanding of why retrograde orbits are stable, possible causes such as mean-motion resonance and an enlarged region of stability were investigated. This was done by performing 10^4-yr orbital simulations over a range of eccentricities, and in turn for each eccentricity a range of nine mass combinations or mass ratios (M_2/M_1) pertaining to the masses of the primary and secondary star, which were all chosen to represent the extrema cases of the observational uncertainties determined in Ramm et al. (2009). For each mass ratio a range of initial semi-major axes between 1.010 and 1.798 AU was chosen with a resolution of 0.004 AU.

In general, it was found that the ν Octantis system consists of an inner stable region where all orbits are stable and an outer unstable region where the majority of orbits are unstable. The cut-off point for stable orbits depended largely on the mass of the primary, in that a larger mass gives a larger stable orbital region, while the secondary mass and planetary eccentricity only affect it a little. The stability of planets in the 'outer region' (semi-major axes, on average, larger than 1.315 AU) appears to depend on the mass of the secondary and the planetary eccentricity, whereby a larger secondary mass or eccentricity gives rise to more unstable orbits. The mean stable orbit limit for a 2.5 M_J planet was determined to be $a = 1.315 \pm 0.092$ AU which is in agreement with the findings of Eberle and Cuntz (2010) and encompasses the orbit of the suggested ν Octantis planet.

The orbit of the suggested planet is said to be in a 5:2 mean-motion resonance with the secondary star and so in order to investigate the other mean-motion resonances a plot representing the fraction of stable orbits for a range of period ratios was calculated from the simulations of different mass ratios and eccentricities within the observational uncertainties. It was found that the suggested planet has a probability of 80 per cent at surviving 10^4 years while the 3:1 resonance has a 100 per cent probability. However, other mean-motion resonance such as 2:1, 7:4, and 3:2 have less than a 30 per cent probability of surviving the entire integration and so are considered not to exist in reality. Thus the most likely case is that retrograde orbits give larger regions of orbital stability and that resonance is not a key factor in the stability of the suggested planet.

It was found in the long-term retrograde orbit simulation of the suggested planet that the eccentricity has a dominant time variation with a period of about 40 years which remained constant for the 100 million year time span. This inspired further investigation to determine if there is any connection between the stability of retrograde orbits and the variation in the eccentricity. It was found that the period of the dominant eccentricity variation depends on the semi-major axis by a second order exponential relationship, where the larger the semi-major axis the smaller the eccentricity period. It was also found that the relationship for prograde orbits tends to have much smaller eccentricity periods when compared to the retrograde orbits and also decreases at a slightly greater rate with increasing semi-major axis. The eccentricity period for the stable orbit limit of both the prograde and retrograde orbits were both found to be approximately 38.48 years, which suggested that there is a hard limit

for how frequently the shape of the planet's orbit can change, and therefore one can conclude that prograde orbits are gravitationally perturbed more frequently by the secondary star than when the planet is in a equivalent retrograde orbit.

The Fourier analysis of the eccentricities over time for each semi-major axis used in Section 3.2.4 showed that the smaller eccentricity variations corresponded mainly to the period of the secondary star and the synodic period of each case.

In Section 3.2.4 non-coplanar orbits were investigated to learn more about the characteristics of the ν Octantis system. It was found that in addition to the coplanar retrograde orbit at an inclination of 180° for the suggested planet, inclinations between about 165° to 190° allow for stable orbits to exist and therefore the planet could very well have an inclination within this range.

In order to see if the suggested planet's radial-velocity perturbation is still present, spectroscopic observations of the ν Octantis primary star were obtained between January 2009 and January 2012. From these 590 observations, when combined with the Ramm et al. (2009) data, we found that the radial-velocity perturbation, as a result of the secondary star, has a best fit orbital solution with a period of 1050.04 ± 0.02 days and an eccentricity of 0.2359 ± 0.0001 along with the other four orbital elements shown in the first row of Table 4.4.1. The orbital solution for the binary gave a reduced $(\chi^2)^{1/2}$ of 2.8 which corresponds to a good fit.

Once the binary orbital solution was subtracted from the raw radial-velocities it revealed the second perturbation thought to be the result of an orbiting planet. The keplerian fit for the perturbation using only the data reduced in this thesis gave a period of 416.9 ± 2.1 days and an eccentricity of 0.096 ± 0.015, along with the other four orbital elements shown in the first row of Table 4.4.1, giving an RMS scatter of 9.6 ms^{-1}. A keplerian was also fitted to the combination of the current data and the Ramm et al. (2009) data giving a period of 413.48 ± 0.26 days and an eccentricity of 0.096 ± 0.011. This gave an RMS scatter of 15.4 ms^{-1} which is a little larger than the fit for the current data alone. Overall it was found that the orbital elements were in strong agreement with Ramm et al. (2009) apart from a small change in the semi-amplitude which may be due to the incorporation of the I_2-cell giving a much higher precision in the current radial velocities. Therefore, one can conclude that the

radial-velocity perturbation has remained stable for at least ten years, which is strong evidence for the presence of a planet orbiting the ν Octantis primary star. Further evidence to support this claim was found in a bisector analysis of three ν Octantis spectral lines over the observed time interval, which did show a weak anti-correlation between the perturbation's radial velocity and the velocity span of the asymmetries in spectral lines. This may be caused by reflected light from the planet but is very unlikely when considering its size relative to the primary star.

Assuming that the perturbation is indeed a planet, the mass was calculated from the current data to be 2.3 M_J with a semi-major axis of 1.21 ± 0.09 AU. Therefore, one can conclude that this planet is a gas giant similar in composition to Jupiter in our own solar system.

From simulations of the eccentricity for the ν Octantis planet it was found that the maximum eccentricity variation one can expect between the Ramm et al. (2009) and the I_2-cell observations is 0.049. This value is just over double that of the observed difference of 0.024 ± 0.052 and so the observations are in agreement with the simulation. This is strong evidence that the perturbation is not the result of pulsations or changes in the primary star's atmosphere which would cause a bad keplerian fit, and hence, the eccentricity difference would be a lot larger. However, the uncertainties are larger than this difference and so this may not be a reliable indication of eccentricity change.

Overall, it was found in Chapter 3 that retrograde orbits have stable regions about the ν Octantis primary star that are almost double that of prograde orbits, and that the suggested planet could potentially survive for at least 100 million years in a retrograde coplanar orbit. It was also found that the variation in the eccentricity with time may be connected to the stability of planetary orbits in that prograde motion gives rise to more rapid variations than retrograde motion with the same semi-major axis. In Chapter 4 spectroscopic observations of the ν Octantis, and hence radial velocities, were used to show that the planetary perturbation is still present and that the orbital elements remain unchanged within the uncertainties. Further evidence from line bisector analysis showed there was no dependence of the perturbation on spectral line asymmetries. Therefore, one can conclude that this perturbation is most likely the result of a 2.3 M_J planet orbiting the primary star which is supported both theoretically and observationally. However, further observation is needed using the

I_2-cell for multiple binary orbits to obtain more precise orbital solutions for both the binary and planet.

Appendix

Table 5.1 - *Dates, weighted mean relative radial velocities, and the corresponding errors from 590 MJUO observations for ν Octantis.*

Julian Date 245...	RV (km/s)	Error (m/s)	Julian Date 245...	RV (km/s)	Error (m/s)	Julian Date 245...	RV (km/s)	Error (m/s)
5184.9054	25.8056	6.3	5272.8773	21.5409	5.5	5376.1889	15.0653	6.1
5184.9141	25.7948	6.2	5273.8310	21.4757	6.2	5376.1963	15.0609	6.3
5185.8782	25.7754	5.5	5273.8354	21.4768	5.9	5376.2037	15.0612	6.6
5185.8856	25.7727	5.7	5273.8418	21.4738	5.9	5376.2111	15.0642	6.8
5185.8934	25.7625	5.8	5321.7746	18.1990	6.4	5376.2185	15.0713	6.3
5185.9009	25.7639	5.8	5321.7910	18.1925	6.5	5376.2259	15.0722	6.5
5185.9083	25.7683	5.7	5322.1512	18.1736	6.8	5376.2333	15.0725	6.4
5185.9169	25.7639	5.7	5322.1578	18.1697	6.4	5376.2408	15.0705	6.5
5185.9252	25.7647	5.7	5322.1610	18.1686	6.3	5376.2482	15.0718	6.5
5185.9327	25.7674	5.9	5349.2513	16.4783	7.3	5376.2556	15.0679	6.7
5185.9401	25.7701	5.5	5349.2587	16.4721	9.3	5376.2659	15.0659	6.1
5185.9485	25.7717	5.3	5350.2378	16.4183	6.6	5376.2733	15.0667	6.3
5185.9571	25.7728	5.5	5350.2452	16.4175	6.5	5376.2807	15.0661	6.4
5185.9648	25.7669	5.7	5350.2526	16.4161	6.6	5376.2881	15.0699	6.6
5185.9727	25.7689	5.7	5351.2750	16.3594	6.3	5377.2548	15.0243	6.8
5185.9801	25.7656	5.6	5351.2824	16.3538	6.7	5377.2622	15.0252	6.7
5185.9884	25.7659	5.9	5363.2443	15.7071	7.0	5377.2696	15.0213	6.7
5186.8820	25.7521	5.8	5363.2517	15.7078	6.8	5377.2770	15.0188	6.9
5186.8860	25.7534	5.9	5363.2591	15.7125	6.5	5377.2845	15.0157	6.8
5186.8900	25.7481	5.8	5363.2665	15.7048	6.7	5377.2919	15.0159	6.5
5186.8940	25.7502	5.5	5363.2739	15.7043	6.5	5378.2240	14.9664	6.4
5186.8980	25.7448	6.0	5363.2806	15.6994	6.4	5378.2302	14.9632	6.0
5186.9024	25.7481	6.3	5372.8998	15.2505	7.5	5378.2362	14.9676	6.5
5186.9065	25.7434	6.0	5372.9072	15.2483	8.1	5378.2422	14.9721	6.3
5186.9106	25.7439	6.2	5372.9199	15.2458	7.7	5378.2482	14.9770	6.5
5186.9174	25.7452	5.8	5372.9286	15.2397	7.6	5378.2542	14.9784	6.4
5186.9249	25.7458	6.0	5373.7555	15.1948	7.8	5378.2603	14.9806	6.5
5186.9325	25.7462	5.5	5373.7664	15.1941	7.8	5378.2663	14.9800	6.7
5186.9406	25.7401	5.7	5373.7767	15.2044	7.1	5378.2723	14.9790	6.3
5232.8696	23.9307	5.6	5373.7870	15.2004	7.2	5378.2783	14.9710	6.7
5232.8781	23.9314	5.4	5373.7961	15.2072	7.8	5378.2844	14.9691	6.3
5233.8561	23.8926	5.0	5373.8029	15.2024	7.8	5378.2904	14.9648	6.2
5233.8687	23.8980	5.4	5373.8097	15.2024	7.9	5378.2964	14.9656	6.5
5272.8696	21.5466	5.5	5373.8164	15.2073	7.6	5379.1795	14.9186	6.2

Julian Date 245...	RV (km/s)	Error (m/s)	Julian Date 245...	RV (km/s)	Error (m/s)	Julian Date 245...	RV (km/s)	Error (m/s)
5379.1870	14.9230	6.2	5382.2151	14.7726	6.0	5407.2940	13.8170	7.1
5379.1944	14.9288	6.4	5382.2225	14.7777	6.4	5432.0503	13.1528	6.0
5379.2018	14.9282	6.1	5382.2308	14.7787	6.4	5432.0577	13.1583	6.6
5379.2092	14.9247	6.3	5382.2382	14.7865	6.2	5432.0651	13.1610	6.7
5379.2171	14.9240	6.1	5382.2456	14.7883	5.9	5432.0725	13.1586	6.5
5379.2245	14.9237	6.2	5382.2530	14.7887	6.3	5432.0799	13.1613	6.5
5379.2319	14.9166	6.2	5382.2605	14.7899	6.3	5432.0873	13.1555	6.5
5379.2393	14.9143	6.2	5403.8894	13.9240	7.5	5432.0948	13.1468	6.4
5379.2467	14.9172	6.1	5403.8969	13.9257	7.3	5432.1022	13.1489	6.6
5380.1889	14.8770	6.3	5403.9043	13.9258	6.9	5432.1096	13.1435	6.4
5380.1963	14.8801	6.2	5403.9117	13.9319	6.8	5432.1170	13.1501	6.2
5380.2037	14.8813	6.3	5403.9191	13.9321	7.1	5432.1244	13.1525	6.7
5380.2111	14.8812	5.9	5403.9265	13.9383	6.9	5432.1318	13.1543	6.5
5380.2185	14.8799	6.1	5403.9339	13.9252	8.4	5432.1392	13.1561	6.4
5380.2275	14.8796	6.4	5403.9413	13.9232	7.5	5432.1466	13.1484	6.7
5380.2349	14.8786	6.1	5403.9487	13.9159	7.2	5432.1541	13.1542	6.6
5380.2423	14.8814	6.3	5404.0323	13.9163	6.9	5432.1615	13.1530	6.6
5380.2497	14.8878	6.1	5404.0397	13.9137	7.2	5432.1689	13.1515	6.6
5380.2571	14.8818	6.4	5404.0471	13.9088	7.2	5432.1763	13.1445	6.7
5381.1304	14.8245	6.4	5404.0545	13.9240	7.8	5432.1837	13.1424	6.5
5381.1378	14.8266	6.5	5404.0663	13.9099	7.8	5432.2006	13.1460	6.5
5381.1452	14.8282	6.1	5404.0737	13.9217	7.0	5432.2081	13.1522	6.7
5381.1526	14.8317	6.3	5404.0811	13.9256	7.5	5432.2155	13.1506	6.4
5381.1600	14.8348	6.1	5404.0885	13.9218	7.4	5432.2229	13.1447	6.4
5381.1674	14.8355	6.0	5404.0960	13.9164	7.3	5432.2303	13.1390	6.3
5381.1748	14.8369	5.9	5406.2641	13.8435	6.7	5432.2377	13.1404	6.6
5381.1823	14.8344	6.3	5406.2728	13.8411	6.9	5432.2451	13.1427	6.8
5381.1897	14.8325	6.2	5406.2802	13.8405	7.0	5432.2525	13.1452	6.3
5381.1971	14.8302	5.9	5406.2876	13.8333	7.0	5432.2599	13.1534	6.7
5381.2051	14.8259	6.2	5407.2125	13.8096	7.7	5433.1786	13.1296	6.9
5381.2125	14.8209	6.3	5407.2199	13.8145	7.3	5433.1860	13.1240	6.4
5381.2199	14.8290	6.4	5407.2273	13.8144	7.2	5433.1934	13.1248	6.6
5381.2273	14.8266	6.2	5407.2347	13.8125	7.2	5433.2009	13.1281	6.4
5381.2347	14.8283	6.3	5407.2421	13.8068	7.7	5433.2083	13.1199	6.5
5381.2634	14.8271	6.2	5407.2496	13.8005	7.7	5433.2157	13.1134	6.5
5381.2708	14.8197	6.2	5407.2570	13.7987	7.3	5433.2231	13.1145	6.2
5381.2783	14.8238	6.1	5407.2644	13.7959	7.2	5433.2305	13.1183	6.4
5382.1929	14.7864	6.4	5407.2718	13.8002	7.5	5433.2379	13.1196	6.7
5382.2003	14.7835	6.1	5407.2792	13.8077	7.0	5433.2453	13.1237	6.7
5382.2077	14.7773	5.8	5407.2866	13.8123	7.4	5433.2527	13.1224	6.9

Julian Date 245...	RV (km/s)	Error (m/s)	Julian Date 245...	RV (km/s)	Error (m/s)	Julian Date 245...	RV (km/s)	Error (m/s)
5433.2601	13.1236	6.3	5465.8848	12.5742	6.4	5466.2067	12.5718	6.6
5435.1123	13.0814	6.6	5465.8923	12.5737	6.9	5466.2141	12.5713	6.5
5435.1197	13.0769	6.7	5465.8997	12.5669	6.8	5467.0060	12.5644	6.3
5435.1271	13.0751	6.6	5465.9103	12.5671	6.8	5467.0134	12.5674	6.4
5435.1345	13.0738	6.4	5465.9251	12.5707	6.4	5467.0208	12.5638	6.3
5435.1419	13.0710	6.3	5465.9325	12.5699	6.6	5467.0283	12.5644	6.6
5435.1494	13.0671	6.2	5465.9399	12.5716	6.7	5467.0357	12.5649	6.2
5435.1568	13.0702	6.5	5465.9473	12.5779	6.6	5467.0431	12.5510	6.3
5435.1642	13.0721	6.6	5465.9548	12.5717	6.8	5467.0505	12.5551	7.0
5435.1716	13.0714	6.6	5465.9622	12.5665	6.8	5467.0579	12.5565	6.4
5435.1790	13.0773	6.3	5465.9696	12.5668	6.9	5467.0653	12.5532	6.0
5435.1864	13.0773	6.6	5465.9770	12.5615	7.1	5467.0727	12.5602	6.1
5435.1938	13.0769	6.7	5465.9956	12.5706	6.2	5467.0819	12.5660	6.3
5435.2012	13.0745	6.3	5466.0030	12.5800	6.6	5467.0893	12.5595	6.5
5435.2087	13.0691	6.6	5466.0104	12.5757	6.6	5467.0968	12.5604	6.2
5435.2161	13.0651	6.8	5466.0178	12.5745	6.5	5467.1042	12.5595	6.5
5435.2309	13.0698	6.6	5466.0252	12.5660	6.7	5467.1116	12.5587	6.2
5435.2383	13.0733	6.4	5466.0326	12.5608	6.7	5467.1190	12.5610	6.3
5435.2457	13.0740	6.7	5466.0400	12.5630	7.4	5467.1264	12.5608	6.2
5435.2531	13.0798	6.4	5466.0474	12.5649	6.9	5467.1338	12.5650	6.2
5436.8788	13.0383	7.1	5466.0548	12.5626	6.5	5467.1412	12.5644	6.3
5436.8870	13.0334	6.4	5466.0623	12.5743	6.8	5467.1486	12.5623	6.2
5436.8967	13.0387	6.5	5466.0716	12.5698	6.3	5467.1578	12.5641	6.7
5436.9051	13.0415	6.6	5466.0790	12.5649	6.8	5467.1652	12.5608	6.5
5462.9775	12.6102	6.7	5466.0864	12.5723	6.5	5467.1726	12.5582	6.6
5462.9923	12.6097	6.5	5466.0938	12.5656	7.0	5467.1800	12.5589	7.0
5463.0153	12.6062	7.0	5466.1012	12.5559	6.8	5467.1874	12.5602	7.1
5463.0227	12.6013	6.6	5466.1086	12.5570	6.5	5467.1948	12.5566	6.7
5463.0301	12.6094	6.1	5466.1160	12.5641	6.5	5469.9892	12.5195	7.1
5463.0538	12.6000	7.1	5466.1234	12.5711	6.5	5469.9980	12.5288	7.2
5463.0612	12.6083	6.9	5466.1309	12.5686	6.2	5470.0069	12.5279	6.9
5463.0686	12.5958	8.8	5466.1383	12.5782	6.6	5470.0157	12.5174	7.2
5463.0958	12.6064	7.2	5466.1474	12.5741	6.9	5470.0245	12.5241	6.6
5463.1032	12.5991	7.0	5466.1548	12.5668	7.0	5470.0333	12.5315	6.9
5463.1107	12.6034	8.2	5466.1623	12.5671	6.7	5470.0421	12.5387	7.1
5465.8330	12.5628	7.1	5466.1697	12.5676	7.1	5470.0510	12.5385	7.0
5465.8404	12.5684	7.1	5466.1771	12.5627	6.9	5470.0598	12.5317	7.0
5465.8478	12.5693	6.5	5466.1845	12.5681	7.3	5470.0827	12.5337	7.1
5465.8626	12.5702	6.7	5466.1919	12.5736	7.8	5470.1003	12.5304	8.1
5465.8774	12.5697	6.6	5466.1993	12.5678	6.2	5470.1253	12.5419	7.2

Julian Date 245...	RV (km/s)	Error (m/s)	Julian Date 245...	RV (km/s)	Error (m/s)	Julian Date 245...	RV (km/s)	Error (m/s)
5470.1342	12.5363	7.0	5473.0477	12.5057	6.2	5474.1765	12.4862	6.4
5470.1518	12.5340	7.2	5473.0551	12.5046	6.5	5474.1840	12.4850	6.7
5470.1607	12.5315	7.2	5473.0625	12.5019	6.7	5474.1914	12.4824	6.9
5471.0607	12.5142	6.4	5473.0699	12.5037	6.6	5474.1988	12.4859	6.6
5471.0695	12.5092	6.5	5473.0773	12.5003	6.4	5474.2062	12.4916	6.0
5471.0783	12.5102	6.7	5473.0847	12.5060	6.6	5474.2136	12.4871	6.5
5471.0871	12.5151	6.4	5473.0921	12.5109	6.4	5480.9470	12.4328	6.1
5471.0959	12.5294	7.5	5473.1017	12.5062	6.5	5480.9544	12.4372	6.3
5472.0061	12.5079	6.3	5473.1092	12.5046	6.6	5480.9618	12.4347	6.6
5472.0135	12.5149	6.4	5473.1166	12.5007	6.1	5482.0786	12.4330	6.4
5472.0209	12.5145	6.5	5473.1240	12.5023	6.7	5482.0861	12.4414	6.3
5472.0283	12.5110	6.6	5473.1314	12.5026	6.3	5482.0936	12.4418	7.0
5472.0357	12.5094	6.0	5473.1388	12.5010	6.5	5483.9979	12.4169	6.6
5472.0431	12.5038	6.4	5473.1462	12.5090	6.8	5484.0021	12.4279	6.5
5472.0506	12.5056	6.6	5473.1536	12.5061	6.8	5484.0064	12.4292	6.8
5472.0580	12.5068	6.4	5473.1610	12.5063	6.8	5484.9606	12.4208	6.5
5472.0654	12.5084	6.4	5473.1685	12.5031	6.8	5484.9680	12.4103	6.4
5472.0728	12.5088	6.3	5473.1759	12.5073	6.9	5484.9754	12.4178	6.4
5472.0819	12.5107	6.1	5473.1833	12.5045	7.0	5484.9828	12.4162	6.9
5472.0893	12.5079	6.2	5473.1907	12.5029	6.9	5487.9081	12.3970	6.8
5472.0967	12.5154	6.5	5473.1981	12.5050	7.0	5487.9155	12.3951	6.9
5472.1041	12.5175	6.6	5473.2055	12.5022	7.2	5487.9229	12.3985	6.6
5472.1116	12.5192	6.7	5474.0337	12.4926	6.3	5487.9303	12.4013	6.3
5472.1190	12.5142	6.4	5474.0412	12.4953	6.4	5487.9378	12.4105	6.5
5472.1264	12.5096	6.8	5474.0486	12.4974	6.5	5487.9452	12.4111	6.4
5472.1338	12.5041	6.5	5474.0560	12.4916	6.6	5487.9526	12.4064	6.7
5472.1412	12.4987	6.3	5474.0708	12.4935	6.5	5487.9600	12.4006	6.6
5472.1577	12.5087	6.4	5474.0782	12.4931	6.2	5487.9674	12.3949	6.7
5472.1652	12.5125	6.5	5474.0856	12.4982	6.5	5487.9749	12.3935	6.7
5472.1726	12.5134	6.7	5474.0930	12.4957	6.4	5489.8856	12.3957	6.7
5472.1800	12.5140	6.8	5474.1004	12.4978	6.4	5489.8940	12.3983	6.3
5472.1874	12.5156	6.5	5474.1079	12.4965	6.3	5489.9021	12.3906	6.6
5472.1948	12.5097	6.4	5474.1153	12.4936	6.3	5490.8684	12.3934	6.5
5472.2022	12.5028	6.2	5474.1227	12.4921	6.5	5490.8759	12.3883	6.3
5472.2096	12.5003	6.8	5474.1301	12.4870	6.4	5490.8833	12.3875	6.5
5473.0106	12.5022	6.7	5474.1375	12.4866	6.3	5490.9400	12.3877	6.6
5473.0180	12.5054	6.2	5474.1469	12.4997	6.5	5490.9474	12.3924	6.6
5473.0254	12.5087	6.3	5474.1543	12.5009	6.5	5490.9548	12.3920	6.4
5473.0328	12.5088	6.4	5474.1617	12.4990	6.7	5499.9280	12.3697	6.5
5473.0403	12.5019	6.3	5474.1691	12.4932	6.7	5499.9354	12.3706	6.2

Julian Date 245...	RV (km/s)	Error (m/s)	Julian Date 245...	RV (km/s)	Error (m/s)	Julian Date 245...	RV (km/s)	Error (m/s)
5499.9428	12.3706	6.7	5695.8075	14.9356	8.3	5820.0723	18.0074	7.4
5499.9502	12.3672	6.2	5695.8274	14.9179	7.7	5820.0985	18.0157	6.8
5499.9576	12.3630	6.2	5695.8495	14.9123	8.7	5820.1066	18.0166	6.9
5500.9137	12.3672	6.5	5726.2427	15.6208	6.3	5820.1165	18.0197	7.2
5500.9211	12.3702	6.1	5726.2739	15.6255	6.2	5820.1247	18.0164	7.2
5500.9285	12.3710	6.2	5726.8869	15.6322	6.3	5824.0576	18.1191	6.1
5500.9359	12.3703	6.6	5726.9011	15.6386	8.3	5824.0747	18.1234	6.3
5500.9433	12.3655	6.4	5726.9127	15.6419	6.3	5824.0921	18.1163	6.5
5500.9507	12.3605	6.3	5728.2610	15.6724	6.4	5824.1092	18.1119	6.5
5500.9582	12.3576	6.6	5728.2985	15.6763	6.2	5826.1543	18.1674	6.9
5500.9656	12.3587	6.3	5763.9874	16.5336	6.5	5839.9518	18.5417	9.8
5500.9730	12.3580	6.6	5764.0055	16.5320	6.7	5841.9589	18.6083	6.8
5500.9804	12.3687	6.3	5764.1552	16.5339	6.6	5841.9706	18.6037	7.0
5533.9725	12.4435	7.4	5764.1671	16.5431	6.5	5843.0622	18.6414	6.9
5533.9819	12.4466	7.2	5764.1783	16.5526	6.5	5843.0792	18.6386	6.9
5533.9914	12.4471	7.7	5764.9525	16.5662	6.2	5843.0961	18.6385	6.8
5534.9881	12.4694	7.2	5764.9621	16.5661	6.4	5843.1129	18.6428	6.7
5535.0059	12.4470	6.8	5765.8835	16.5870	7.2	5844.1228	18.6634	6.6
5553.0111	12.5491	7.7	5765.9011	16.5830	6.7	5844.1404	18.6686	6.7
5553.0261	12.5558	7.5	5767.0798	16.6200	6.7	5846.8452	18.7396	7.0
5553.0412	12.5531	7.4	5767.0915	16.6224	6.7	5846.8604	18.7356	7.3
5572.9430	12.7637	6.9	5767.1206	16.6314	6.7	5846.8777	18.7380	6.5
5572.9581	12.7557	7.5	5767.1322	16.6296	6.7	5846.8932	18.7392	7.4
5574.0422	12.7856	7.6	5784.7999	17.0869	6.8	5863.0145	19.1878	7.0
5574.0573	12.7764	7.2	5784.8183	17.0977	7.3	5863.8475	19.2062	7.0
5576.0025	12.8045	7.7	5817.0359	17.9290	7.1	5868.9442	19.3577	7.8
5601.9411	13.1190	7.6	5817.0559	17.9401	8.1	5868.9593	19.3596	7.6
5643.8667	13.8439	5.8	5817.9853	17.9546	7.3	5870.0943	19.3815	6.9
5643.8818	13.8395	5.8	5818.0047	17.9574	7.2	5870.1113	19.3755	6.8
5643.8969	13.8521	5.7	5820.0444	18.0154	6.5	5870.1284	19.3825	7.0
5669.8336	14.3697	6.2	5820.0526	18.0190	6.6	5870.1458	19.3807	6.9
5669.8487	14.3720	6.1	5820.0641	18.0067	7.4	5870.1628	19.3751	6.8
5669.8637	14.3550	6.0	5820.0723	18.0074	7.4	5871.1623	19.4045	6.7
5670.9317	14.3732	9.4	5820.0985	18.0157	6.8	5898.0254	20.1313	7.3
5670.9468	14.3748	8.6	5820.1066	18.0166	6.9	5898.0425	20.1501	7.3
5670.9618	14.3738	7.8	5820.1165	18.0197	7.2	5898.0612	20.1385	6.8
5675.7950	14.4807	6.8	5820.1247	18.0164	7.2	5898.0781	20.1310	7.6
5695.8075	14.9356	8.3	5820.0444	18.0154	6.5	5898.0962	20.1430	8.7
5695.8274	14.9179	7.7	5820.0526	18.0190	6.6	5900.1120	20.2013	6.9
5695.8495	14.9123	8.7	5820.0641	18.0067	7.4	5900.1291	20.2040	7.3

Julian Date 245...	RV (km/s)	Error (m/s)
5902.8949	20.2761	6.9
5931.9887	21.0868	6.2
5932.0061	21.0856	6.1
5933.9443	21.1278	8.4
5933.9652	21.1457	7.1
5934.9895	21.1641	6.2
5936.9591	21.2231	6.4
5936.9760	21.2260	6.3

References

Acuña, M.H., Connerney, J.E.P., & Ness, N.F., 1983, J. Geophys. Res. 88(A11): 8771.

Bahcall, J.N., Pinsonneault, M.H., & Wasserburg, G.J., 1995, Reviews of Modern Physics 67(4): 781.

Barbier-Brossat, M., & Figon, P., 2000, Astronomy and Astrophysics Supplement Series 142: 217.

Beaulieu, J.P., Bennett, D.P., Fouque, P., et al., 2006, Nature 439(7075): 437.

Bennett, D.P., Bond, I.A., Udalski, A., et al., 2008, The Astrophysical Journal 684: 663.

Bessel, M.S., 1990, Astronomy and Astrophysics Supplement Series 83: 357.

Bessell, M.S., & Wood, P.R., 1984, Publications of the Astronomical Society of the Pacific 96: 247.

Böhm-Vitense, E., 1992, Introduction to stellar astrophysics. Volume 3. Stellar structure and evolution. (E.. Cambridge University Press, Cambridge (UK)).

Borucki, W.J., Koch, D., Basri, G., et al., 2003, Kepler Mission: A mission to find Earth-size planets in the habitable zone. in Towards Other Earths: Darwin/Tpf and the Search for Extrasolar Terrestrial Planets, Proceedings, ed H. Lacoste (69).

Borucki, W.J., Koch, D.G., Batalha, N., et al., 2011, ArXiv e-prints 1112: 1640.

Boss, A., 2009, The Crowded Universe : The Search for Living Planets, (Basic Books).

Bulirsch, R., & Stoer, J., 1965, §2.2 in Introduction to Numerical Analysis. (Springer-Verlag, New York).

Busse, F.H., 1978, Annu. Rev. Fluid Mech. 10: 435.

Butler, R.P., Marcy, G.W., Williams, E., et al., 1996, Publications of the Astronomical Society of the Pacific 108: 500.

Campbell, B., Auman, J., Walker, G., & Yang, S., 1979, Precision Radial Velocities with the Hydrogen Fluoride Absorption Cell. in Bulletin of the American Astronomical Society.

Campbell, W.W., & Moore, J.H., 1928, Publications of Lick Observatory 16: 315.

Chambers, J.E., 1999, Monthly Notices of the Royal Astronomical Society 304(4): 793.

Christie, W.H., 1936, The Astrophysical Journal 83: 433.

Cohen, C.J., & Hubbard, E.C., 1965, The Astronomical Journal 70: 10.

Colacevich, A., 1935, Publications of the Astronomical Society of the Pacific 47: 87.

Connerney, J.E.P., Ness, N.F., & Acuna, M.H., 1982, Nature 298(5869): 44.

Cornwell, T.J., & Evans, K.F., 1985, Astronomy and Astrophysics 143: 77.

Cuntz, M., Eberle, J., & Musielak, Z.E., 2007, Astrophysical Journal 669(2): L105.

Cutri, R.M., Skrutskie, M.F., van Dyk, S., et al., 2003, VizieR Online Data Catalog 2246: 0.

David , J.S., 2003, Earth and Planetary Science Letters 208(1-2): 1.

Doppler, C., 1846, Annalen der Physik 144(5): 1.

Eberle, J., & Cuntz, M., 2010, The Astrophysical Journal 721: L168.

Eggen, O.J., 1993, The Astronomical Journal 106: 80.

Einstein, A., 1936, Science 84(2188): 506.

Endl, M., Kuerster, M., Barnes, S.I., et al., 2009, Searching for Planets in the Alpha Cen System: from Jupiters to Earth Analogs. in AAS/Division for Planetary Sciences Meeting Abstracts.

Endl, M., Kürster, M., & Els, S., 2000, Astronomy and Astrophysics 362: 585.

Fegley Jr, B., & Lodders, K., 1994, Icarus 110(1): 117.

Gerstenkorn, S., & Luc, P., 1978, Paris: Editions du Centre National de la Recherche Scientifique (CNRS), 1978.

Gray, D.F., 1983, Publications of the Astronomical Society of the Pacific 95: 252.

Griffin, R.F., & Griffin, R.L., 1973, Monthly Notices of the Royal Astronomical Society 162: 243.

Guillot, T., 1999, Science 286(5437): 72.

Guillot, T., & Gautier, D., 2009, ArXiv e-prints 0912: 2019.

Harrington, R.S., 1977, The Astronomical Journal 82: 753.

Hatzes, A.P., & Cochran, W.D., 1993, The Astrophysical Journal 413: 339.

Hatzes, A.P., Cochran, W.D., Endl, M., et al., 2006, Astronomy and astrophysics (Berlin) 457(1): 335.

Hatzes, A.P., Cochran, W.D., Endl, M., et al., 2003, The Astrophysical Journal 599: 1383.

Hatzes, A.P., Cochran, W.D., McArthur, B., et al., 2000, The Astrophysical Journal Letters 544: L145.

Hearnshaw, J.B., Barnes, S.I., Kershaw, G.M., et al., 2002, Experimental Astronomy 13(2): 59.

Hilditch, R.W., 2001, An introduction to close binary stars. (Cambridge University Press, Cambridge ; New York).

Holman, M.J., & Wiegert, P.A., 1999, The Astronomical Journal 117(1): 621.

Houk, N., 1978, Ann Arbor : Dept. of Astronomy, University of Michigan : distributed by University Microfilms International, 1978-.

Hubbard, W.B., 1968, The Astrophysical Journal 152: 745.

Huensch, M., Schmitt, J.H.M.M., Schroeder, K.P., & Reimers, D., 1996, Astronomy and Astrophysics 310: 801.

Ingersoll, A.P., Barnet, C.D., Beebe, R.F., et al., 1995, Dynamic meteorology of Neptune. in Neptune and Triton.

Israelian, G., Santos, N.C., Mayor, M., & Rebolo, R., 2001, Nature 411(6834): 163.

Jacob, W.S., 1855, Monthly Notices of the Royal Astronomical Society 15: 228.

Jefferys, W.H., 1974, The Astronomical Journal 79: 710.

Jones, H.S., 1928, Ann. Cape Obs. 10(8): 237.

Kepler, J., 1609, (Pragae) 1609 32.

Kepler, J., Ptolemaeus, C., & Fludd, R., 1619, Lincii Austriae, sumptibus G. Tampachii, excudebat I. Plancvs, 1619. 38.

Konacki, M., & Wolszczan, A., 2003, The Astrophysical Journal Letters 591: L147.

Lejeune, T., & Schaerer, D., 2001, VizieR Online Data Catalog 6102: 0.

Lindal, G.F., Wood, G.E., Levy, G.S., et al., 1981, J. Geophys. Res. 86(A10): 8721.

Lyapunov, M.A., 1907, Ann. Fac. Sci., University of Toulouse, 9, 203

Malhotra, R., Vieira Martins, R., Ferraz-Mello, S., & Fernandez, J., 1998, Orbital Resonances and Chaos in the Solar System. in Solar System Formation and Evolution.

Marcy, G.W., & Butler, R.P., 1992, Publications of the Astronomical Society of the Pacific 104(674): 270.

Marcy, G.W., Butler, R.P., Fischer, D., et al., 2001, The Astrophysical Journal 556: 296.

Mayor, M., & Queloz, D., 1995, Nature 378(6555): 355.

Mermilliod, J.C., 2006, VizieR Online Data Catalog 2168: 0.

Morais, M.H.M., & Correia, A.C.M., 2008, Astronomy and Astrophysics 491: 899.

Morais, M.H.M., & Correia, A.C.M., 2012, Monthly Notices of the Royal Astronomical Society 419(4): 3447.

Murdoch, K.A., Hearnshaw, J.B., & Clark, M., 1993, The Astrophysical Journal 413: 349.

Ness, N.F., Acuna, M.H., Behannon, K.W., et al., 1986, Science 233(4759): 85.

Ness, N.F., Acuna, M.H., Burlaga, L.F., Connerney, J.E.P., & Lepping, R.P., 1989, Science 246(4936): 1473.

Neuhäuser, R., Mugrauer, M., Fukagawa, M., Torres, G., & Schmidt, T., 2007, A&A 462(2): 777.

Newton, I., 1760, Colonia : A. Philibert; 548 p. ; in 8.; DCC.4.221 I through IV.

Ollivier, M., Encrenaz, T., Roques, F., Selsis, F., & Casoli, F., 2008, Planetary Systems, (Springer-Verlag Berlin and Heidelberg GmbH & Co. KG).

Povich, M.S., Giampapa, M.S., Valenti, J.A., et al., 2001, The Astronomical Journal 121: 1136.

Press, W.H., Teukolsky, S.A., Vetterling, W.T., & Flannery, B.P., 2007, Numerical Recipes: The Art of Scientific Computing. (Cambridge University Press, New York).

Proudman, J., 1916, Proceedings of the Royal Society of London. Series A 92(642): 408.

Quarles, B., Cuntz, M., & Musielak, Z.E., 2012, ArXiv e-prints 1201: 2313.

Quarles, B., Eberle, J., Musielak, Z.E., & Cuntz, M., 2011, Astronomy and astrophysics (Berlin) 533: A2.

Queloz, D., Henry, G.W., Sivan, J.P., et al., 2001, Astronomy and Astrophysics 379: 279.

Rabin, S., 2010, Nicolaus Copernicus. in Stanford Encyclopedia of Philosophy, (Stanford University).

Ramírez, I., & Meléndez, J., 2005, The Astrophysical Journal 626: 465.

Ramm, D.J., 2004, A spectroscopic study of detached binary systems using precise radial velocities : a thesis submitted in partial fulfilment of the requirements for the degree of Doctor of Philosophy in Astronomy in the University of Canterbury. (University of Canterbury).

Ramm, D.J., Pourbaix, D., Hearnshaw, J.B., & Komonjinda, S., 2009, Monthly Notices of the Royal Astronomical Society 394: 1695.

Rauch, K.P., & Hamilton, D.P., 2002, The HNBody Package for Symplectic Integration of Nearly-Keplerian Systems. in Bulletin of the American Astronomical Society.

Richardson, L.F., 1911, Philosophical Transactions of the Royal Society of London. Series A, Containing Papers of a Mathematical or Physical Character 210(459-470): 307.

Rivera, E.J., & Lissauer, J.J., 2001, The Astrophysical Journal 558: 392.

Runge, C., 1895, Mathematische Annalen 46(2): 167.

Sanchez-Lavega, A., Lecacheux, J., Gomez, J.M., et al., 1996, Science 271(5249): 631.

Santos, N.C., Mayor, M., Naef, D., Queloz, D., & Udry, S., 2001, ArXiv Astrophysics e-prints: 1377.

Schneider, J., 2012, The Extrasolar Planets Encyclopaedia, (Paris Observatory).

See, T.J.J., 1896, The Astronomical Journal 16: 17.

Seidelmann, P.K., Archinal, B.A., A'Hearn, M.F., et al., 2007, Celestial Mechanics and Dynamical Astronomy 98(3): 155.

Sheppard, S.S., 2012, The Giant Planet Satellite and Moon Page, (Carnegie Institution of Science, Department of Terrestrial Magnetism).

Simon-Miller, A.A., Gierasch, P.J., Beebe, R.F., et al., 2002, Icarus 158(1): 249.

Skuljan, J., 2007, HRSP Manual Version 3.0. (University of Canterbury).

Sterne, T.E., 1941, Proceedings of the National Academy of Science 27: 175.

Taylor, G.I., 1917, Proceedings of the Royal Society of London. Series A 93(648): 99.

Toner, C.G., & Gray, D.F., 1988, The Astrophysical Journal 334: 1008.

Udalski, A., Jaroszy'ski, M., Paczy'ski, B., et al., 2005, The Astrophysical Journal Letters 628: L109.

Valenti, J.A., Butler, R.P., & Marcy, G.W., 1995, Publications of the Astronomical Society of the Pacific 107: 966.

van Helshoecht, V., & Groenewegen, M.A.T., 2007, Astronomy and Astrophysics 463: 559.

van Leeuwen, F., 2007, Hipparcos, the New Reduction of the Raw Data. in Astrophysics and Space Science Library, ed F. van Leeuwen.

von Zahn, U., Hunten, D.M., & Lehmacher, G., 1998, J. Geophys. Res. 103(E10): 22815.

Walker, G.A.H., Walker, A.R., Irwin, A.W., et al., 1995, Icarus 116: 359.

Wisdom, J., & Holman, M., 1991, The Astronomical Journal 102: 1528.

Wisdom, J., Holman, M., & Touma, J., 1996, Fields Institute Communications, Vol. 10, p. 217 10: 217.

Wolszczan, A., & Frail, D.A., 1992, Nature 355(6356): 145.

Yoshida, H., 1990, Physics Letters A 150(5–7): 262.